

Coulomb balls -
Structure and confinement of spherical dust
crystals in a plasma

Dissertation
zur Erlangung des Doktorgrades
der Mathematisch-Naturwissenschaftlichen Fakultät
der Christian-Albrechts-Universität zu Kiel

vorgelegt von
Oliver Arp

Kiel
April 2006

Referent: Prof. Dr. A. Piel

Koreferent:

Tag der mündlichen Prüfung: 07. Juni 2006

Zum Druck genehmigt: Kiel, den

Der Dekan

Abstract

In this thesis the fundamental properties of "Coulomb balls" are explored, a newly discovered form of spherical crystalline complex plasmas. Coulomb balls show an unusual type of structural order in complex plasmas, which is similar to laser-cooled ion clusters in Paul and Penning traps.

Inside a Coulomb ball the dust particles are arranged in nested shells. Within each shell the particles form a hexagonal lattice, which is affected by defects as a consequence of the curvature of the shell surface. This kind of structure is consistent with theoretical calculations and simulations of finite Coulomb systems. The ambient plasma modifies the interaction law between the particles to a shielded Coulomb force, also called Yukawa interaction. A comparison of numerous experimentally observed Coulomb balls with molecular dynamics simulations of Coulomb and Yukawa clusters detected systematic differences in the shell radii and occupation numbers, which are attributed to the shielding of the plasma.

The confinement of Coulomb balls is based on the combination of two principles that have been separately used before in the context of complex plasmas. Dielectric walls, in the form of a small cubical glass box, were used to shape the plasma profile and to generate a lateral confinement of the enclosed dust cloud. Further, a thermophoretic force is applied to compensate for gravity, which in combination with the plasma induced electric field force establishes a vertical confinement. The proposed functional principle of the trap used for confining Coulomb balls was quantitatively verified. For this purpose the thermophoretic force field inside the trap was measured. The plasma conditions inside the trap were obtained from plasma simulations. The results were used for deriving the plasma-induced forces. Superimposing the force fields of the measured thermophoretic force and of the plasma-induced forces yields the total potential well of the trap. The size as well as the location of the observed Coulomb ball is in excellent agreement with the derived trap potential.

Future investigation of Coulomb balls with time resolved measurements of all particle trajectories promise a deep insight into the thermodynamics of finite systems with shielded Coulomb interaction.

Kurzfassung

In dieser Arbeit werden die fundamentalen Eigenschaften von "Coulomb-Balls" untersucht, einer neu entdeckten Art von sphärischen kristallinen komplexen Plasmen. Coulomb-Balls zeigen eine für komplexe Plasmen ungewöhnliche Art von struktureller Ordnung, die große Ähnlichkeiten mit lasergekühlten Ionenclustern in Paul- und Penning-Fallen hat.

In einem Coulomb-Ball sind die Staubpartikel auf ineinander geschichteten Schalen angeordnet. Innerhalb jeder Schale bilden die Partikel ein hexagonales Gitter, welches aufgrund der Krümmung der Schalenoberfläche von Defekten durchsetzt ist. Diese Art der strukturellen Ordnung stimmt mit theoretischen Berechnungen und Simulationen finiter Coulomb-Systeme überein. Das umgebende Plasma schirmt die Coulomb-Wechselwirkung zwischen den Staubpartikeln eines Coulomb-Balls ab, und führt zu einer so genannten Yukawa-Wechselwirkung. Ein Vergleich zahlreicher experimentell beobachteter Coulomb-Balls mit molekulardynamischen Simulationen von Coulomb- und Yukawa-Clustern deckte systematische Unterschiede in den Schalenradien und Besetzungszahlen auf, welche auf die unterschiedliche Wechselwirkung zurückgeführt wurden.

Die zur Erzeugung von Coulomb-Balls benutzte Falle basiert auf der Kombination von zwei Prinzipien, welche einzeln bereits vorher im Bereich komplexer Plasmen eingesetzt wurden. Dielektrische Wände in Form einer kleinen kubischen Glasküvette werden zur Formung des Plasmaprofiles und zur Erzeugung des seitlichen Einschlusses der Staubwolke benutzt. Zusätzlich wird eine thermophoretische Kraft eingesetzt, um die Wirkung der Gravitation zu kompensieren. Dies ermöglicht in Verbindung mit der plasmainduzierten elektrischen Feldkraft den vertikalen Einschluss. Zur quantitativen Verifikation des Funktionsprinzips der Falle wurde das thermophoretische Kraftfeld in ihrem Inneren vermessen und die plasmainduzierten Kräfte bestimmt. Da die Plasmaparameter in der Falle nicht experimentell gemessen werden können, wurden diese aus Plasmasimulationen gewonnen und zur Bestimmung der plasmainduzierten Kräfte verwendet.

Die Überlagerung der Kraftfelder der gemessenen thermophoretischen Kraft und der plasmainduzierten Kräfte liefert den Potentialverlauf in der Falle. Sowohl die Größe als auch die Position des beobachteten Coulomb-Balls stimmen hervorragend mit dem bestimmten Fallenpotential überein.

Zukünftige Untersuchungen von Coulomb-Balls mit zeitaufgelösten Messungen aller Partikeltrajektorien versprechen einen tiefen Einblick in die Thermodynamik von finiten Systemen mit abgeschirmter Coulomb-Wechselwirkung.

Contents

1	Introduction	1
2	Confinement of finite strongly-coupled Coulomb systems	4
2.1	Ion clusters in Paul- and Penning traps	5
2.2	Confinement of complex plasmas	7
2.2.1	Complex plasmas in the sheath of an rf discharge	8
2.2.2	Three dimensional complex plasmas	12
2.2.3	Other discharge geometries	13
3	The discovery of Coulomb balls	15
3.1	Experimental setup	15
3.1.1	Properties and handling of dust particles	17
3.2	First experiments and observations	19
3.2.1	Dust inside the glass box	20
3.2.2	Heating of the electrode	22
3.3	Spherical dust clouds	25
4	Structure of Coulomb balls	27
4.1	Scanning video microscopy (SVM)	27
4.1.1	Data analysis	30
4.2	Global properties	31
4.3	Shell structure	34
4.4	Intrashell structure	37
4.5	Simulation of Coulomb balls	38
4.6	Large Coulomb balls	42
5	Confinement of Coulomb balls	46
5.1	Basic principle of the trap	46
5.2	The thermophoretic force	49
5.2.1	Particle image velocimetry (PIV)	52
5.2.2	Setup	54
5.2.3	Analysis of PIV data	56
5.2.4	Neutral friction	57
5.2.5	Balance of forces	59
5.2.6	The thermophoretic force field	61

5.2.7	Accuracy of the measurement	66
5.3	Plasma-induced forces	67
5.3.1	Simulation of the discharge	67
5.3.2	Electric field force	72
5.3.3	Ion-drag force	73
5.4	Properties of the trap	76
5.5	Higher-order effects	78
6	Summary and outlook	81

1 Introduction

Many-body systems consisting of identical charged particles interacting by electrostatic forces, so-called *Coulomb systems*, show a variety of interesting structural and dynamical phenomena. Such a system is called *strongly coupled*, when the potential energy of the particles due to their electrostatic interaction overcomes the average kinetic energy of their thermal random motion. In this case the particles are spatially strongly correlated, which allows these systems to show liquid and crystalline behavior. This work focuses on finite strongly-coupled systems. Due to their limited number of particles, these systems are on the one hand interesting for various theoretical investigations. On the other hand their structural properties are significantly different from the bulk order of extended systems, which is a consequence of the competition between the repulsive Coulomb interaction and the required confining forces. Some typical examples of finite strongly-coupled Coulomb systems are electrons on the surface of liquid helium [1], quantum dots [2], and laser-cooled ions in Paul and Penning traps [3–5].

In the context of this work, the most important realization of a strongly-coupled Coulomb system is a *complex* or *dusty plasma*, which is a gas plasma containing besides electrons and ions an additional component, namely highly charged macroscopic dust particles. In contrast to typical Coulomb systems, the dust particles are interacting by shielded Coulomb forces, a so-called Yukawa interaction, which is a consequence of the shielding property of the surrounding plasma. Originally, complex plasmas were known from astrophysics where they are found e.g. in interstellar dust clouds, in the tails of comets and in the ring systems of giant gas planets [6]. Besides these remote systems, complex plasmas are present in many industrial processes. Some examples are thin film deposition of silicon, which plays a role e.g. in the production of high efficiency solar cells or flat panel displays, and powder treatment (e.g. Ref. [7,8]). In addition, dust particles occur inside plasma etching reactors of the semiconductor industry, where these particles negatively affect the yield of the chip production and have to be removed efficiently [9].

With the discovery of the plasma crystal in 1994, the interest in complex plasmas rose abruptly. [10–12]. Complex plasmas turned out to be ideally suited for studying phenomena of strong coupling. The macroscopic size and the large mass of the dust particles slows down their motion and, in contrast to most other strongly coupled systems, allows to observe the individual particles by very simple means, even with the naked eye. In addition, the large charges of the typically

micrometer-sized dust particles results in comparatively large inter-particle distances of a few hundred micrometers. This results in a very high transparency of a complex plasma which gives access to each single particle even in the center of a large dust cloud.

In the laboratory, complex plasmas are typically generated in parallel plate rf discharges. As a consequence of gravity, particles injected into the plasma sediment to its lower boundary, where they are levitated by strong electric fields. Here, assuming identical particle sizes and suitable plasma conditions, flat dust clouds with a limited vertical extension are found, where the particles are arranged in regular crystalline lattices. These nearly two-dimensional systems, which have similarities to colloidal suspensions [13, 14], show a rich set of interesting phenomena, like phase transitions [15, 16], fluid motion [17], and a variety of wave phenomena (e.g. Ref. [18]) on quasi-atomic scale. By means of suitable horizontal barriers the generation of two-dimensional finite dust clusters is possible [19, 20].

The large mass of the particles complicates the generation of three-dimensional complex plasmas, since gravity forces the dust to arrange in flat clouds with a small vertical extension. To eliminate the effect of gravity, experiments were performed under microgravity conditions in space [21–24] or on parabolic flights (e.g. Ref. [25, 26]). In these experiments extended three-dimensional complex plasmas could be generated. However, the dust is not evenly distributed in the complete volume, but is disturbed by a dust-free region in the center of the discharge, the so-called *void phenomenon* (e.g. Ref. [22, 25]). Similar results are found in laboratory experiments, when gravity is compensated by thermophoretic forces [27]. With respect to studying finite systems, the resulting hollow dust cloud is actually the opposite of the desired situation.

Confinement by electric fields that are strong enough to levitate micrometer-sized particles is always accompanied by superthermal ion flows. This ion flow is responsible for the generation of attractive forces by means of charge accumulated in the wake behind a particle [28]. The attractive forces are responsible for particle chain formation as observed in dust clouds in the rf sheath [15, 29, 30] or in striations of a dc discharge [31].

In this work spherical dust crystals were successfully generated, which we named "Coulomb balls". This system is the subject of studies in the present thesis. The first major goal of investigations is a careful analysis of the structural properties of Coulomb balls. In a further step the interest is focused on similarities with and differences from trapped ion crystals. Deviations are expected from the different interaction law, namely shielded Yukawa interaction in Coulomb balls and pure Coulomb interaction in ion crystals.

For the structural investigations suitable methods have to be implemented. Two-dimensional systems could be studied with conventional video microscopy (e.g. Ref. [15]), which permits tracing of individual particle trajectories with high spatial and temporal resolution. A three-dimensional object like the Coulomb ball requires a different approach. When the system is in a solid phase, scanning video microscopy can be used to recover the three-dimensional structure. In this technique a laser sheet illuminates a thin slice of the system. The sheet and the camera are moving together in order to record a sequence of slices, from which the particle coordinates are recovered in three dimensions. Such techniques were used earlier in the analysis of three-dimensional particle arrangements in dusty plasmas (e.g. Ref. [26,32]). This method will be used for the structural analysis of the solid phase of the Coulomb ball. The method fails, however, in liquid states because of the particle motion.

The second major goal of the present thesis is a quantitative analysis of the forces that lead to the confinement of the Coulomb balls. Since the generation of Coulomb balls involves thermophoretic levitation and lateral confinement by glass walls, the different acting forces are analyzed separately. An absolute measurement of the thermophoretic force field is attempted by analysing the trajectories of tracer particles. Other electric forces, which result from surface charges on the glass walls and from the space charge of the plasma particles are not accessible by direct experimental technique. For this reason, the electric forces are studied by means of computer simulations with a proven simulation code for high-frequency discharges.

This survey of Coulomb balls is structured as follows: In Chapt. 2 a short introduction into the basic properties and the confinement of strongly coupled systems is given. Especially ion clusters in Paul and Penning trap and complex plasmas are treated. This knowledge is important for understanding the basic principle of the constructed trap. A first series of experiments is presented in Chapt. 3, which illustrates the behavior of dust inside the trap and ends with the generation of Coulomb balls. These experiments are followed by a detailed structural analysis of Coulomb balls in Chapt. 4 including comparisons with simulations and other strongly coupled systems. In Chapt. 5 further experiments are presented, which allow for identifying the dominant forces that contribute to the confinement. In a hierarchical approach, beginning with the strongest, these forces are quantitatively determined and analyzed with respect to their contribution to the confinement. At the end, all forces are combined to derive the total topology of the trap, which is used to evaluate the integrity of the proposed model of the trap.

2 Confinement of finite strongly-coupled Coulomb systems

Systems containing multiple charged particles interacting by electromagnetic forces are present in many fields of physics. A simplified model of these systems considers point-like charges interacting by Coulomb forces embedded in a homogenous neutralizing background. The physics of this so-called *one component plasma* (OCP) is closely related to the classical atom model of Thomson [33]. Assuming identical charges q , the correlation between the individual particles of an OCP is described by the *coupling parameter*

$$\Gamma = \frac{q^2}{4\pi\epsilon_0 a_{ws}} \frac{1}{k_B T} . \quad (2.1)$$

Here is T the kinetic temperature of the particles, ϵ_0 the electric permittivity of free space and k_B Boltzmann's constant. Thus, Γ is the ratio of the average Coulomb interaction energy and the average thermal kinetic energy at the *Wigner-Seitz radius* a_{ws} , which is defined by the equation

$$\frac{4}{3}\pi a_{ws}^3 = \frac{1}{n} , \quad (2.2)$$

with the number density n of the particles. Hence, Eq. (2.2) assigns to each particle a volume fraction of the complete system, which equals a sphere of radius a_{ws} . The Wigner-Seitz radius a_{ws} is a measure of the average distance between individual particles, although it is not identical with the average inter-particle distance (see Sec. 4.2). An OCP in which the Coulomb interaction energy between the charges overcomes the thermal kinetic energy, i.e. $\Gamma > 1$, is called *strongly coupled*. Up to a value $\Gamma \approx 174$ the system is a liquid [34], whereas larger values of Γ yield a crystalline state where the particles are arranged in a regular lattice.

Already in 1934, Wigner used this model to predict a solid phase of strongly coupled electrons inside a metal [35]. According to Eq. (2.1) a strongly coupled system requires either large values of the charge q , densely packed particles, i.e. low values of a_{ws} , or low temperatures T . In the laboratory, typical examples of strongly-coupled systems are electrons on the surface of liquid helium [1], quantum dots [2], and laser-cooled ions in Paul [3, 4] and Penning traps [5]. The

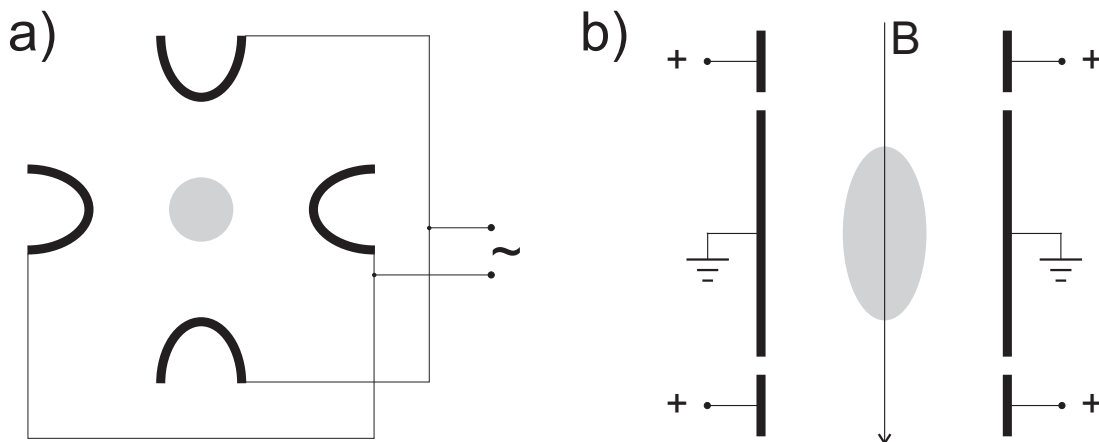


Figure 2.1: Schematic section of (a) a Paul and (b) a Penning trap.

missing neutralizing background of these non-neutral systems requires the presence of an external confinement to prevent an electrostatic explosion. A very low temperature of typically a few milli-Kelvin characterizes these systems, which allows the particles to condense into a crystalline state. Usually not accessible for laboratory experiments are systems, in which the strong coupling is attributed to dense packing of the charged particles. It is believed that the compressed interior of brown dwarf stars and giant gas planets consists of strongly-coupled ions that are embedded in a weakly coupled (degenerate) gas of electrons [36]. Complementary to the mentioned systems are colloidal suspensions of macroscopic particles [13, 14], and complex plasmas [10–12]. Here, typically micrometer-sized particles carry large charges, which results in strong interaction of the particles at comparatively long distances. The macroscopic size and the large mass of the particles slows down their motion and makes these systems very interesting for studying phenomena of strong coupling.

Since the interaction between the individual charges is repulsive, these systems require some kind of confinement to prevent an electrostatic explosion. Due to the special relevance within the context of this work the confinement of ion clusters and finite complex plasmas is described in the following.

2.1 Ion clusters in Paul- and Penning traps

Strongly coupled clusters of laser-cooled ions were first experimentally observed in Paul traps [3, 4]. These traps use an oscillating electric field to confine charged particles. A schematic section illustrating the basic geometry is shown in Fig. 2.1 (a). An rf electric quadrupole field is generated by four electrodes that are pairwise connected. The frequency of the electric field depends on the mass of the individual trapped particles and for ions is in the MHz range. This mass sensitivity of the trap is widely utilized in quadrupole mass spectrometers, which use a linear Paul trap as mass filter. To confine small clusters of ions in all three dimensions, a typical trap geometry is obtained by rotating the electrode geometry

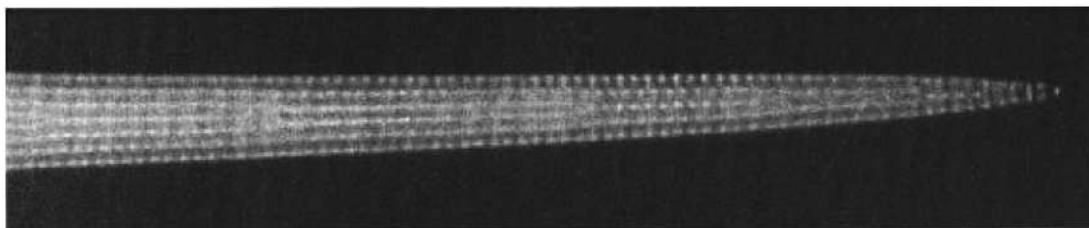


Figure 2.2: Partial view of an elongated ion cluster confined in a linear Paul trap. From Ref. [38].

in Fig. 2.1 (a) about the vertical axis. This yields a trap with a horizontal ring electrode and two endcaps.

The motion of a confined particle inside a Paul trap is described by the Mathieu equation [37]. The oscillating electric field induces a micromotion of the particles about the average position of each individual particle. The amplitude of oscillation increases with the distance from the center of the trap. Due to the strong coupling of the particles by Coulomb interaction, the larger amplitude of outer particles induces a heating of the inner particles. Consequently this so-called rf heating limits the size of a confinable strongly coupled system. Hence, the first experiments that observed crystalline order [3] and phase transitions [4] were limited to small clusters containing typically less than 10 particles. Within the context of these experiments, Diedrich *et al.* [3] observed a crystalline planar cluster consisting of a central particle surrounded by a hexagonal structure of 6 other particles. To confine larger systems, Drewsen *et al.* [38] used a linear Paul trap. The authors confined elongated ion systems with a large aspect ratio (see Fig. 2.2). Here, the influence of rf heating is reduced due to the limited radial extension of the ion cloud, which allows for observing $> 10^5$ ions in a crystalline state.

Another method of confining ion clusters is the use of a Penning trap. Here, the ions are confined by a combination of a static electric and magnetic field [34]. In contrast to a Paul trap, the confined clusters are not subject to heating as a consequence of oscillating fields. This, on the one hand, allows for laser-cooling the ions down to temperatures of a few mK and, on the other hand, for the observation of extended spherical clusters. A schematic section of a Penning trap is shown in Fig. 2.1 (b). The cylindrical trap has three segments. The central part is electrically grounded whereas both outer segments are held at a positive potential for confining positive ions. This generates an axial electric field between the outer and the inner segments, which causes an electric force that confines a positive ion in a harmonic potential well along the axis of the trap. The radial confinement of the trap is realized by a uniform axial magnetic field, which provides a radially inwards directed Lorentz force to compensate for centrifugal and electrostatic force and induces a cyclotron motion of the ions. Thus, the size of the confined dust cloud is limited by the magnetic field strength. In addition, the cyclotron motion is superimposed by an $\vec{E} \times \vec{B}$ motion, which causes

2.2. CONFINEMENT OF COMPLEX PLASMAS

complex trajectories of the individual ions including a rotation of the complete ion cloud about the axis of the trap. This rotation complicates the observation of the trapped ion cloud and made the use of imaging techniques in the first experiments impossible. However, by means of sophisticated synchronization techniques [39, 40] it became later possible to image laser induced fluorescence of single ions in a Paul trap [41].

The structural observations made in both described traps are qualitatively the same. In small clusters, the ions are arranged in concentric nested shells that match the shape of the trap [5, 38]. This finding is consistent with theoretical models and simulations (e.g. Ref. [42–45]) of finite Coulomb systems. Itano *et al.* [46] confined large spherical ion clusters containing more than 10^5 particles in a Penning trap. The authors found that in such large systems the shell structure is only found in the outer region of the cluster. In the center, a crystalline body centered cubic (bcc) [47] structure was found, which is theoretically expected for an infinite OCP [34], but was also recently reported from simulations of large spherical clusters [48].

2.2 Confinement of complex plasmas

A complex or dusty plasma is a plasma which, besides free electrons and ions, contains a third component of macroscopic dust particles. In the usual case of an electronegative plasma the dust particles attain a negative charge q_d as a consequence of the higher electron mobility compared to the ions. Due to the shielding property of the surrounding plasma, the interaction between the dust particles in a complex plasma is not of pure Coulomb type, but is reduced by shielding. Consequently, in comparison to an ideal OCP with Coulomb interaction, the resulting Yukawa interaction between the particles requires larger values of Γ for establishing a crystalline system.

The shielding of the plasma is described by the *linearized Debye length*

$$\lambda_D = \left(\frac{1}{\lambda_{De}^2} + \frac{1}{\lambda_{Di}^2} \right)^{-1/2}, \quad (2.3)$$

with

$$\lambda_{De,i} = \sqrt{\frac{\epsilon_0 k_B T_{e,i}}{n_{e,i} e^2}}. \quad (2.4)$$

Here $T_{e,i}$ is the temperature, $n_{e,i}$ the number density of the electrons and the ions, respectively. Assuming identical charges q_d of the dust particles the resulting Yukawa interaction force between two particles at distance b is given by

$$\vec{F}_{yuk} = -\frac{q_d^2}{4\pi\epsilon_0 b} \left(\frac{1}{b} + \frac{1}{\lambda_D} \right) \exp\left(-\frac{b}{\lambda_D}\right) \vec{e}_b. \quad (2.5)$$

In the case $\lambda_D \rightarrow \infty$ Eq. (2.5) reduces to pure Coulomb interaction.

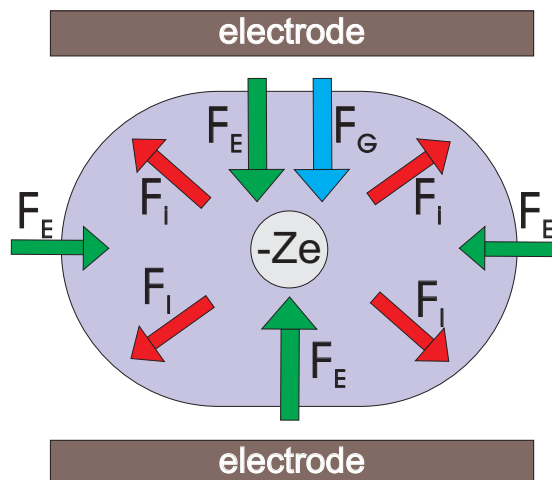


Figure 2.3: Forces acting on a charged dust particle inside a parallel-plate rf discharge.

The general possibility of Wigner crystallization in a complex plasma with Yukawa interaction was predicted in Ref. [49] several years before the discovery of the plasma crystal [10–12]. According to the phase diagram of Yukawa systems [50,51], the phase of a complex plasma depends strongly on the *screening strength*

$$\kappa = a_{ws}/\lambda_D , \quad (2.6)$$

and the melting line of a Yukawa system is approximated by the relation

$$\Gamma \exp(-\kappa) = 174 . \quad (2.7)$$

Consequently, assuming e.g. $\kappa = 0.5$ a Yukawa system can be considered crystalline when $\Gamma > 287$.

2.2.1 Complex plasmas in the sheath of an rf discharge

For studying complex plasmas in the laboratory, usually spherical micrometer sized dust particles are injected into a rf discharge. A schematic vertical section through a parallel plate rf discharge is shown in Fig. 2.3. The discharge is maintained by an oscillating voltage of typical 13.56 MHz, which is applied to the electrodes. A dust particle inside the discharge is naturally subject to gravity \vec{F}_g , which leads the particle to fall towards the lower electrode. Due to the charge of the particle, it is affected by electrical fields that are present in the plasma. However, its comparatively large inertia prevents the particle from following the oscillating rf field, i.e. the dust particles are only affected by time-averaged electrical fields. Since the (time-averaged) plasma potential has a positive maximum value in the center of the discharge [52], an electric force \vec{F}_E acts on the particle, which is directed towards the center of the discharge. In addition, a radially outward-directed ion-drag force \vec{F}_i is caused by streaming ions from the central

2.2. CONFINEMENT OF COMPLEX PLASMAS

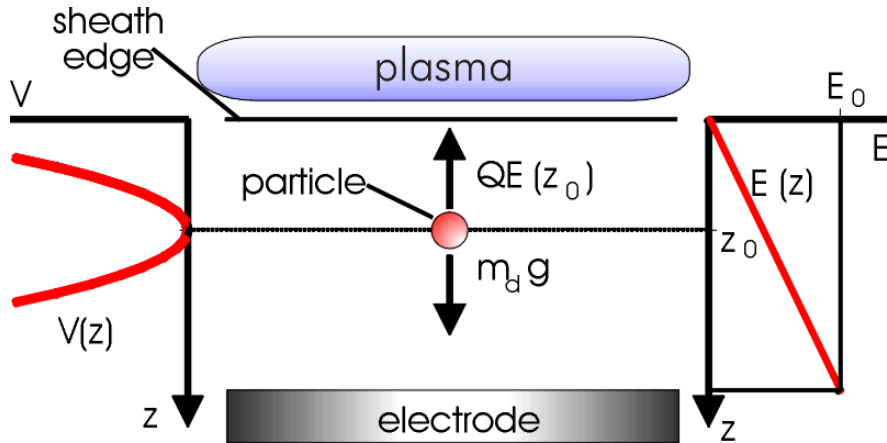


Figure 2.4: Confinement of flat complex plasmas in the lower sheath of a rf discharge. From Ref. [53].

region, where the primary plasma production takes place. This force displaces the particle from the center of the discharge but is typically negligible in the outer regions of the plasma (see Sec. 5.3). When using micrometer sized particles the gravitational force overcomes all other forces in most parts of the discharge except for the sheath region above the lower electrode. Here, a strong electric field causes an upwards directed force on the charged particles that is sufficiently strong to compensate for gravity.

A schematic detailed view of the lower sheath region is shown in Fig. 2.4. In good approximation the electric field E increases linearly from the plasma edge towards the electrode. This causes an upward-directed increasing electric force \vec{F}_E on a negatively charged particle. In combination with the gravitational force \vec{F}_g , a parabolic potential well is established, which confines the dust particle vertically. Depending on the mass of the particle it is levitated a few millimeters above the lower electrode. A horizontal confinement of the particle is achieved either by the positive plasma potential, which keeps the particles inside the plasmas, or by placing flat (typ. 1 – 2 mm) metallic barriers on top of the lower electrode, which deform the electric potential in the sheath in a suitable manner. By this means the horizontal extension of a complex plasmas in the sheath region containing multiple identical particles is adjustable from one-dimensional particle chains to extended two-dimensional systems. Depending on the plasma conditions these systems can reach liquid and crystalline states where the particles are arranged in a very regular pattern, the so-called *plasma crystal* [10–12].

A top view of an extended plasma crystal is shown in the upper part of Fig. 2.5. Each white dot corresponds to a single dust particle. The particles arrange themselves in a very regular pattern with mainly six neighbors, i.e. in an hexagonal lattice. This structure was also found in flat ion clusters in a Paul trap [3] and is the natural structure of two-dimensional OCPs. These flat complex plasmas have been explored for many years and offer a plenty of interesting phenomena.

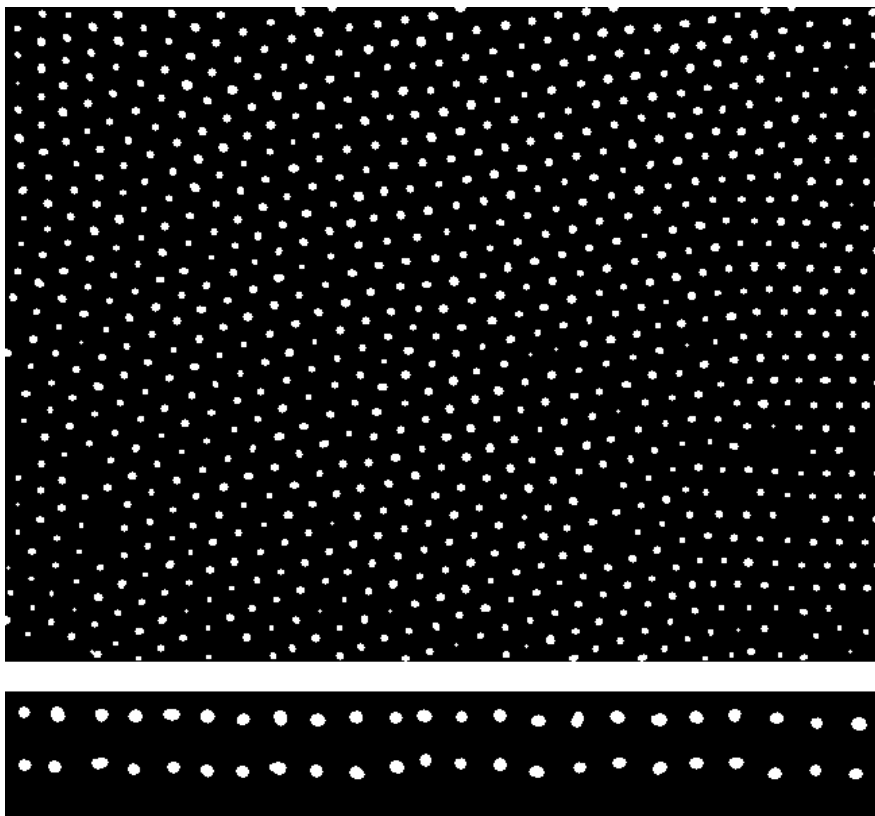


Figure 2.5: Topview of extended plasma crystal confined in the sheath of an rf discharge. below: side view of the same crystal. The particles are aligned in vertical chains. From Ref. [53].

Some examples are the observation of phase transitions [15,16], fluid motion [17], and a variety of wave phenomena (e.g. Ref. [18]).

By placing a flat metallic ring on top of the electrode, finite two-dimensional Coulomb clusters containing from a single to several hundred particles can be generated [19,20]. In contrast to extended two-dimensional plasma crystals, the structure of this finite clusters is strongly affected by the boundary conditions given by their lateral confinement. The competition of the repulsive interaction between the particles and the radial confinement forces the particles in the vicinity of the boundary to arrange in concentric rings. In Fig. 2.6 six two-dimensional clusters containing between three and 791 particles are shown. Small systems with less than ~ 30 particles are dominated by the influence of the confinement, which forces the particles to arrange in nested rings. By increasing the particle number the influence of the confinement vanishes in the central region, which leads the particles to arrange in a hexagonal lattice as it is found in extended plasma crystals (see Fig. 2.5). Due to the limited number of particles these systems are ideally suited for various theoretical and experimental studies of their structural [20, 54, 55] and thermodynamical properties [54–60].

In comparison to the observed structural properties of two and three-

2.2. CONFINEMENT OF COMPLEX PLASMAS

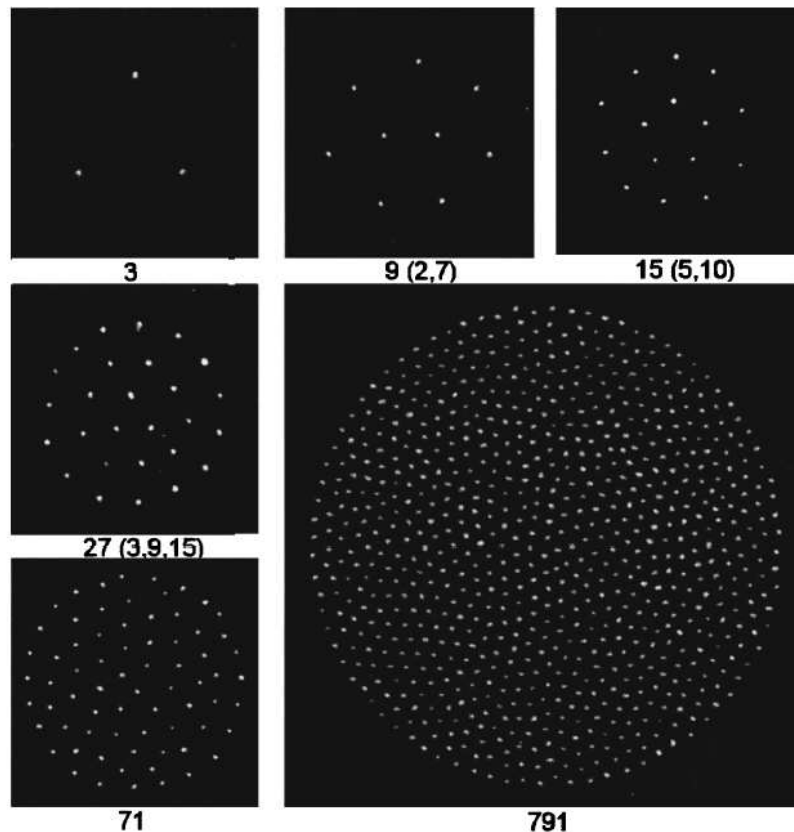


Figure 2.6: Finite clusters of consisting of different numbers of dust particles confined in the sheath of a rf discharge. From Ref. [19].

dimensional ion clusters the two-dimensional dust clusters show many similarities, which suggests the observation of finite three-dimensional dust clusters in complex plasmas. Unfortunately, the generation of a three-dimensional complex plasma is hampered by the influence of gravity and the non-equilibrium plasma conditions in the sheath region. Just injecting more particles yields multi-layered, so-called 2.5 dimensional systems. In Fig. 2.5 (b) a side view of the above plasma crystal is shown, which is actually a multi-layered system. One observes that in contrast to an isotropic three-dimensional crystal lattice the particles are arranged in vertical chains [15,29,30], which is caused by a directed ion flow in the sheath [28]. However, some experiments [61,62] showed that under certain conditions it is possible to generate extended multi-layer systems that show coexisting regions with fcc, bcc, and hcp lattices [47]. Nevertheless, none of the mentioned experiments is capable to generate spherical three-dimensional dust clusters.

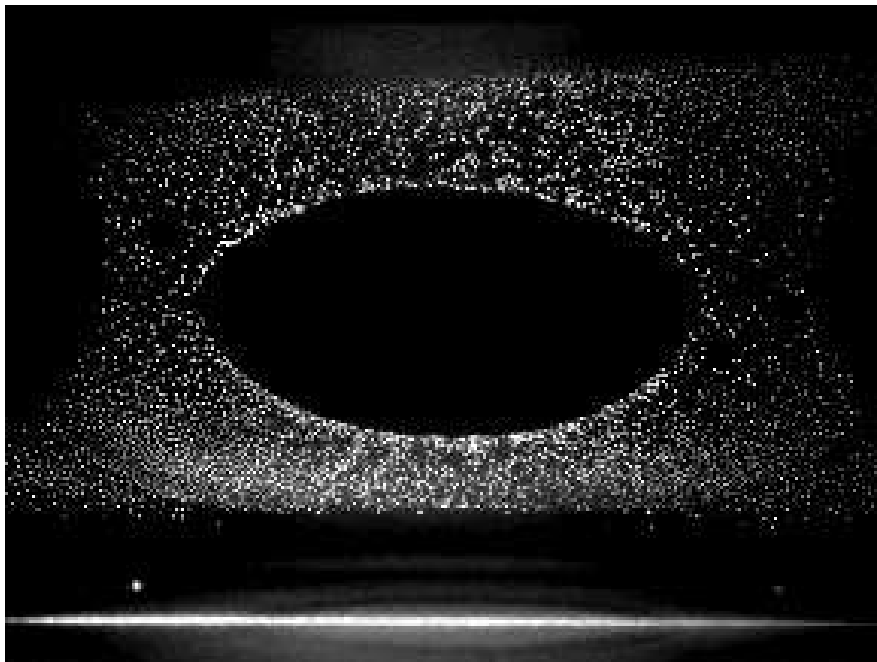


Figure 2.7: Gravity compensation by thermophoretic force yields an extended three-dimensional complex plasma affected by a large dust free region ("void") in the center of the discharge. From Ref. [27].

2.2.2 Three dimensional complex plasmas

To reduce the influence of gravity, which leads micrometer-sized particles to sediment into the lower sheath and to form flat pan-cake shaped dust clouds, it is possible to use smaller dust particles. Since the gravitational force F_g is proportional to the third power of the particle radius r_d , the influence of gravity decreases dramatically with respect to the confining electric force $F_E \propto r_d$ when using smaller particles. Thus gravity becomes negligible for particles in the nanometer range. Such particles are present, e.g. in reactive plasmas, where they grow inside the discharge and fill large parts of the plasma volume (e.g. Ref. [63,64]). Unfortunately, these complex plasmas are not well-suited for studying strongly coupled systems. On the one hand, the small dust charge in the order of a few elementary charges results in low values of the coupling parameter Γ and the system cannot be considered strongly coupled. On the other hand, the small size of the particles does not allow for an easy observation of the individual particle as it is required for structural investigations.

Consequently, experiments with three-dimensional complex plasmas consisting of micrometer-sized particles were performed under microgravity conditions in space [21–24] and on parabolic flights (e.g. Ref. [25,26]). An alternative approach yielding similar dust distributions in the laboratory under gravity conditions was presented by Rothermel *et al.* [27]. The authors generated a temperature gradient in the neutral gas of the discharge by heating the lower and cooling the

2.2. CONFINEMENT OF COMPLEX PLASMAS

upper electrode of a parallel plate rf reactor. This gradient causes an upwards directed thermophoretic force [65] acting on the dust particles, which is sufficiently strong to compensate for gravity in most parts of the discharge. A vertical section through the center of the resulting complex plasma (consisting of spherical dust particles with a diameter of $3.4 \mu\text{m}$) is shown in Fig. 2.7. Obviously, the dust is not homogeneously distributed in the complete volume but is disturbed by the presence of a large dust-free region in the center of the discharge, the so-called "void". This phenomenon is typical for experiments under microgravity conditions (e.g. Ref. [22, 25]) and is attributed to the radially outwards directed ion-drag force (see Fig. 2.3) [66–70]. Although, attempts were made to suppress the "void", these experiments are not sufficiently reliable so far and require unusual plasma conditions that limit the usable parameter range [71].

2.2.3 Other discharge geometries

Besides the discussed discharges in parallel plate rf reactors there are numerous other discharge types that allow for the confinement of complex plasmas. Barkan and Merlino [72, 73] confined elongated and spherical dust clouds in the double layer in front of an anode of a Q-machine. In this magnetized dc discharge, the low gas pressure and strong electric fields in the anodic plasma induces directed ion flows, which destabilize the confined dust cloud and excite waves. Consequently, this kind of experimental setup turned out to be well suited for the investigation of various wave phenomena in complex plasmas [72, 74].

The confinement of complex plasmas inside a DC discharge is not limited to anodic plasmas. Fortov *et al.* [31] observed almost spherical dust clouds confined inside an instability region (stratum) of the positive column of a DC glow discharge. However, the strong electric field that confines the dust, induces a directed ion flow, which leads the particles to arrange in chains as observed in the sheath region of an rf discharge.

Another interesting experiment was performed by Zobnin *et al.* [75]. The authors use an electrodeless inductively coupled rf discharge in a vertically aligned glass tube [see Fig. 2.8 (a)]. Here, the particles are confined vertically by strong electric fields in the transient region between the luminous plasma core and the neutral gas in the lower edge of the discharge. The lateral confinement is established by surface charges on the glass walls. The authors observed small comet-shaped dust clouds, i.e. a nearly spherical dust cloud (head) equipped with a long vertical tail of particles [see Fig. 2.8 (b)]. Apparently, the arrangement of the particles in the tail and even in the head [see Fig. 2.8 (c)] of the cloud is again dominated by vertical chains, which is a consequence of directed ion flow in this region of the discharge due to the confining electric fields.

Very recently, shortly after the successful confinement of spherical dust clouds within the context of this work [76], Annaratone *et al.* [77] presented an experiment, which is capable to confine three-dimensional finite spherical dust clusters. The authors use a parallel plate rf discharge where the lower electrode is divided into approximately 60 segments, which are independently operated with dc and rf

2. CONFINEMENT OF FINITE STRONGLY-COUPLED COULOMB SYSTEMS

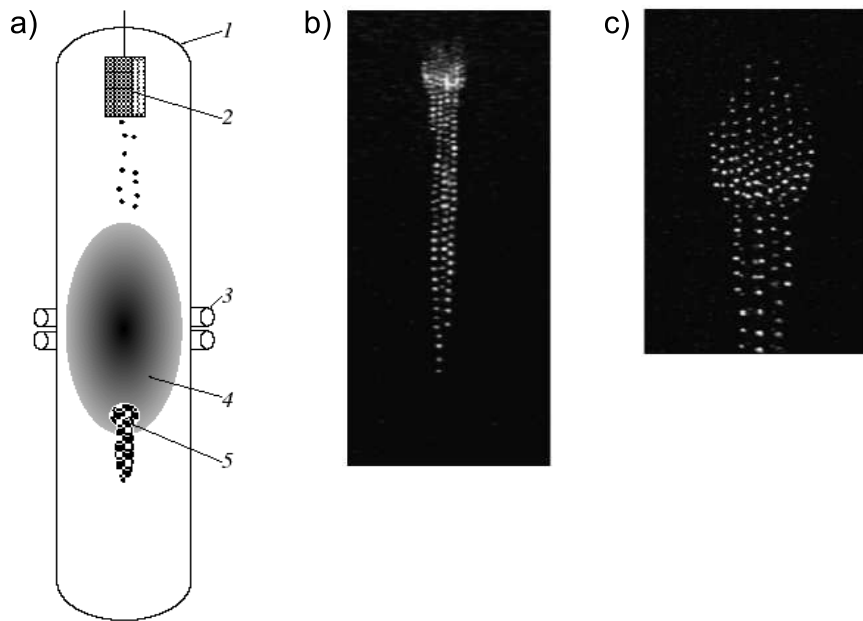


Figure 2.8: (a) Experimental setup by Zobnin *et al.* [75]: (1) discharge tube, (2) dust dispenser, (3) inductor, (4) plasma core, (5) confined dust cloud, (b) vertical section through a confined dust cloud and (c) close up of the head of the cloud. The figures are selected from Ref. [75].

voltages. By applying a suitable rf/dc combination to a central, millimeter-sized square segment, small spherical dust clusters were confined in an area of bright plasma glow above that electrode segment. The authors presented a structural analysis of small systems up to a cluster containing 13 particles and icosahedral structure. Besides these small clusters, the authors also successfully confined larger clouds with up to approximately 200 particles, although no structural analysis of these systems was made.

In summary, dust confinement in plasmas involves electric fields in space charge regions or from surface charges. The ion flow associated with the electric fields usually affects the confinement and structure the dust cloud.

3 The discovery of Coulomb balls

This chapter follows the historic sequence of experiments that led to the discovery of spherical dust clouds, so-called Coulomb balls. These dust clouds are confined inside a rf discharge under gravity conditions and do not suffer from non-isotropical order of the dust particles, as typical for complex plasmas confined by strong electric fields. The trap used to confine Coulomb balls is based on a suitable shaping of the plasma by means of dielectric walls in combination with a thermophoretic force to reduce the influence of gravity.

3.1 Experimental setup

All experiments within the context of this work were carried out in a discharge chamber called “Kleiner Topf”, which was developed and constructed by Homann [78] (IEAP, University of Kiel). Because of its simplicity this chamber has been intensely used for various investigations in complex plasmas (e.g. Ref. [20, 78]). In order to meet the current requirements numerous modifications have been applied to the chamber.

Schematic sections of the discharge chamber are shown in Fig. 3.1. In this asymmetric capacitively coupled rf discharge the plasma is generated by an oscillating electric field between a powered circular electrode in the lower part of the chamber and the grounded vacuum vessel. The powered electrode has a diameter of 17 cm and a distance of approximately 10 cm from the lid of the chamber. For an optical investigation of the discharge and the dust the chamber is equipped with five windows. Four of them are located in the side walls and one is in the lid, which can be removed to gain access to the interior of the chamber.

A pump station is connected via a manual butterfly throttle valve to the chamber. To minimize the disturbing influence of neutral gas flow on a complex plasma the gas inlet and the pump station are connected via the same port to the vessel. The neutral gas pressure inside the chamber is controlled by a coordinated adjustment of the manual gas inlet metering valve and the throttle valve. For all experiments the inert gas argon has been used at pressures between 20 Pa and 120 Pa.

The discharge is powered by a rf generator at a frequency of $f_{rf} = 13.56$ MHz. For all experiments only low rf amplitudes at the electrodes in the range of $U_{rf} = (20-30)$ V were used. A matching network transforms the output impedance

3. THE DISCOVERY OF COULOMB BALLS

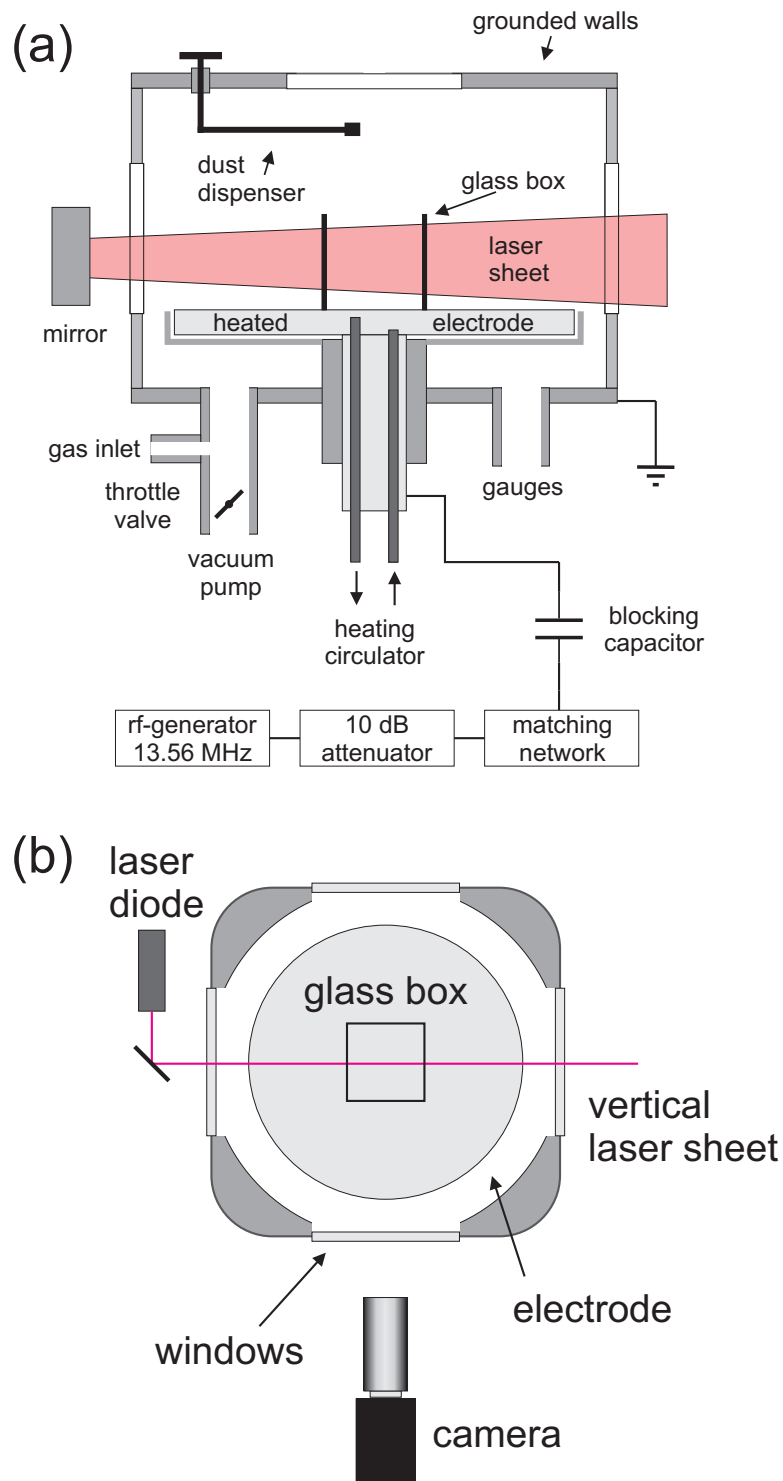


Figure 3.1: Vertical (a) and horizontal (b) section of the discharge chamber and the video microscopy setup.

3.1. EXPERIMENTAL SETUP

of the generator to the impedance of the discharge chamber to minimize the reflected rf power. Finally a blocking capacitor eliminates direct currents between the electrode and the other circuits. This allows the electrode to be biased. In most experiments the plasma generates a self-bias, but in some cases an external bias is applied. The typical plasma parameters are peak electron densities up to $n_e \approx 10^{15} \text{ m}^{-3}$ in the center of the discharge, electron temperatures of (2–5) eV and cold ions at room temperature. For a detailed description of the discharge properties see Ref. [78].

The most important change with respect to earlier experiments in this chamber is the use of a heated electrode. For this purpose, a heating circulator is connected to the hollow powered electrode, which allows for heating it up to $T_E \approx 95 \text{ }^\circ\text{C}$ with a stability of 0.05 K. This establishes a temperature gradient in the neutral gas between the electrode and the vacuum vessel at the temperature T_V . At the beginning of an experiment, T_V equals typically room temperature. Because the vacuum vessel is not actively cooled, T_V rises slightly with time. Thus, to maintain a stable temperature gradient, it is necessary to adjust the electrode temperature during the experiment at a rate of approximately 1 K/h.

Figure 3.2 gives an impression of the complete experimental setup. The discharge chamber is located on the left hand side on top of the table surrounded by cameras, lasers and miscellaneous mechanical components. The rack on the right contains most parts of the electronic equipment like rf generator, pressure gauges, computer etc., which is necessary to control the experiment and to handle the accumulated data.

3.1.1 Properties and handling of dust particles

In all experiments spherical melamine formaldehyde (MF) particles with diameters in the range of $d = (3-10) \text{ }\mu\text{m}$ manufactured by MICROPARTICLES [79] are used. This material has a mass density of $\rho_d = 1514 \text{ kg/m}^3$ and is highly resistant to mechanical stress as well as it withstanding temperatures up to $300 \text{ }^\circ\text{C}$. In the range of the used plasma conditions neither chemical reactions with the argon plasma nor significant material degradation due to sputtering etc. is observed. Thus it can be assumed that the particles keep their properties for the duration of an experiment. Figure 3.3 shows an image of the particles taken by a reflection electron microscope (REM). The particles have a highly uniform spherical shape with a very smooth surface, which simplifies the topology of the electric field surrounding such a particle when immersed in a plasma. This allows to use simple models for estimating the particle charge. However, the most important property with respect to complex plasmas is their excellent monodisperse size distribution with a coefficient of variance (C.V.) below 3%. This property makes the particles ideally suited for the production of regular plasma crystals. Due their identical size the particles have an identical mass and charge (assuming a uniform plasma density). Thus, the interaction potential is uniform, which is required for the formation of regular crystalline structures.

To inject these dust particles into the plasma, a salt-shakerlike device (dis-

3. THE DISCOVERY OF COULOMB BALLS

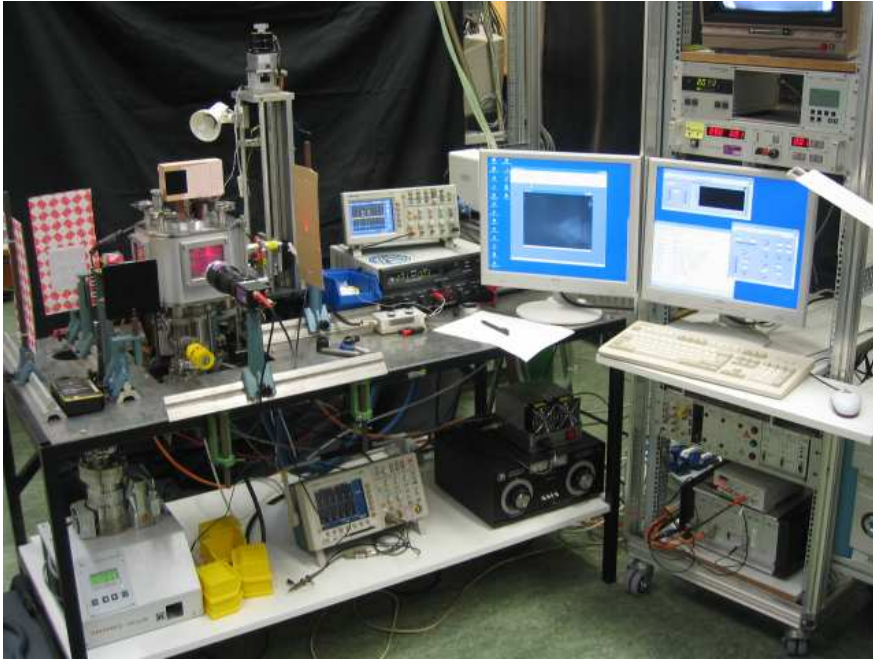


Figure 3.2: Picture of the experimental setup. The discharge chamber “Kleiner Topf” is located on the left side on top of the table.

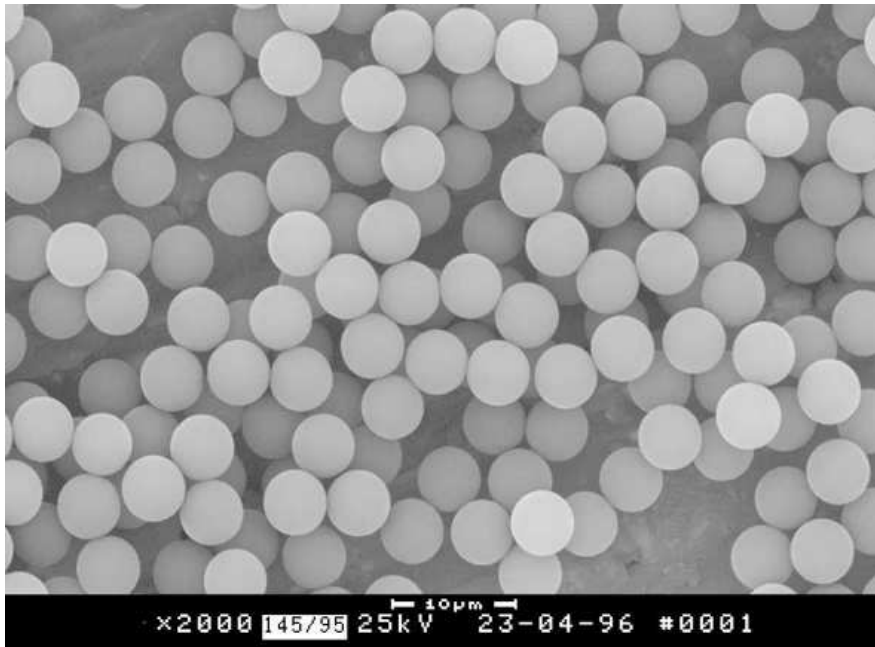


Figure 3.3: Image of dust particles taken by an electron microscope (REM). From Ref. [79].

3.2. FIRST EXPERIMENTS AND OBSERVATIONS

penser) is located below the lid of the discharge chamber. This dispenser consists of a metallic support, which can be swiveled via a rotational feedthrough to various positions in the chamber. A small container at the end of the support stores a reservoir of dust particles. By gently knocking against the support, a number of particles can be injected through a small hole in the bottom of the container into the discharge.

The detection of particles inside the plasma is done by a simple video microscopy setup as sketched in Fig. 3.1. A vertical laser sheet illuminates a thin slice of the complex plasma. It has a thickness of approximately 0.5 mm and is generated by a diode laser ($P_\lambda = 50$ mW, $\lambda = 660$ nm) and a cylindrical lens. The position of the laser sheet inside the chamber is adjustable by a mirror. A standard monochrome CCD video camera with a resolution of 768×576 pixels observes the scattered laser light of the particles at right angle. To achieve the necessary magnification ratio, the camera is equipped with a macro zoom lens, which allows for a minimum field of view of approximately 12×9 mm² within the laser sheet. To enhance the contrast of the recorded images the plasma glow is suppressed by a narrow-bandwidth interference filter, which is mounted in front of the macro lens. This filter is nearly transparent for the laser wavelength but suppresses almost all other light. For later analysis the video signal of the camera is recorded by a digital video recorder.

The intention of the following experiments was to observe the influence of the heated electrode on dust particles inside the discharge. Similar to the experiment of Rothermel *et al.* [27], here, complex plasmas with a large vertical extension were expected. A confinement based only on the positive plasma potential as utilized in symmetric parallel plate discharges with two powered electrodes (e.g. Ref. [22, 27]) is not possible in the present asymmetric type of discharge. Experiments dealing with two-dimensional complex plasmas in the present discharge geometry typically use flat metallic or dielectric barriers placed on top of the electrode to confine the particles horizontally [20]. Following this idea but expecting a much higher vertical extension of the particle cloud due to the effect of thermophoretic levitation it seemed promising to use a kind of transparent vertical tube for its confinement. Due to better optical properties and to reduce laser reflections a glass tube, actually a box, with a square cross-section is used. Figure 3.4 (a) shows a picture of a typical glass box with a side length of approximately 30 mm. The glass plates have a thickness of 2 mm and are combined by a small amount of vacuum-proof epoxy glue.

3.2 First experiments and observations

A top view of a glass box inside the plasma ($p = 50$ Pa, $U_{rf} = 30$ V) is shown in Fig. 3.4 (b). It has a side length of 30 mm and is placed at the center of the electrode. The plasma glow, which is separated by dark sheath regions from the dielectric walls, is present outside and inside the glass box. By slightly reducing the rf amplitude, a sudden change of the discharge mode occurs, which leads

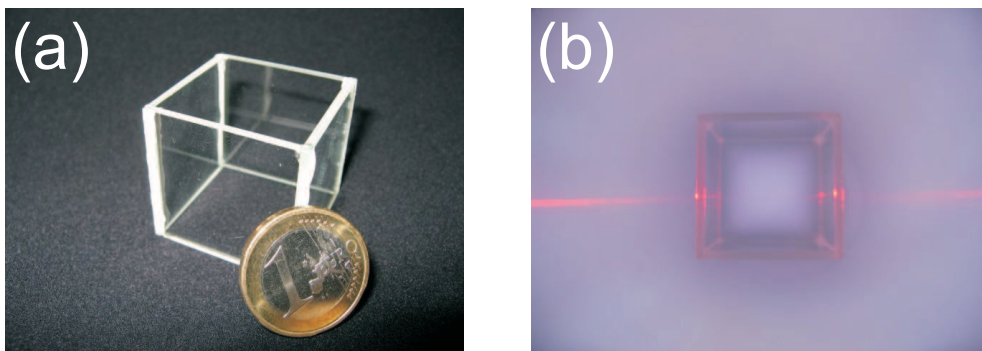


Figure 3.4: (a) glass box and euro coin and (b) topview of glass box inside the discharge.

the plasma glow inside the glass box to disappear abruptly, while the plasma outside is not significantly affected. Increasing the rf amplitude afterwards above a certain value, the glow inside the box abruptly returns. The threshold values of the rf amplitude at, which the glow inside the box appears and disappears show a hysteretic behavior. In addition, they have a significant dependence on the neutral gas pressure as both values rise with increasing pressure. Thus it is possible to initiate a transition between the discharge modes not only by a variation of the rf amplitude but also by changing the neutral gas pressure.

The behavior of the discharge is qualitatively understood. In the used gas pressure range $p \approx (20-100)$ Pa the energy is transferred into the plasma by *ohmic heating* [52]. Accordingly, the oscillating motion of the electrons inside the bulk plasma is dominated by frequent collisions with neutral gas molecules during each rf periode. Depending on the electron energy, these collisions result in excitation or ionization of neutral gas molecules. The energy of the electrons depends mainly on the electric field strength (rf amplitude) and the mean free path of the electrons (gas pressure). The energy gain is proportional to the ratio E/p [80]. Since the observed two modes are important in the further discussion, let the term *production mode* denote the mode with plasma glow, i.e. plasma production inside the glass box. The other case, where only a very dilute diffusive plasma is present, is characterized by the term *diffusion mode*.

3.2.1 Dust inside the glass box

Since the behavior of the plasma in the presence of the glass box is known, it is now time to determine the influence of both discharge modes on dust that is injected into the glass box. For these observations the dispenser is filled with relatively small dust particles ($d = 3.47 \mu\text{m}$) and is positioned approximately 5 cm above the glass box. The vertical laser sheet cuts the glass box in its center and illuminates the complete section of the box, which is observed by the camera.

Starting in the diffusion mode (at $p = 50$ Pa), i.e. with low rf amplitudes and without plasma glow inside the glass box, the injected particles fall directly down

3.2. FIRST EXPERIMENTS AND OBSERVATIONS

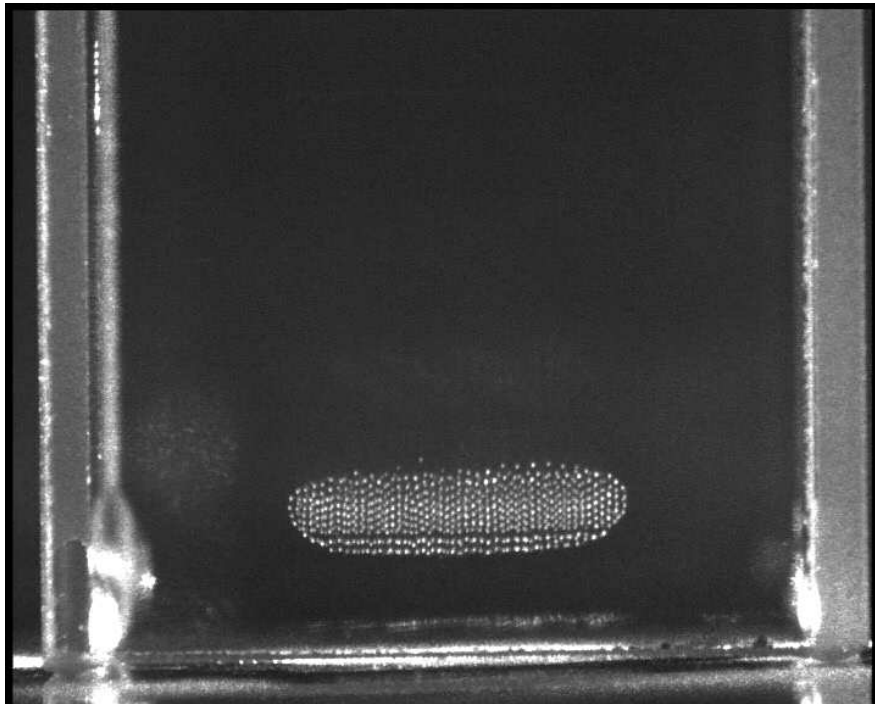


Figure 3.5: Flat crystalline dust cloud confined in the sheath of the discharge inside the glass box. The particles are aligned in vertical chains.

to the electrode and remain on its surface. This observation confirms that in the diffusive mode only a very weak plasma is present in the glass box, which is not capable to generate electric fields that are sufficient to confine the particles. Then, by increasing the rf amplitude, the discharge mode switches to production mode. The dust particles on top of the electrode are not affected by this change but remain there. Consequently, to prevent any distortion of the discharge by an insulating layer of dielectric dust particles on the electrode, these particles have to be removed regularly.

When in production mode, newly injected particles fall down until they reach the sheath region a few millimeter above the electrode. Here the charged dust is stopped and levitated due to the presence of strong electric fields. Gravity typically forces these particles to arrange in a thin layer or at larger particle numbers in flat dust clouds with a limited vertical extension. An example of such a dust cloud is shown in Fig. 3.5. The two bright vertical bars on the left and right hand side of the image are the walls of the glass box. The regular arrangement of the particles indicate a crystalline state of the complex plasma. As typical for dust clouds in the sheath above an electrode, the particles are arranged in vertical chains, as a consequence of a directed ion flow to the electrode. When the size of the dust cloud inside the glass box overcomes a certain critical value the discharge switches to diffusion mode due to high plasma losses to the surface of the dust particles. It remains to mention that dust particles initially confined in

the sheath region fall abruptly down to the electrode when the discharge switches from production to diffusion mode.

All the observations in this section were made at a fixed neutral gas pressure of 50 Pa. Nevertheless, a variation of the pressure does not change much qualitatively. However, at gas pressures below approximately 20 Pa, the low damping of the particles motion by the neutral gas yields liquid and gaseous complex plasmas inside the box, which are not desired in the context of this work.

3.2.2 Heating of the electrode

In the previous sections the effect of the glass box on the discharge and the behavior of dust particles was investigated. It is now time to return to the actual goal of these experiments, namely the investigation of the influence of a heated electrode on a confined complex plasma.

For this purpose the discharge is operated at a neutral gas pressure of 50 Pa and moderate rf amplitudes in production mode. At the beginning of the experiment the electrode temperature equals room temperature and the dust particles form a flat dust cloud in the sheath above the electrode [see Fig. 3.6 (a)]. Then the heating is switched on, which leads the electrode temperature to rise by a rate of approximately 0.2 K/s. Shortly after beginning of heating, the lower particles of the cloud start to retreat horizontally from the center towards the sides of the cloud [see Fig. 3.6 (b)]. As the temperature further increases the number of particles in the outer region grows [Fig. 3.6 (c)] until no particle remains in the center and the dust forms a torus-like structure [Fig. 3.6 (d)]. Beginning with a certain temperature (here, $T_E \approx 58$ °C) the dust particles inside the torus-shaped cloud begin a poloidal vortex motion, which is indicated by the arrows in Fig. 3.6 (e). The rotation of these vortices is always directed upwards in the center and downwards in the vicinity of the glass walls. With rising electrode temperature, the vortices get more and more elliptic, with their major axes tilted upwards towards the center of the glass box. At very high temperatures, i.e. up to $T_E \approx 94$ °C in Fig. 3.6 (h), both vortices connect in the center of the glass box to a dome-shaped dust cloud. Due to the counter rotation of the vertices the particles in the central region of the merged cloud are stationary, whereas in the outer regions of the cloud is dominated by the vortex motion. Such vortices in a complex plasma are also observed in other experiments (e.g. Ref. [22]). The presence of stationary particles in the center of the glass box, convection can be excluded as possible driving mechanisms [81]. Here, the formation of vortices is attributed to a weak inhomogeneity of the particle charge within the dust cloud in combination with the presence of non-electrostatic forces, like gravity, thermophoretic and ion-drag force [82]. In addition to the shape of the confined dust cloud, its vertical position is significantly affected by the electrode temperature. Obviously, the average levitation height of the cloud increases with the electrode temperature.

At first sight, these findings seem to be somewhat disappointing, as it was expected to see an extended dust cloud similar to those of other experiments [27]

3.2. FIRST EXPERIMENTS AND OBSERVATIONS

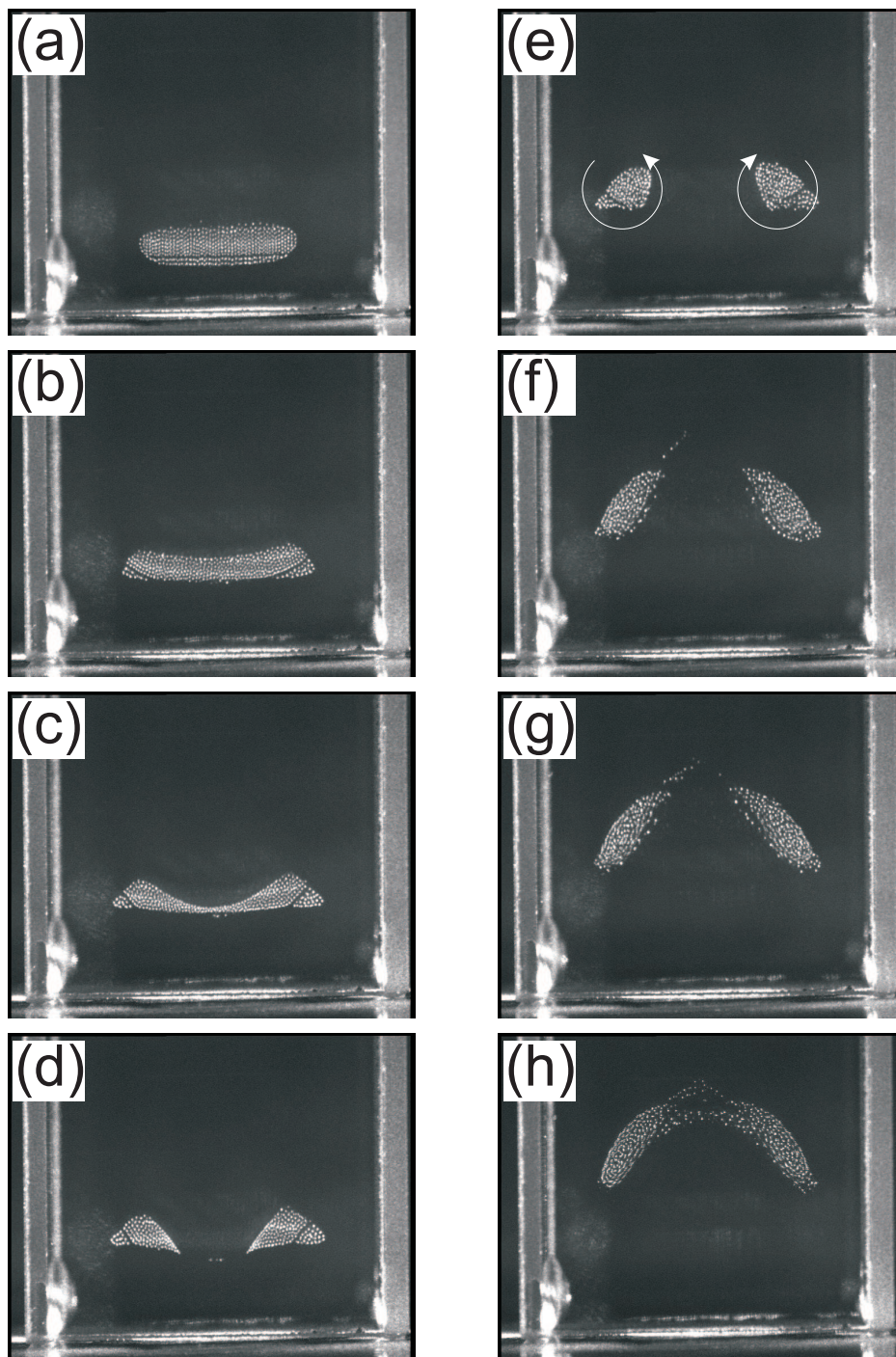


Figure 3.6: Dust confined in the glass box at different electrode temperatures [from (a) $T_E \approx 22$ °C to (h) $T_E \approx 94$ °C]. Beginning at a certain temperature ($T_E \approx 58$ °C) the torus-shaped dust cloud is affected by a poloidal vortex motion of the dust particles [(e)-(h)].

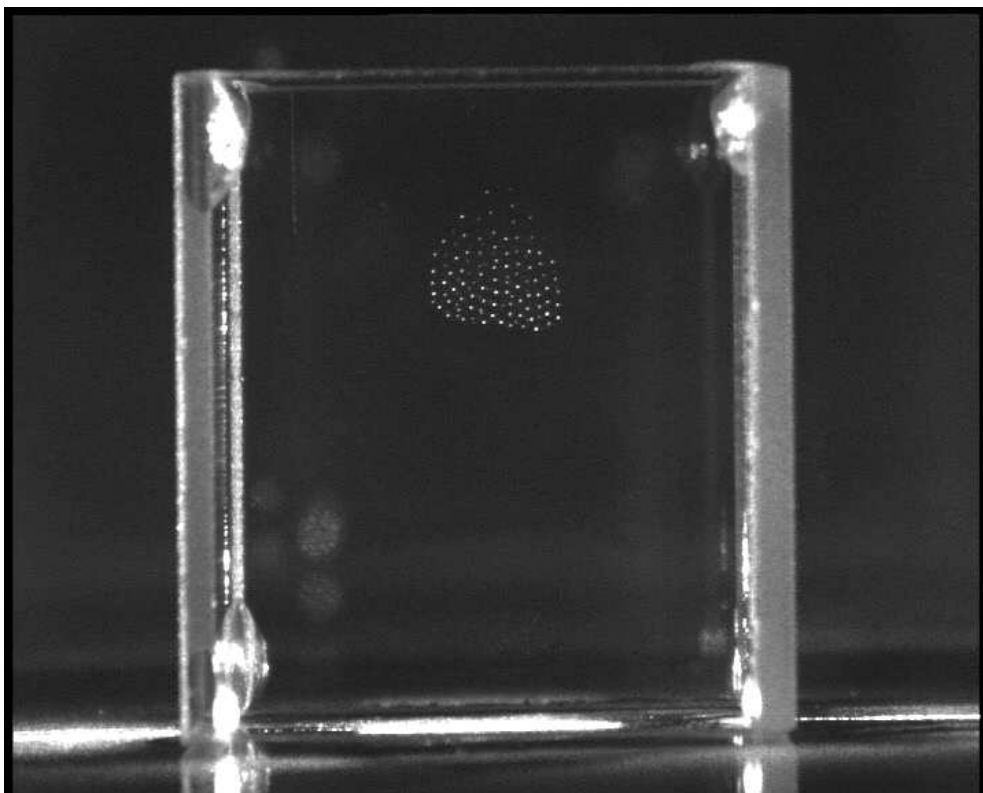


Figure 3.7: A small compact dust cloud confined in the upper region of the glass box.

using thermophoretic levitation. Hoping to get better results and to utilize the large parameter space, in a second run the electrode temperature is kept fixed at a moderate value of $T_E \approx 75^\circ\text{C}$ while the rf amplitude is varied. The experiment starts with a moderate amplitude in production mode and the particle distribution is similar to Fig. 3.6 (f). By slowly increasing the rf amplitude the particles are concentrated stronger in the lower outer regions of the glass box. A further increase of the amplitude does not change this behavior. In a second step the rf amplitude is set back to its initial value, thus the dust particles are located in the lower outer region of the glass box forming vortices. When the rf amplitude is afterwards lowered the dust vortices expand continuously towards the center of the glass box until both vortices almost touch each other in the center [similar to Fig. 3.6 (h)].

A further reduction of the rf amplitude leads to a sudden transition to diffusion mode. Completely unexpected and in contrast to the earlier described case without a heated electrode, the dust particles now ascend to the upper region of the glass box. Here they form a drop-shaped compact dust cloud (see Fig. 3.7) without any significant particle motion. The large vertical extension of the cloud and its location inside the glass box, suggests that compensation of gravity by thermophoretic force as a consequence of the heated electrode plays a significant

3.3. SPHERICAL DUST CLOUDS

role. A further reduction of rf amplitude leads the cloud to expand while its vertical position increases and finally to a complete decomposition by particles smoothly flowing down to the electrode. Once the diffusion mode is established and the dust forms a compact cloud the rf amplitude can be increased again by a certain amount without destroying the cloud. This causes a compression of the dust cloud, while its levitation height decreases. By this means, the size of the confined cloud and thus the distance between the individual particles is variable by approximately up to 30 %.

These findings show, that it is possible to confine compact dust clouds under gravity conditions that apparently do not suffer from the influence of gravity and void effects and may be well suited to investigate crystalline bulk order in complex plasmas.

3.3 Spherical dust clouds

Inspired by the described observations a survey started with the goal to optimize the experimental parameters like plasma conditions, electrode temperature as well as the size of the glass box and the particles in order to generate a dust cloud that is best suited for further experiments. Within these experiments it was found that, with a carefully selected set of experimental parameters, it is possible to generate almost perfect spherical dust clouds. To get an impression of the three-dimensional shape of such a cloud a number of consecutive vertical sections were recorded by tilting the laser mirror about its vertical axis. For this measurement, the field of view of the camera was adjusted to the size of the cloud in order to improve the optical resolution. The recorded sequence of images is shown in Fig. 3.8. Each image displays an area of approximately $12 \times 9 \text{ mm}^2$. As the laser sheet touches the front of the cloud [Fig. 3.8 (a)] only a few particles in the center of the field of view are visible. The number of visible particles increases while approaching the center of the cloud [Fig. 3.8 (b)-(c)] and decreases afterwards [Fig. 3.8 (d)-(e)] before reaching the back side of the cloud [Fig. 3.8 (e)]. All sections of the cloud are almost circular, i.e. the three-dimensional shape of the cloud is spherical due to the symmetry of the glass box. In addition, it is obviously neither affected by a void nor dominated by the formation of vertical particle chains. The observation of the recorded video material also shows that the weak thermal jitter of the particles is very rarely superimposed by sudden hopping motions of single particles. This suggests an almost solid state of the cloud with crystalline ordering of the particles.

Encouraged by these findings, further experiments were tackled in order to reveal the properties of these spherical dust clouds, so-called Coulomb balls, and their trap in detail.

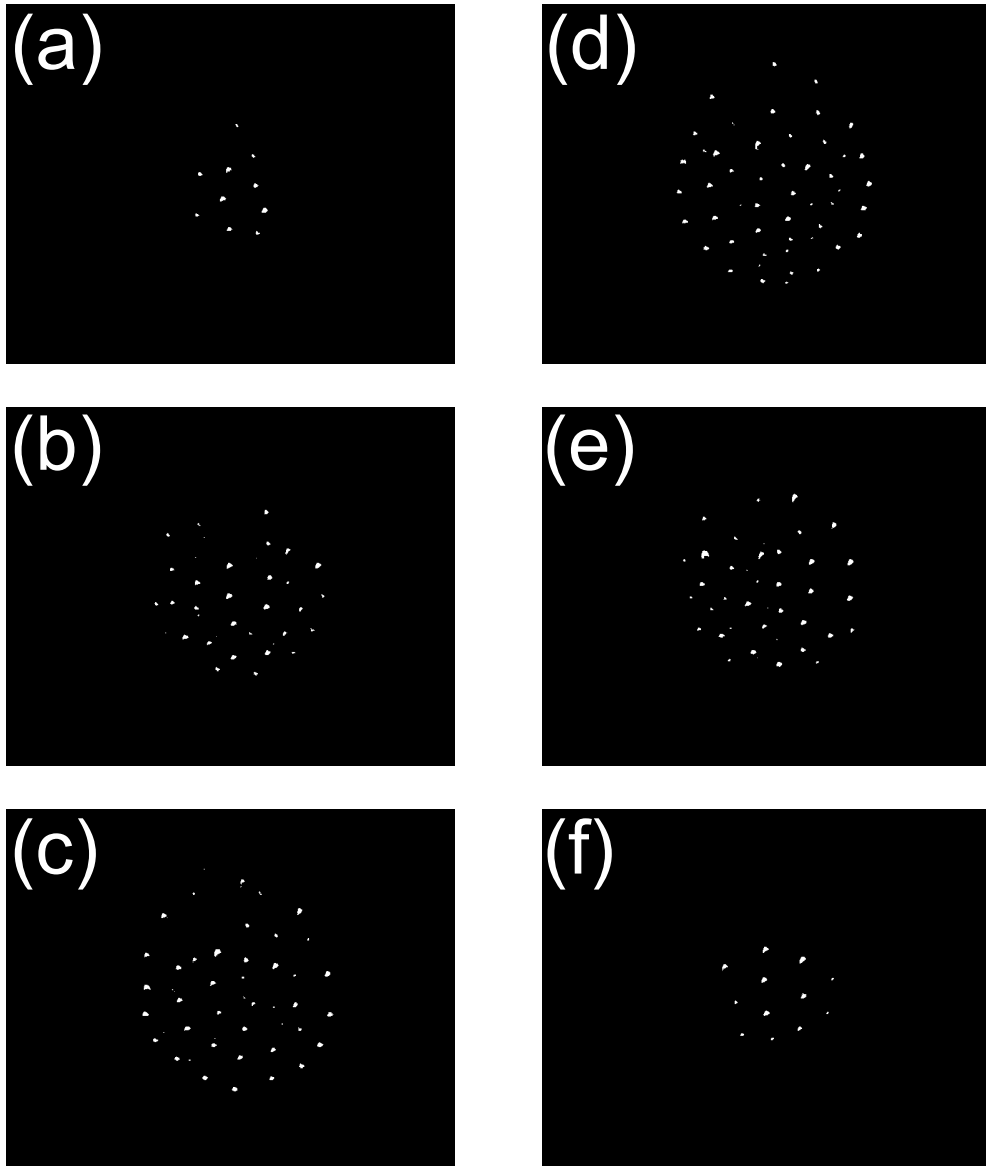


Figure 3.8: Consecutive vertical sections of a dust cloud confined in the glass box. The laser sheet moves from the front of the cloud (a) through the center (b)-(e) to the back-side (f). All images have the same field of view of $12 \times 9 \text{ mm}^2$.

4 Structure of Coulomb balls

With the discovery of Coulomb balls numerous questions arised concerning the structure of these spherical dust clouds. First, the probably most basic question concerns the phase of the complex plasma. In the case of a crystalline cloud the arrangement of the particles is of great interest. Since the actual plasma conditions inside the trap are not exactly known it is to clarify whether the structural order is affected by non-isotropic phenomena as observed, e.g. in the sheath region of a plasma (see Sec. 2.2.1). Finally, it stands to reason to search for dynamical phenomena within the cloud. To allow for a detailed analysis of their internal structure an additional diagnostic tool is required, which yields the three-dimensional position of each dust particle.

4.1 Scanning video microscopy (SVM)

A way to determine the three-dimensional positions of the dust particles inside a complex plasma is the so-called *Scanning video microscopy* (SVM) method. It is an established tool in complex plasmas (e.g. Ref. [26, 32]) and actually an automatic and more sophisticated version of the previously described manual scan through a dust cloud by tilting the laser sheet (see Sec. 3.3). The modified setup is shown in Fig. 4.1. In addition to the previous setup, a second laser ($P_\lambda = 50$ mW, $\lambda = 682$ nm) with a separate camera is added to the experiment. Again, the laser generates a vertical laser sheet and is mounted at right angle together with the second camera on a motorized translational stage, which is aligned parallel to the optical axis of the camera. As before, the focal plane of the camera lies within the laser sheet. The rigid connection between the camera and the laser guarantees that their relative position does not change when positioning the laser sheet inside the observed dust cloud by moving the translational stage. Hence, in contrast to the previously described method, here parallel sections are recorded. Thus, the camera is always focused to the illuminated particles and yields sharp images in the complete field of view. This is necessary for a precise analysis of the data. The translational stage is equipped with a stepper motor, which is controlled by a computer. By moving the horizontal stage continuously subsequent vertical sections of a confined Coulomb ball are recorded. The analysis of these images yields a three-dimensional reconstruction of the observed cloud.

The spatial resolution of this diagnostic is obviously defined by the pixel resolution of the camera, by the width of the laser sheet, and by the displacement

4. STRUCTURE OF COULOMB BALLS

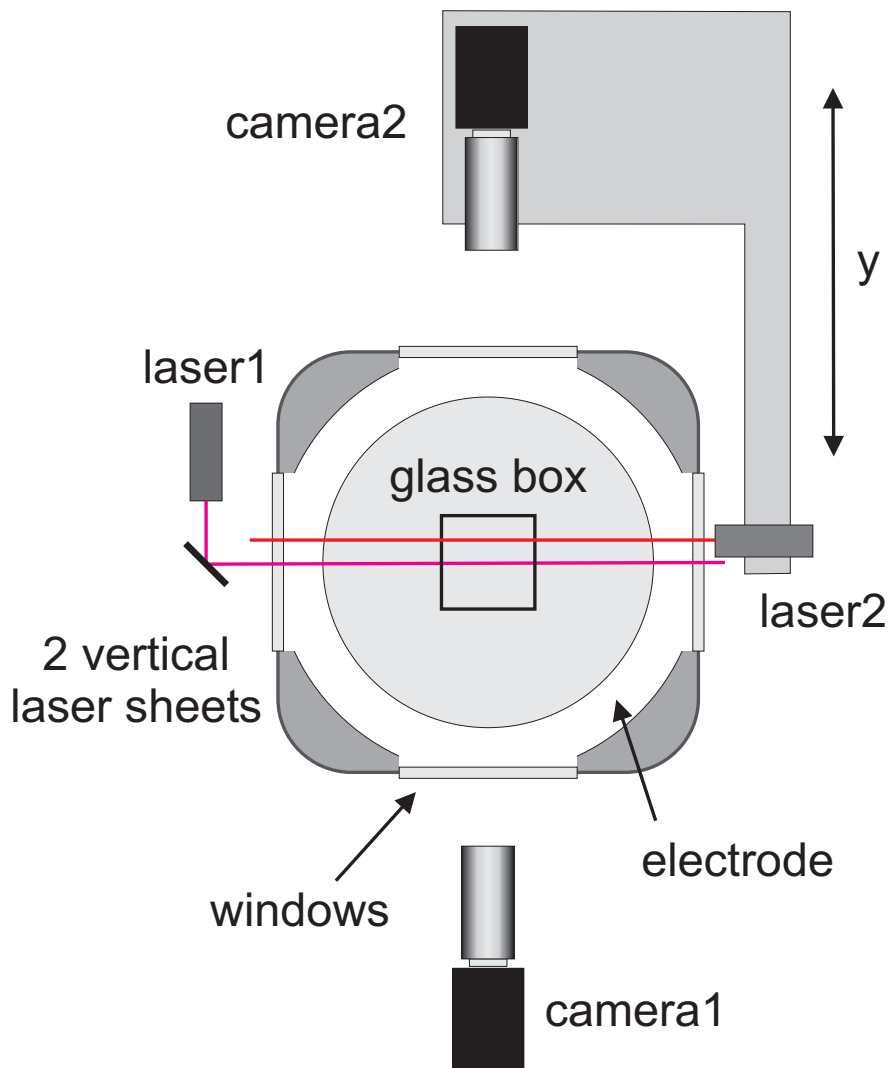


Figure 4.1: Top view of the discharge chamber with the original video microscopy setup (laser1, camera1) and the added scanning video microscopy diagnostic (laser2, camera2). Both diagnostics use different laser wavelengths to prevent disturbances.

between subsequent sections. In the present setup a digital monochrome CCD camera with a resolution of 640×480 pixel and a maximum frame rate of 40 fps is used. The images taken by the camera are digitally stored for off-line analysis. Due to the high sensitivity of the camera and a graylevel resolution of 10 bits in combination with a fix-focus high aperture lens (50 mm/f1.2) the optical system allows for a wide range of adjustments with respect to the field of view and image quality without suffering from low light intensity. As in the original setup, the lens is equipped with an interference filter centered on the laser wavelength. Since the SVM setup uses a different wavelength, both diagnostics can be used simultaneously. To utilize the resolution of the sensor the field of view is adjusted

4.1. SCANNING VIDEO MICROSCOPY (SVM)

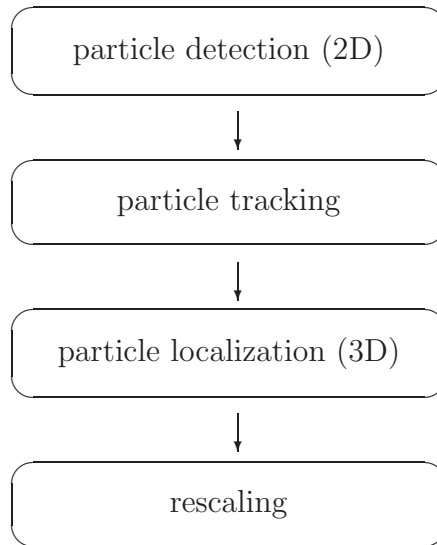


Figure 4.2: The analysis of the PIV data is divided into four steps.

to match the size of the observed Coulomb ball. Besides the pixel resolution the adjustment of the lens has a significant influence on the effective accuracy of this diagnostic. Since the proper adjustment is strongly dependent on the applied method of analysis, this topic is addressed in the following section.

The resolution along the axis of the optical system depends in principle on the profile of the laser sheet and on the depth of focus, which is given by the properties of the lens. However, since in the present setup the depth of focus is always larger than the width of the used laser sheet, the lens does not affect the axial resolution. To ensure the detection of all particles when scanning with the laser sheet through a dust cloud it is necessary to have an overlap of the laser profiles in consecutive images. Consequently, the width of the laser sheet must not be smaller than the axial displacement between these sections. By using a laser sheet with a Gaussian intensity profile perpendicular to its plane the width of the sheet can be chosen sufficiently large although a precise estimation of the axial position of the particles is still possible by analyzing their intensity evolution when moving the sheet. In the present setup the laser sheet has a mostly constant intensity distribution in the plane and a half-width of $\approx 100 \mu\text{m}$. Typically, the stage propagates with a constant velocity $v_y = 0.5 \text{ mm/s}$. By utilizing the maximum frame rate of the CCD camera this velocity results in a displacement of $\Delta y = 12.5 \mu\text{m}$ between two successive sections. Since a complete scan of a typical Coulomb ball consists of 400–500 sections it takes approximately 10 s to scan the complete cloud.

4.1.1 Data analysis

The recorded sequence of images is analyzed by using a special *MATLAB* code written by Block [83]. According to Fig. 4.2 the analysis is divided into four steps.

The first step performs the *particle detection* in the two dimensions of each section. It provides two-dimensional coordinates and the intensity of each detected particle within a single section. As in most particle detection algorithms the basic idea is to apply a threshold operator to the image, which marks those pixels that overcome a certain threshold value of intensity. Then connected regions of such pixels are assumed to correspond to a single dust particle and are analyzed separately to derive the desired properties of the particle. The position of a particle within the image plane (x - z) is derived by calculating the center of mass of the pixel values in the considered region. In addition, a measure of the intensity of a particle is derived by typically adding up all corresponding pixel values. To get its position with high (sub-pixel) accuracy, it is favorable when a particle is not imaged by a single pixel but by an extended region. Consequently, depending on the quality of the lens, a slight defocusing of the particles might result in a better accuracy. However, since the particles are point sources, the optical system is susceptible to lens errors especially comatic aberration. This results in asymmetrically deformed images of the individual particles, which reduces the accuracy of the analysis and has to be minimized by a proper adjustment of the lens. Another crucial topic in performing the particle detection is the selection of the threshold value. Typically, the background of the images is not homogeneously dark but distorted due to light reflections and a residual fraction of plasma glow. Since it is desirable for the following steps of the analysis to detect as many particles as possible, an adaptive algorithm was implemented. It uses multiple threshold values for the analysis of each section, which allows to increase the reliability and the number of detected particles significantly.

After the particle detection is applied to every section of the observed dust cloud the analysis proceeds with the second step. Because each particle is visible in multiple sections the *particle tracking* algorithm uses the data of the previous step to track each particle from one section to the next to prevent multiple counting of a particle. This is done by considering sequentially each particle of one section and searching for the nearest particle in the following section. If the distance is smaller than typically 5 pixel, then both particles are regarded identical. To eliminate accidentally detected noise or disturbed data due to particle motion a detected particle is only considered a real particle if it occurs in multiple sections. However, the algorithm does not require a particle to be visible in a connected set of sections since the (thermal) motion perpendicular to the laser sheet typically leads a particle to disappear from one section to the next and to reappear later. With the used algorithm the typical error of the resulting number of real dust particles is below 1 %, which was verified with simulated data. This step of analysis provides the total number of particles including their intensity evolution during the scan.

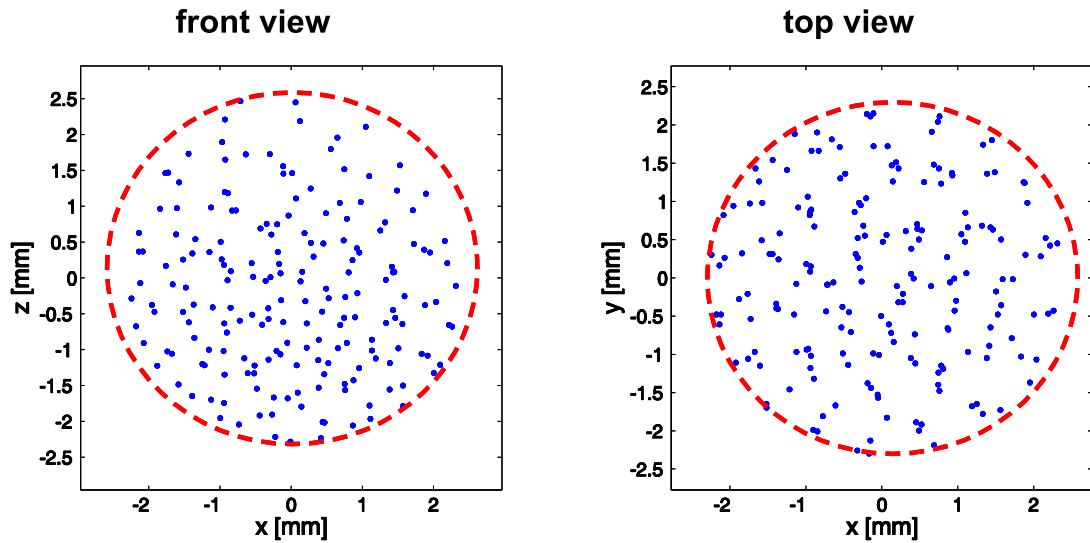


Figure 4.3: Front and top view of a reconstructed Coulomb ball containing $N = 190$ particles. The shape of the cloud is in both projections circular (dashed lines).

The third step of the data analysis performs the actual *particle localization* in three dimensions. Here, the intensity evolution of each particle is analyzed to derive its axial position y . Therefore, a model function, typically an inverted parabola, is fitted to the intensity evolution of each particle. By finding the maximum value of this functions the axial position is derived with a typical uncertainty of ± 2 sections, i.e. $\approx \pm 30 \mu\text{m}$. This is approximately one magnitude less than the expected inter-particle distance. The result of the particle localization algorithm is a set of three-dimensional coordinates corresponding to the particles of the observed dust cloud.

So far, the derived particle coordinates are given in arbitrary units (e.g. pixels, steps) depending on the properties of the used camera and the mechanical components. Finally, to allow for a physical analysis of the data *rescaling* is made to fit the real world dimensions. Thus, in the end a list of three-dimensional real world coordinates is obtained, which is the basis for all further structural analysis.

4.2 Global properties

The three-dimensional reconstruction of a Coulomb ball containing $N = 190$ particles ($d = 3.47 \mu\text{m}$) is plotted in Fig. 4.3. It shows two projections of the particle positions, one in the x - z plane (front view) and the other in the x - y plane (top view). Every dot corresponds to a single dust particle. As indicated by the dashed circles the shape of the cloud is in both projections circular with a diameter of $d_{CB} \approx 5 \text{ mm}$, i.e. in three dimensions the shape of the cloud is spherical. The distribution of the particles in the projections is mostly homogenous, although

4. STRUCTURE OF COULOMB BALLS

the front view suggests imperfections and a slightly reduced particle density in the upper region of the Coulomb ball.

With respect to the question of structural order, obviously the estimation of the coupling parameter Γ should yield interesting information. Unfortunately, the actual plasma conditions and therefore especially the dust charge is not precisely known. A rough estimation considering different charging models [18, 84] yields a range $800e \lesssim q_d \lesssim 8000e$ for possible values of the dust charge in the present situation. This results in a range for the coupling parameter $80 \lesssim \Gamma \lesssim 8000$. When assuming a realistic shielding strength $\kappa \approx 0.5$, then a value $\Gamma \gtrsim 287$ is required for a crystalline phase in a homogeneous system. Consequently, the coupling parameter is not a suitable measure to obtain information concerning the phase of the Coulomb ball.

Other methods yield interesting and more reliable information about the ordering of the particles. To get a first impression of the structural order of the particles within the cloud the *pair distribution function* (PDF) [85]

$$g(r) = \frac{V}{4\pi r^2 N^2} \left\langle \sum_i \sum_{j \neq i} \delta(r - r_{ij}) \right\rangle \quad (4.1)$$

is calculated. Here is $i, j \in [1 \dots N]$, V the volume of the cloud and $r_{ij} = |\vec{r}_i - \vec{r}_j|$ the distance between the i -th and j -th particle. Since only the distance, but not the orientation of the particles is considered, the term $4\pi r^2$ accounts for the increasing probability of finding particles at larger distance r , when assuming an infinite isotropic system. The PDF is a measure of local spatial order and yields a kind of average probability of finding a particle at the distance r to an arbitrarily chosen other particle. In the case of randomly distributed particles and an infinitely extended system the PDF equals 1 for all values of r . Considering an infinite three-dimensional system with ideal regular crystalline lattice without defects $g(r)$ shows periodic distinct delta peaks as a consequence of long range correlation. However, in the real world these peaks are broadened by thermal effects. In addition, the presence of defects in the crystal lattice results in a decrease of the modulation depth with increasing r . In the case of a finite spherical Coulomb ball with a diameter d_{CB} the pair distribution function decreases with r until $g(r > d_{CB}) = 0$. In Fig. 4.4 $g(r)$ is plotted for the observed cluster (measured data) and for randomly distributed particles within the same volume. As expected, the curve of the random distribution decreases steadily from $g(0) \approx 1$ to $g(\gtrsim 5 \text{ mm}) = 0$. In contrast, the pair distribution function of the Coulomb ball is almost 0 for $r \lesssim 0.6 \text{ mm}$, then it rises abruptly to a maximum value at $r_{max} = 0.714 \text{ mm}$, where $g(r_{max}) \approx 1.3$. Thus, the probability of finding a particle that is located closer than r_{max} is almost zero. Considering Coulomb repulsion between the particles this observation is expected and r_{max} can be identified with the average nearest neighbor or *inter-particle distance* b . With increasing distance $g(r)$ decreases below the value of the random distribution until it again reaches a second much smaller maximum at $r \approx 2b$. This significant modulation of the pair distribution function can be considered a first indication of crystalline order

4.2. GLOBAL PROPERTIES

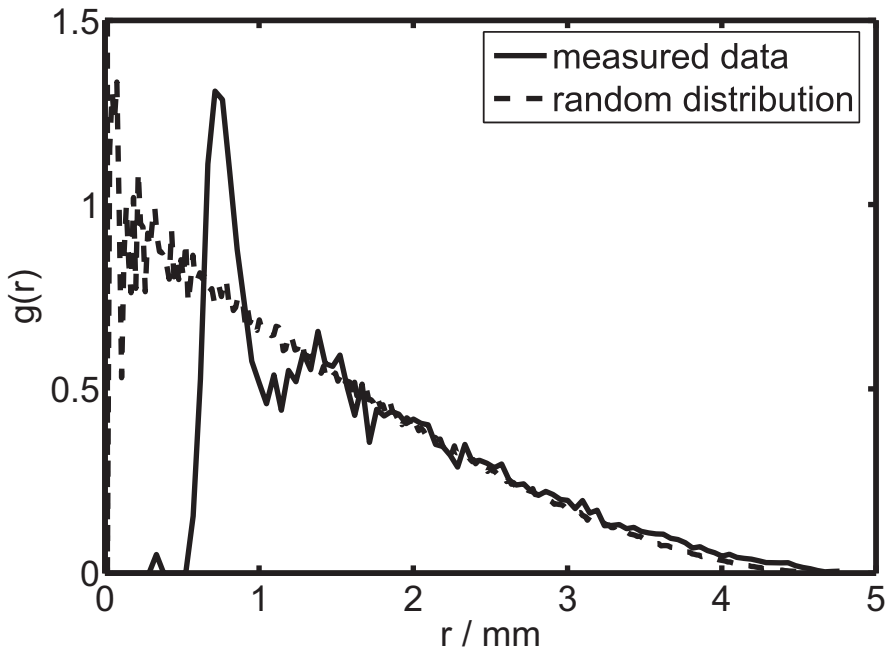


Figure 4.4: Pair distribution function $g(r)$ of a Coulomb ball containing $N = 190$ particles (measured data) and of a random distribution within the same volume.

with in the Coulomb ball. In addition, using the derived inter-particle distance and the approximation

$$n_d \approx \frac{N}{\frac{4}{3}\pi \left(\frac{d_{CB}+b}{2}\right)^3} \quad (4.2)$$

yields the number density $n_d \approx 2.8 \text{ mm}^{-3}$ of the dust and with Eq. (2.2) the Wigner-Seitz radius $a_{ws} \approx 0.44 \text{ mm}$ in the observed cloud. The ratio $b/a_{ws} \approx 1.62$ is dependent on the structural order of the system. In the case of an ideal hcp lattice a value $b/a_{ws} \approx 1.63$ is expected [47]. However, the good agreement with the experimental value is not a sufficient indication of this kind of structure within the Coulomb ball.

A criterion that defines the melting transition and can be used as a limit for crystalline order is the *Lindemann criterion* [86]. Accordingly, a system melts when the root mean square amplitude δ_{rms} of the particles thermal motion exceeds 10 % of the inter-particle distance b . By analyzing a video of a vertical section through the center of the presented Coulomb ball and assuming isotropic thermal motion the oscillation amplitudes of the particles are determined. Figure 4.5 shows a histogram of the oscillation amplitude δ in units of the inter-particle distance b . The distribution of the amplitude values is relatively narrow with a root mean square value $\delta_{rms} \approx 0.058 b$ and a standard deviation $\sigma = 0.014 b$. Hence, the root mean square amplitude δ_{rms} is below 6 % of the inter-particle distance. Consequently, according to the Lindemann criterion, the cloud is expected to be in crystalline phase.

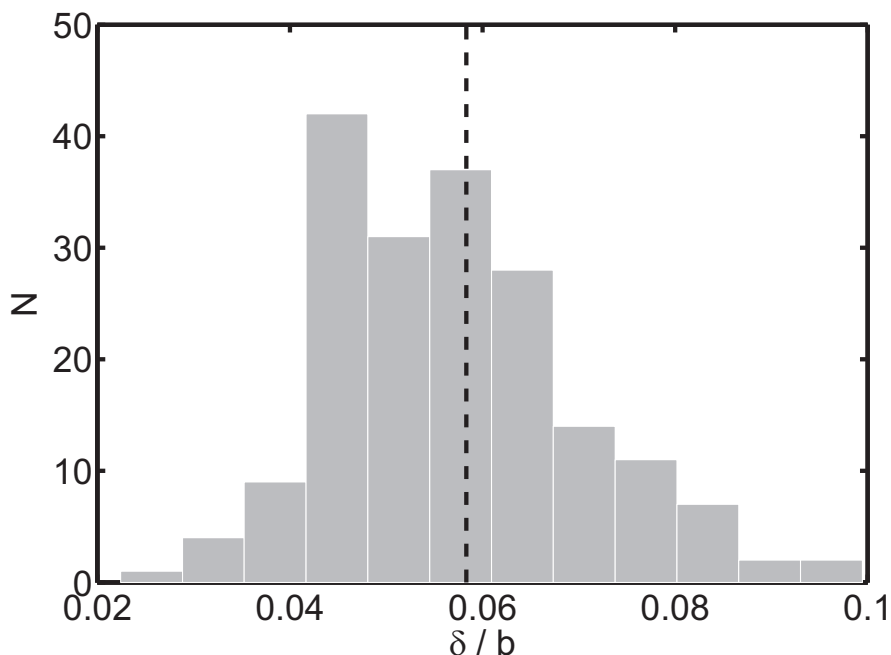


Figure 4.5: Oscillation amplitude δ of the particles thermal motion in units of the average inter-particle distance $b = 0.714$ mm. The dashed line indicates the root mean square amplitude $\delta_{rms} \approx 0.058 b$.

4.3 Shell structure

Motivated by the observed structural properties of trapped ion clusters in Paul and Penning traps, where the ions are arranged in concentric nested shells [5, 38] a similar internal structure of Coulomb balls is conjectured. Despite obvious similarities of these systems, significant differences are expected due to the shielding of the plasma in the case of Coulomb balls. To check for a shell structure the particle coordinates of the observed Coulomb ball are transformed into cylindrical coordinates

$$\begin{aligned} \rho &= \sqrt{(x - x_c)^2 + (y - y_c)^2} \\ \varphi &= \arctan\left(\frac{y - y_c}{x - x_c}\right) \\ z &= z - z_c, \end{aligned}$$

where (x_c, y_c, z_c) is the position of the center of the dust cloud. Using this coordinate system and projecting all particles into the ρ - z plane yields Fig. 4.6, which shows that the particles are indeed arranged in distinct nested shells, an unusual kind of structural order in complex plasmas. Shell formation was only observed as dust rings in two-dimensional clusters [19, 20] or in the vicinity of a Langmuir probe under microgravity conditions [25]. Four shells are visible with an almost constant inter-shell distance. The dashed lines correspond to perfect spherical shells that were fit to the data. In the lower part of the Coulomb ball

4.3. SHELL STRUCTURE

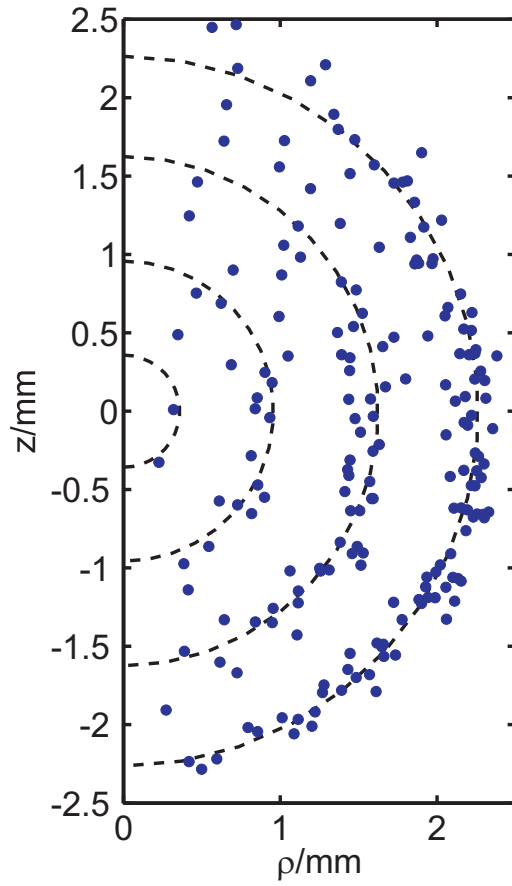


Figure 4.6: A Coulomb ball containing $N = 190$ particles projected into the ρ - z plane of cylindrical coordinates. The particles are arranged in distinct nested shells.

the shells are clearly separated by almost particle-free gaps, whereas in the upper part of the cloud, more particles are observed at inter-shell locations. This finding is consistent with the previously observed (see Fig. 4.3) slightly distorted particle distribution in the upper part of the cloud. However, the apparently reduced particle density at small values of ρ in Fig. 4.6 is not a property of the Coulomb ball, but only a geometric phenomenon due to the chosen coordinate system. The visibility of the shells within this plot depends crucially on the values (x_c, y_c, z_c) , which have to be chosen carefully. A first approximation of these values is to take the center of mass of the dust cloud as origin of the coordinate system. However, slight inhomogeneities in the dust distribution and deviations from an ideally spherical shape of the cloud result in a slightly different location of the center of the shells.

A deeper insight into the radial distribution of the particles yields the *radial particle distribution function*. It is a histogram of the radial positions $r = [(x - x_c)^2 + (y - y_c)^2 + (z - z_c)^2]^{1/2}$ of all particles of the cloud, i.e. it yields the number of particles located in a certain interval about r (see Fig. 4.7). As seen in the previous observation the particles are concentrated at certain ra-

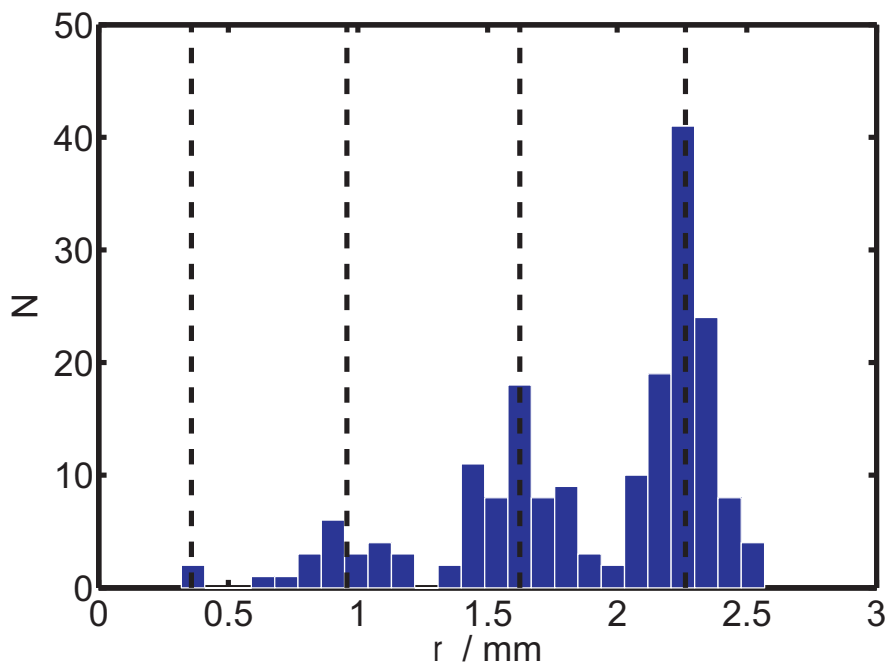


Figure 4.7: Radial particle distribution function of a Coulomb ball containing $N = 190$ particles.

dial positions, which are identified with the shell radii. By finding minima in the radial distribution the radial axis is partitioned into neighboring intervals, which define the spatial boundaries of each shell. Counting the number of particles lying within each of these radial intervals yields the *shell occupation numbers* N_S . For the present four shells ($S = 1 \dots 4$) the corresponding occupation numbers are $N_1 = 2$, $N_2 = 21$, $N_3 = 60$ and $N_4 = 107$. Obviously, these values are affected by an uncertainty of a few particles, since the separation of the shells is not unique due to particles located at inter-shell positions. More accurate quantities that can be derived from the radial distribution function are the shell radii r_S . These values are obtained by averaging the radial positions of all particles lying within the corresponding interval. Here, due to the averaging process the uncertainty of the shell boundaries does not yield large errors. The derived shell radii are $r_1 = 0.3$ mm, $r_2 = 0.89$ mm, $r_3 = 1.53$ mm and $r_4 = 2.18$ mm (indicated by the dashed vertical lines in Fig. 4.7.), which results in an average inter-shell distance $\delta_S = 0.63$ mm. Thus, compared with the inter-particle distance $b = 0.715$ mm obtained from the pair distribution function (see Fig. 4.4) the inter-shell distance is smaller by a factor $\delta_S/b = 0.87 \pm 0.06$.

According to Hasse *et al.* [43] the intra-shell structure directly affects the inter-shell distance δ_S . The authors presented a simple geometric model that considers two neighboring shells and assumes locally an ideal hcp structure, i.e. the hexagonal ordered inner and the outer shell are shifted by $b/2$. The model yields a ratio between the nearest neighbor distance b and the inter-shell distance δ_S of $\delta_S/b = 0.87$. The excellent agreement with the experimentally derived ratio yielding the same value is an additional indication of a hexagonal arrangement

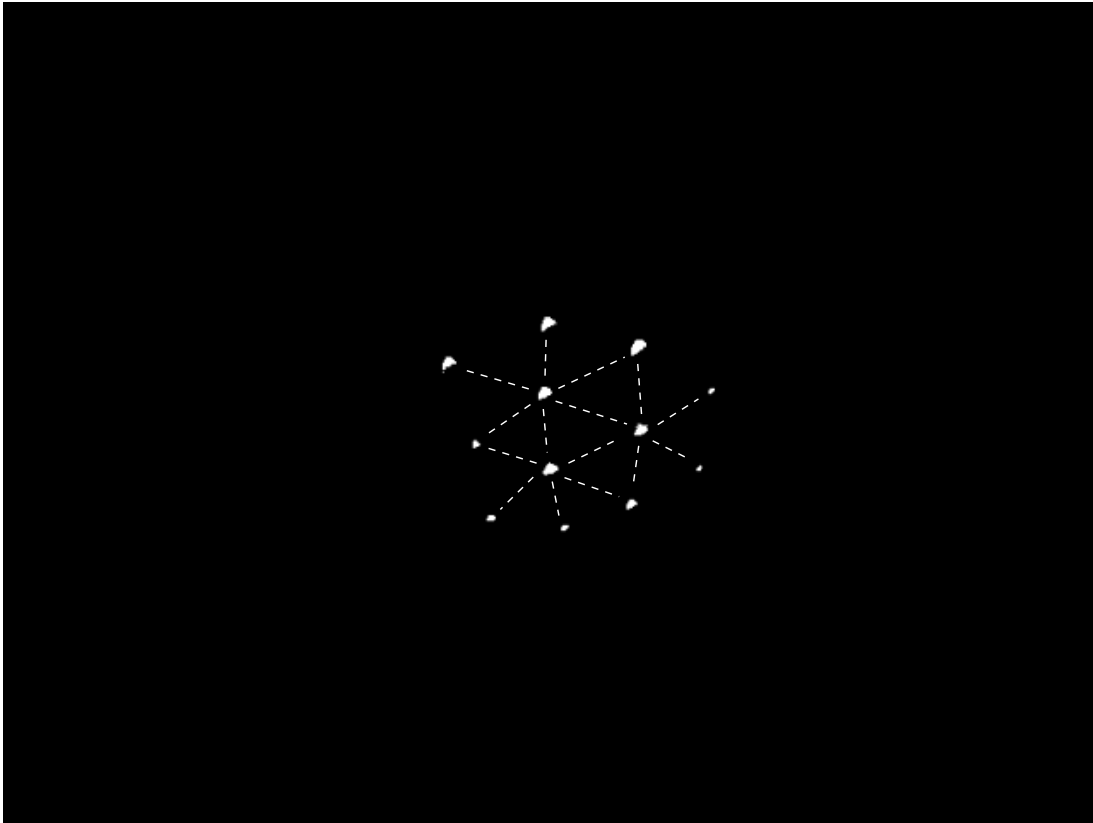


Figure 4.8: Laser sheet touching the surface of a Coulomb ball. The dashed lines indicate hexagonal order.

of the particles within a Coulomb ball.

4.4 Intrashell structure

Structural simulations of finite Coulomb clusters [34, 43, 87] found hexagonal order within the shells of finite Coulomb clusters. However, according to Euler's theorem as a consequence of the curvature of the spherical surface the hexagonal order is necessarily disturbed by defects. This results ideally in particle arrangements with five and six neighbors similar to the leather patches of a soccer ball. A first visual indication for the presence of such regular order within the shells of a Coulomb ball yields the experiment when positioning the laser sheet in a way that it touches the front or respectively the back side of the dust cloud. Thus, only particles of the outermost shell are visible (see Fig. 4.8). The figure shows that each of the three center particles are surrounded by six neighbors, which suggests a crystalline hexagonal order within this shell. To verify this suggestion the data of the reconstructed dust cloud is separated into the four shells by using the radial distribution function (see Fig. 4.7). Thus, it is possible to treat the particles pertaining to each shell separately. A broadly applied method to analyze the structure of crystals is the *Voronoi analysis* (e.g. [88–90]). In two

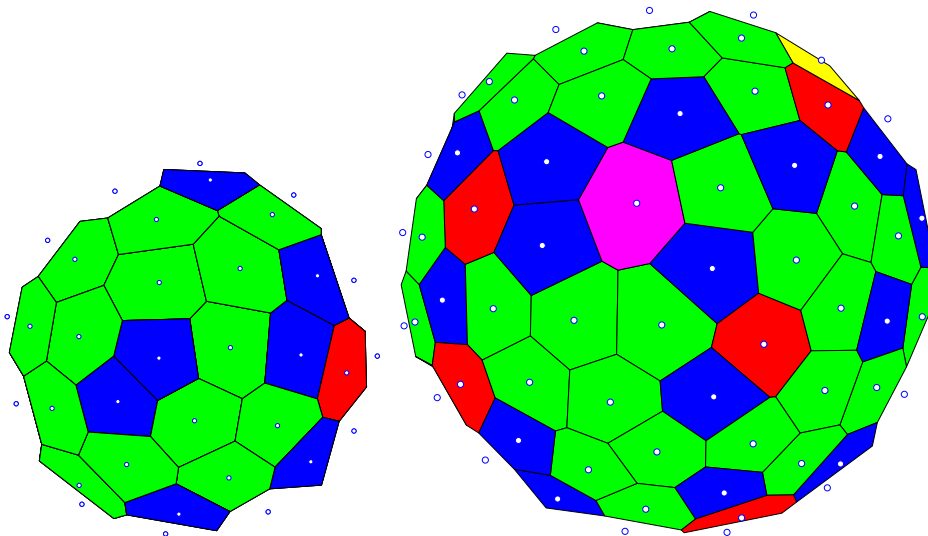


Figure 4.9: Voronoi analysis of approximately one hemisphere of the 3rd (left) and 4th (right) shell of a Coulomb ball containing $N = 190$ particles.

dimensions this method assigns a cell (*Voronoi or Wigner-Seitz cell*) to each particle, which is defined by a polygon surrounding the particle. The edges of this polygon are the rectangular bisectors of the connections between the considered particle and its neighbors. Thus, the number of edges of the resulting cell corresponds to the number of neighbors of the enclosed particle. As in the present case the particles are arranged on the surface of a sphere the curvature has to be taken into account when performing the Voronoi analysis in order to yield correct results [91–93]. The Voronoi analysis for the 3rd and 4th shell of the presented Coulomb ball is shown in Fig. 4.9. The figure shows almost one hemisphere of each shell. The white dots inside the cells mark the positions of the individual dust particles. One observes that the particles are evenly arranged in patterns with mainly five (dark gray) and six (light gray) neighbors. In the case of the 4th shell some defects with different numbers of neighbors are present. This finding is in excellent agreement with the structure proposed by the mentioned simulations and pronounces the similarity of Coulomb balls with other strongly coupled Coulomb systems, e.g. ion clusters.

4.5 Simulation of Coulomb balls

The presence of plasma results in shielded Coulomb, i.e. Yukawa interaction between the particles of a Coulomb ball. This kind of interaction suggests significant structural differences between Coulomb balls and pure Coulomb systems like ion clusters. Since it is experimentally not possible to vary the interaction between the dust particles in order to study its influence, simulations were performed. During this work there has been an intense collaboration with the *Institute of Theoretical Physics and Astrophysics (ITAP)* at the University of Kiel. Within

4.5. SIMULATION OF COULOMB BALLS

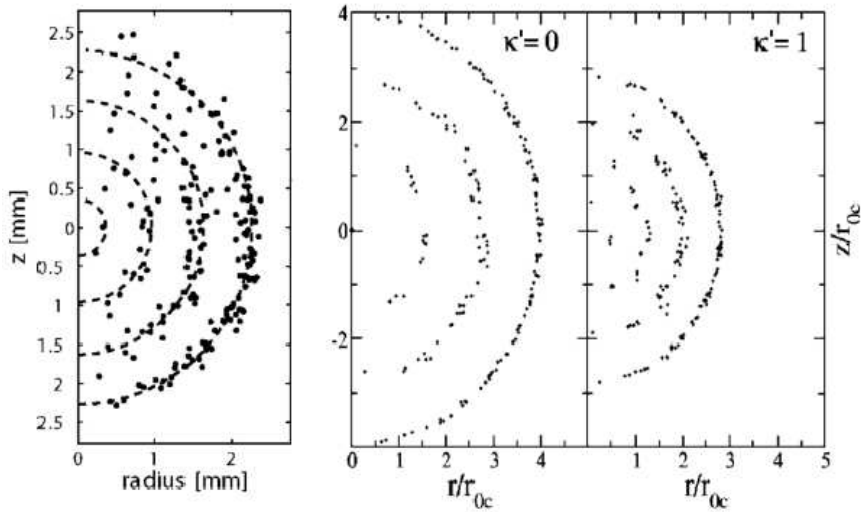


Figure 4.10: Comparison of experimental (left, identical with the cluster presented in Fig. 4.6) and simulated Coulomb balls containing each $N = 190$ particles. The MD-simulations are performed with Coulomb ($\kappa' = 0$) and Yukawa ($\kappa' = 1$) interaction. From Ref. [94].

this context Bonitz *et al.* [94] presented sophisticated simulations and calculations concerning the ground state configurations of Coulomb balls with Coulomb and Yukawa interaction. The results are summarized in the following.

A comparison of the previously discussed Coulomb ball containing $N = 190$ particles (see Fig. 4.6) and molecular dynamics (MD) simulations considering the same number of particles at Coulomb ($\kappa' = 0$) and Yukawa ($\kappa' = 1$) interaction is shown in Fig. 4.10. Deviating from the previous definition of the shielding strength (see Eq. (2.6)), in the simulations the shielding is described by $\kappa' = r_{0c}/\lambda_D$. Here, r_{0c} is the ground state distance of two Coulomb interacting particles inside a screening-independent harmonic potential well (see Ref. [94]). Both simulated Coulomb balls show four nested shells in agreement with the experiment. However, the separation of the shells is much clearer in the simulation compared to the experiment. Obviously, the presence of Yukawa interaction results in a smaller cluster radius compared to the Coulomb case. This can be considered a consequence of weaker interaction between the particles, which results in a smaller inter-particle distance.

A more complex analysis considering the individual shell radii of 43 experimental (symbols) Coulomb balls containing between $N = 100$ and $N = 500$ particles in comparison with MD-simulations (lines) is presented in Fig. 4.11. In the figure is R_S/a the shell radius in units of the average interparticle distance, corresponding to r_S/b in the here used notation. One observes an almost linear increase of the shell radii with $N^{1/3}$. Deviations are only observed at particle numbers N where new shells emerge. The simulations show a very good agreement with the measured data and almost no influence of the shielding strength

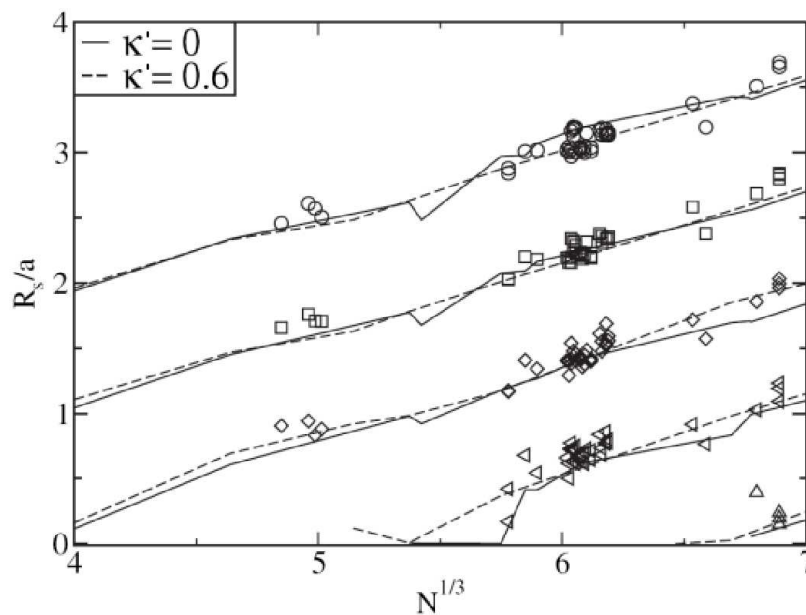


Figure 4.11: Shell radii in units of the inter-particle distance of 43 experimental (symbols) Coulomb balls and MD-simulations (lines). From Ref. [94].

Table 4.1: Experimental and simulated shell occupation numbers of a Coulomb ball containing $N = 190$ particles. The values are taken from Ref. [94].

$\kappa' \rightarrow$	0	0.2	0.3	0.4	0.5	0.6	1.0	Exp.
N_1	1	1	2	2	2	2	4	2
N_2	18	18	20	20	21	21	24	21
N_3	56	57	57	58	58	60	60	60
N_4	115	114	111	110	109	107	102	107

κ' on the shell radii in units of the inter-particle distance.

Besides the shell radii the influence of the shielding on the shell occupation numbers N_S are of interest. The corresponding values of the four shells of the experimental cluster $N = 190$ and simulations for different shielding strengths κ' are presented in Tab. 4.1. Obviously, in the presence of shielding, i.e. $\kappa' > 0$, more particles are located in the lower shells. Consequently, the occupation of the outermost shell N_4 is reduced compared to the Coulomb case ($\kappa' = 0$). At a shielding strength $\kappa' \approx 0.6$ the simulated shell occupation numbers agree exactly with the experiment. To verify whether this agreement is accidental, the shell occupation numbers of all mentioned 43 experimental clusters are analyzed and compared with simulations. The result is shown in Fig. 4.12. The symbols correspond to the experimental data, the lines to simulated clusters at different values κ' . With increasing cluster size N the number of particles within each shell

4.5. SIMULATION OF COULOMB BALLS

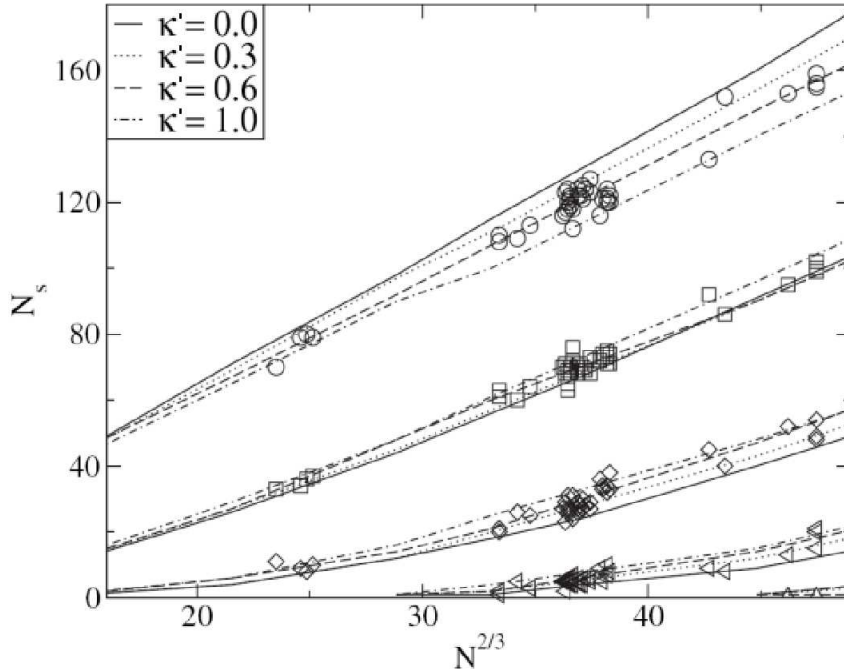


Figure 4.12: Experimental (symbols) and simulated shell occupation numbers N_S for different cluster sizes N . From Ref. [94].

N_S rises almost proportional to $N^{2/3}$. The exponent $2/3$ expresses the geometric relation between the surface of a sphere and its enclosed volume. Obviously, the configurations of the measured Coulomb balls deviate systematically from the simulated Coulomb systems ($\kappa' = 0$). In agreement with the already in Tab. 4.1 observed tendency the occupation numbers of the lower shells are in the experiment significantly larger than in the simulated Coulomb cluster ($\kappa' = 0$). Consequently, the outer-most shells are depleted. The simulations with Yukawa interaction show the same tendency of deviation from the Coulomb curves as the experimental data. Consistent with the previous finding, the simulations with a screening strength $\kappa' = 0.6$ show an excellent agreement with the experiment. According to Bonitz *et al.* the best fit to the experimental data yields a value of $\kappa' = 0.62 \pm 0.23$, which corresponds to a ratio $(b/\lambda_D)_{sim} \approx 0.65$ [94]. Using this value and $b/a_{ws} \approx 1.6$ from Sec. 4.2 one gets $\kappa_{sim} \approx 0.41$. In the 43 observed Coulomb balls the average inter-particle distance is $b \approx 0.6$ mm. Since the exact plasma conditions were not exactly known when observing the individual clusters an average shielding length $\lambda_D \approx 0.7$ mm is assumed, which is consistent with plasma simulations in Sec. 5.3.1. Again, with $b/a_{ws} \approx 1.6$ one gets $\kappa_{exp} \approx 0.54$, which is in reasonable agreement with the value obtained from the simulation.

To analyze the influence of a finite temperature on the shell radii and occupation numbers thermodynamic Monte Carlo (MC) simulations [94,95] were performed. These calculations show at typical temperatures and screening strengths only a weak effect on the shell roughness, but not on the shell radii and occupation

numbers.

In addition to the presented simulations focusing on the structural and thermodynamic properties of Coulomb balls calculations to estimate the real world dimensions and physical properties of the dust cloud in its real trap were performed. For this purpose an MD code by Piel [96] has been modified to fit the special needs. The code uses the algorithm of Verlet [97] to solve the following N Newton's equations of motion

$$m_d \frac{d^2 \vec{r}_i}{dt^2} = \vec{F}_{int}^{i,j} + \vec{F}_{conf}^i + \vec{F}_{fr}^i + \vec{F}_{rnd}^i, \quad (4.3)$$

where $i, j \in [1..N]$ and $j \neq i$ are the indices of two arbitrary particle at the positions $\vec{r}_{i,j}$. The Yukawa interaction force between the dust particles is given by

$$\vec{F}_{int}^{i,j} = -\frac{q_d^2}{4\pi\epsilon_0} \frac{\vec{r}_i - \vec{r}_j}{|\vec{r}_i - \vec{r}_j|^2} \left(\frac{1}{|\vec{r}_i - \vec{r}_j|} + \frac{1}{\lambda_D} \right) \exp\left(-\frac{|\vec{r}_i - \vec{r}_j|}{\lambda_D}\right), \quad (4.4)$$

where λ_D is the shielding length of the plasma. In the case of $\lambda_D \rightarrow \infty$ Eq. (4.4) reduces to pure Coulomb interaction. The second summand in Eq. (4.3) is the confining force \vec{F}_{conf}^i of the trap. Assuming an isotropic harmonic trap potential well the force is given by

$$\vec{F}_{conf}^i = -q_d \alpha \frac{\vec{r}_i}{|\vec{r}_i|}, \quad (4.5)$$

where the constant α expresses the strength of confinement. To allow the system to cool down and to approach a ground state the friction force

$$\vec{F}_{fr}^i = -\mu \frac{d\vec{r}_i}{dt}, \quad (4.6)$$

with the kinetic friction coefficient μ extracts kinetic energy from the system. However, to prevent the system from being trapped in metastable states and to simulate thermal motion, a random force $\vec{F}_{rnd}^i(T_d)$ is added. This force acts in each time step and on each particle in a different randomly distributed direction. Its absolute value is controlled by a Nosé-Hoover thermostat [98,99], which keeps the particles at a certain selectable temperature T_d . This code is used later in Sec. 5.4 to verify the proposed model of the trap, but shows even without a detailed knowledge of the actual trap potential interesting phenomena when simulating large Coulomb balls.

4.6 Large Coulomb balls

So far only Coulomb balls in a relatively limited range of particle numbers ($100 \leq N \leq 500$) are presented. However, the used trap allows also to confine Coulomb balls in a much wider range of particle numbers reaching from very few to many

4.6. LARGE COULOMB BALLS

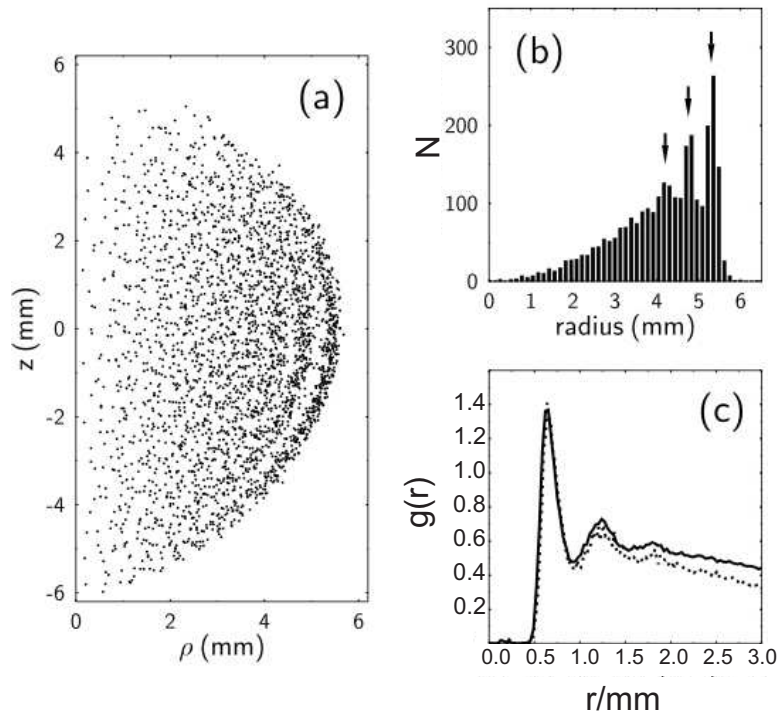


Figure 4.13: A large Coulomb ball containing approximately $N = 2800$ particles ($d = 3.47 \mu\text{m}$). (a) projection into the ρ - z plane (b) radial distribution function and (c) pair distribution function of the complete cluster (solid line) and the central $N/3$ particles (dotted line).

thousand particles. Experiments [77] and simulations [100] dealing with small clusters ($N < 100$) show that such systems are dominated by local order of the particles and do not show significant collective structure like the formation of shells. In the discussed range between approximately $N = 100$ – 400 the dominant structure is the shell structure with a hexagonal arrangement of the particle within the shells. Here, the particle number does not show any significant influence on the general structure of the cluster. This changes drastically when considering larger Coulomb balls. Here, a number of new structural phenomena are observed.

A large Coulomb ball containing $N \approx 2800$ particles ($d = 3.37 \mu\text{m}$) is shown in Fig. 4.13. In contrast to the previously presented much smaller Coulomb balls, only few shells in the outer region of the cloud are visible [see Fig. 4.13 (a)]. In the center region no pronounced shells are observable. Accordingly, the radial distribution function [see Fig. 4.13 (b)] allows to identify three outer shells (arrows) but no modulation is present at $\rho \lesssim 3$ mm. The pair distribution function $g(r)$ of the Coulomb ball is plotted in Fig. 4.13 (c) (solid line). It does not differ qualitatively from the curve of the smaller cluster (see Fig. 4.4). Even the function calculated only for the apparently structureless central $N/3$ particles (dotted line) does not show any significant difference except for a stronger decay with increasing r due to the smaller size of the subsystem. Thus, the particle

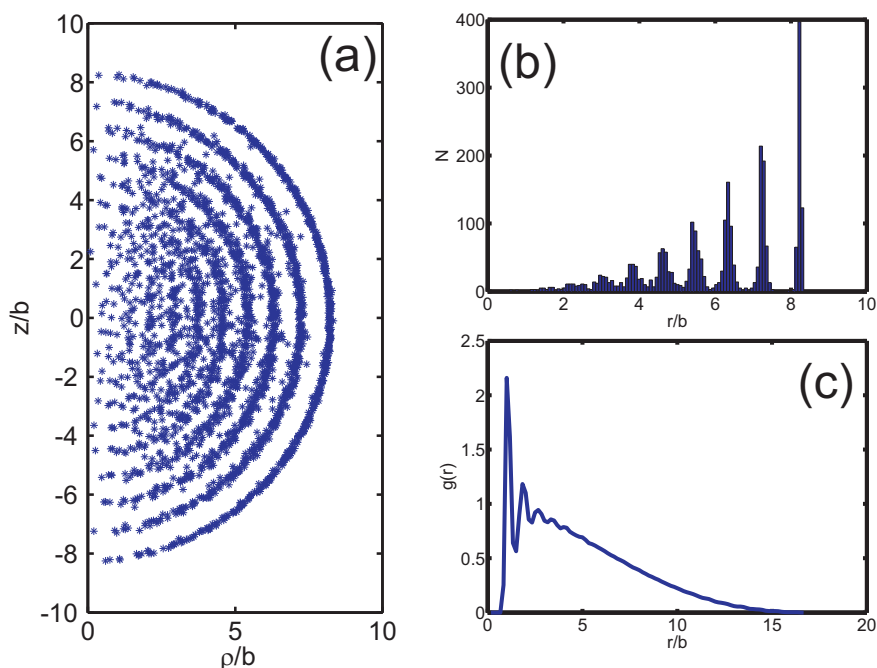


Figure 4.14: MD simulation of a large Coulomb ball with Yukawa interaction at a Debye length $\lambda_D = 0.5$ mm and a dust temperature $T_d = 300$ K. (a) projection into the ρ - z plane (b) radial distribution function and (c) pair distribution function of the complete cluster.

correlation in the center and the outer region of this large cluster is practically identical although significant differences in the structure are observable.

For comparison, in Fig. 4.14 a simulated Yukawa cluster ($\lambda_D = 0.5$ mm, $T_d = 300$ K) containing $N = 2800$ particles is shown in Fig. 4.14. Similar to the experiment the shell structure is not expanded into the center of the cluster. Only in the outer regions distinct shells are observable. When approaching the center more and more particles are at inter-shell positions until no shell structure is visible in the central region. This finding is again in good agreement with observations of large ion clusters ($N \approx 10^6$) in Penning traps [46] and consistent with simulations [34, 48]. However, with the present diagnostic, it was not possible to detect any crystalline bulk order in the central region of large Coulomb balls. Better suited methods might yield a different result. Since the plasma conditions during the observation of the cluster presented in Fig. 4.13 are not precisely known, the simulation assumes a trap potential that is derived in Chapt. 5 for slightly different plasma conditions. Consequently, the absolute cluster dimensions in the simulation are arbitrary. To allow for a quantitative comparison the dimensions are given in units of the inter-particle distance b . In the experiment this quantity is obtained from the pair distribution function [see Fig. 4.13 (c)] yielding $b \approx 0.63$ mm. Using this value to calculate the real world dimensions of the simulated cluster results in a cluster radius $r_{sim} \approx 8.4b \approx 5.2$ mm, which is

4.6. LARGE COULOMB BALLS

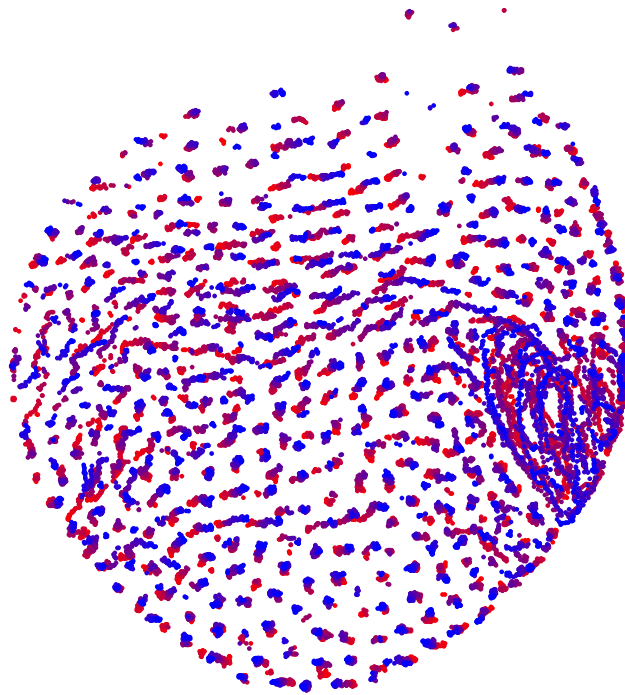


Figure 4.15: Superposition of 120 vertical sections through the center of a huge Coulomb ball containing more than 6000 particles ($d = 3.47 \mu\text{m}$). The sections are recorded over a duration of 120 s. The time is color-coded, i.e. a moving particle is indicated by a trace from red to blue.

in good agreement with the observation [see Fig. 4.13 (a)].

Within the presented trap even larger dust clouds can be confined. A vertical section through the center of a huge dust cloud with a diameter of 15 mm containing $N > 6000$ particles is shown in Fig. 4.15. To illustrate the motion of the dust particles the figure is generated by superimposing 120 sections that were imaged in 1 s intervals. The time is color coded, i.e. a moving particle produces a trace that begins in red and ends in blue. Except for a separation of the outermost particle layer no pronounced shell structure is visible. The figure illustrates the coexistence of crystalline domains in the bottom part with almost no particles motion and liquid domains with mostly moderate motion inside the dust cloud. Near the "equator" at the right hand side even fast moving particles yielding a vortex structure are visible. Due to the limited extension of this structure and the low gas pressure, convection and gas flow drop out as reason for this phenomenon. Similar to Sec. 3.2.2 a possible driving mechanism for the observed motion is an inhomogeneous plasma, which causes a spatially varying dust charge in the observed cloud.

To get a deeper and quantitative understanding of the observed structural and dynamical effects observed in Coulomb balls a detailed knowledge of the mechanism of the trap is essential and is addressed in the next chapter.

5 Confinement of Coulomb balls

In the previous chapter a variety of structural properties of Coulomb balls were attributed to the properties of the confining trap. To allow for a more quantitative analysis of the observed phenomena, like the dependence of the shell occupation numbers and cluster radii on the type of interaction, a detailed knowledge of the plasma parameters inside the trap is essential. In addition, quantitative MD simulations of Coulomb balls, require the knowledge of the real trap potential, which can only be derived with a fundamental understanding of the trap. Based on simple experiments a set of major forces that contribute to the confinement is identified. A basic model of the trap based on these forces is derived and verified by a combination of measurements and simulations. Finally, the modeled properties of the trap are compared with the experimental observations.

5.1 Basic principle of the trap

For the understanding of the mechanism that confines Coulomb balls the careful observation of the behavior of the dust particles inside the glass box plays an important role. Already in Chapt. 3 a number of phenomena were described. In addition to these experiments a more detailed analysis of the dependence on the electrode temperature and the rf amplitude yield a basic model of the trap.

In Fig. 5.1 three vertical sections of the same Coulomb ball are shown at different electrode temperatures T_E . Here, dust particles with a diameter $d = 4.8 \mu\text{m}$ are used. The origin of the vertical axis is located at the surface of the electrode. The shape of the confined dust cloud varies from prolate at $T_E = 65 \text{ }^\circ\text{C}$ via circular at $T_E = 75 \text{ }^\circ\text{C}$ to oblate at $T_E = 85 \text{ }^\circ\text{C}$. Even slight variations of the electrode temperature result in surprisingly direct reactions of the dust cloud within fractions of a second. These findings show that the thermophoretic force plays a crucial role for the confinement and that it is necessary to properly adjust the electrode temperature to obtain spherical Coulomb balls. In addition to the variation of the shape, the vertical position of the confined dust cloud increases with the electrode temperature. From the fact that the shape of the cloud varies it can be concluded that the temperature gradient $\vec{\nabla}T$ and (due to its proportionality, see Sec. 5.2) the thermophoretic force is not constant but varies with height inside the glass box. Otherwise, only an influence on the position of the cloud but not on its shape is expected.

A second experiment that plays a key role for the understanding of the mech-

5.1. BASIC PRINCIPLE OF THE TRAP

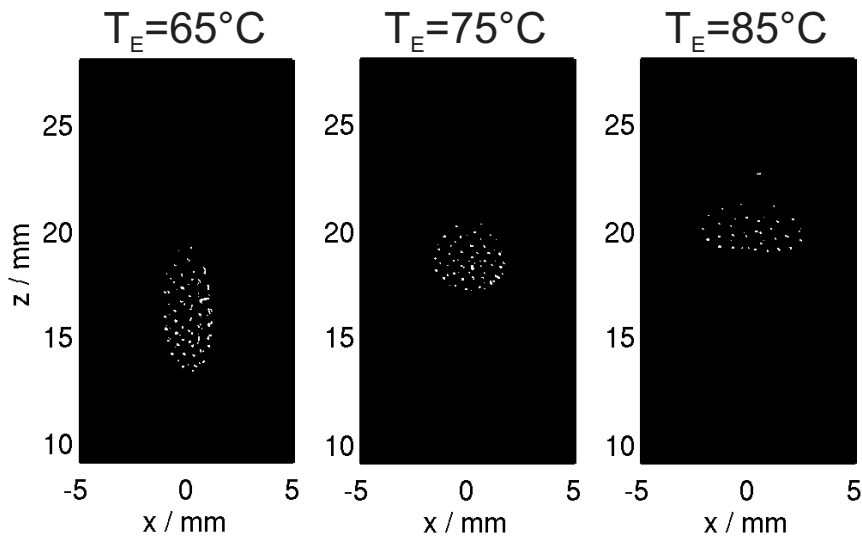


Figure 5.1: Vertical sections through the center of a dust cloud at different electrode temperatures T_E .

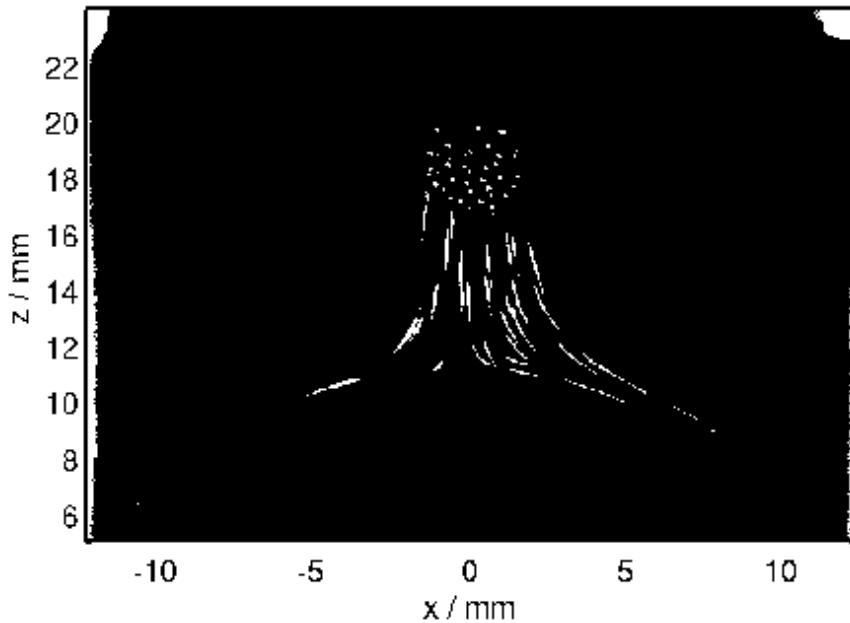


Figure 5.2: Superposition of multiple video frames. The motion of the dust particles results in white traces. Switching the plasma off leads an initially confined spherical Coulomb ball ($x = 0$ mm, $z \approx 19$ mm) to fall down until the particles are deflected towards the outer region of the glass box at $z \approx 11$ mm.

5. CONFINEMENT OF COULOMB BALLS

anism of confinement is shown in Fig. 5.2. Again, in this figure, $z = 0$ mm corresponds to the surface of the electrode. The white structures at the left and right edges of the image are light reflections from the glass walls. The image is a superposition of a number of subsequent video frames. At the beginning of the experiment a spherical Coulomb ball ($d_c = 4.8 \mu\text{m}$, $d_{CB} \approx 3.2$ mm, $N \approx 200$, $a_{ws} \approx 0.3$ mm) is confined, which is located at the position ($x = 0$ mm, $z \approx 19$ mm). Then, the rf is abruptly switched off. This causes the dust particles to fall down and produces white traces in the image between $z \approx 17$ mm and $z \approx 11$ mm. The trajectories of the particles are directed almost straight downwards to the electrode with only a slight divergence. When the particles reach a height of $z \approx 11$ mm they are significantly deflected towards the walls of the glass box. Since the time scale for the plasma decay after switching the rf off (microseconds) is much shorter than the time scale for the motion of the particles (milliseconds), the particles can be considered electrically neutral on their way down towards the electrode. Thus, the deflection of the particles can only be caused by non-electric forces most probably due to the thermophoretic force as a consequence of the heated electrode.

From these observations a number of conclusions can be drawn. First, a significant fraction of the downward-directed gravitational force is compensated by an upward-directed thermophoretic force. Otherwise a slight increase of temperature could not have such a significant effect on the levitation height. Second, the trajectories of the falling particles after switching the plasma off show that the thermophoretic force obviously increases when approaching the electrode. Thus, the temperature gradient inside the glass box is not constant. Third, the fact that the deflection takes place at a much lower position than the levitation height of the Coulomb ball, shows that it resides at a position, where gravity is not completely compensated by thermophoretic force. Finally, the thermophoretic force does not provide a radial confinement. Hence, the compensation of the residual fraction of gravity as well as the radial confinement of the dust has to be established by plasma-induced forces. The observed influence of the rf voltage on the shape and location of a trapped Coulomb ball (see Sec. 3.2.2) supports this picture.

To summarize, the observations suggest a basic principle of the particle trap as sketched in Fig. 5.3. Each particle inside the glass box is affected by the gravitational force \vec{F}_g . As a consequence of the vertical variation of the temperature gradient inside the glass box, the upward-directed thermophoretic force \vec{F}_{th} increases when a particle approaches the electrode. In the lower part of the trap, the thermophoretic force is sufficiently large to compensate gravity, which prevents the particles from reaching the electrode in the center region of the glass box. Due to surface charges on the glass walls and electric fields inside the trap the negatively charged dust particles are repelled from the glass walls and the electrode towards the bulk plasma above the glass box. The vertical component of the electric field force $F_{E,z}$ is directed upwards, thus it supports the thermophoretic force in compensating gravity. Because of a steady flow of electrons and ions from the bulk plasma onto the glass walls and onto the electrode, a

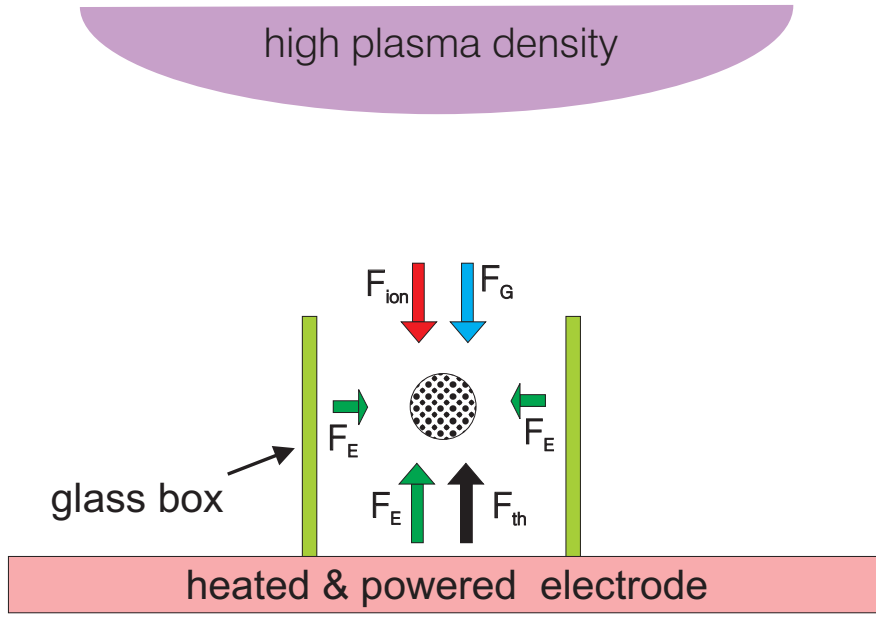


Figure 5.3: Basic principle of the trap: The vertical confinement of a Coulomb ball is established by upwards-directed thermophoretic \vec{F}_{th} and electric force \vec{F}_E , which compensate for the downwards directed gravitational \vec{F}_g and ion-drag force \vec{F}_{ion} . The lateral confinement is attributed to the electric force \vec{F}_E .

mainly downward-directed ion-drag force is expected.

As the forces that contribute to the confinement are identified, the strategy for verifying the proposed mechanism of confinement is as follows: In a hierarchic approach, beginning with the strongest, the forces are determined and analyzed with respect to their contribution to the confinement of Coulomb balls. The strongest forces are gravity and the thermophoretic force. Since the gravitational force is defined by the known properties of the dust particles only the thermophoretic force field inside the glass box has to be measured. Afterwards, the plasma-induced forces, i.e. the electric field force and the ion-drag force, are derived from a simulation of the discharge including the glass box. By superimposing all these forces the trap is modeled.

5.2 The thermophoretic force

Small macroscopic particles suspended in a fluid, under influence of a temperature gradient, move against the gradient towards colder regions [65]. This phenomenon is called thermophoresis and is described by the thermophoretic force \vec{F}_{th} . In the microscopic view the reason for this force can be regarded as follows: The presence of the temperature gradient results in a modified non-isotropic velocity distribution function of the gas molecules (e.g. Ref. [101,102]). Accordingly, there are less fast and therefore more slower gas molecules moving in the direction of

the temperature gradient compared to the opposite direction. Consequently, the average momentum transfer by impacts of gas molecules at the side of a dust particle directed towards the region of higher gas temperature is larger than on the other side. Hence, a force acts on the particle, which is directed opposite to the temperature gradient and accelerates it towards regions of colder neutral gas.

The relevance of this effect for experiments dealing with complex plasmas has been shown by Jellum *et al.* [103]. The presence of a temperature gradient inside the neutral gas affects the arrangement of dust particles confined in a plasma. An application of the thermophoretic force within the context of complex plasmas was presented by Rothermel *et al.* [27]. The authors showed that it is possible to use an externally applied temperature gradient in the gas background of a complex plasma to compensate for gravity.

An analytical model of the thermophoretic force acting on a spherical dust particle was given by Talbot *et al.* [104]. Assuming a thermally accommodated particle, which is expected in the present case, the force is given by the expression

$$\vec{F}_{th} = -\frac{32}{15} \frac{r_d^2}{\bar{v}_{tn}} \Lambda \vec{\nabla} T_n \quad (5.1)$$

Here is $r_p = d/2$ the radius of a dust particle, Λ the heat conductivity of the neutral gas (translational component in the case of a non-atomic gases), and

$$\bar{v}_{tn} = \sqrt{\frac{8k_B T_n}{\pi m_n}} \quad (5.2)$$

the mean thermal velocity of the neutrals. The temperature of the neutral gas is T_n and the mass of a gas molecule m_n , which in the case of atomic argon is $m_n = 40$ amu. The heat conductivity depends on the gas temperature and is given by

$$\Lambda = \alpha c \eta, \quad (5.3)$$

with the specific heat capacity $c = (3k_B)/(2m_n)$ and η the viscosity of the neutral gas [105]. The factor $\alpha \approx 2.5$ applies to the case of an atomic gas [106]. Finally, with the expression

$$\eta = \frac{5\sqrt{\pi}}{16} \frac{\sqrt{m_n k_B T_n}}{\sigma_n}, \quad (5.4)$$

which is derived from a hard sphere collision model [105], the thermophoretic force is

$$\vec{F}_{th} = -\beta k_B \frac{r_d^2}{\sigma_n} \vec{\nabla} T_n. \quad (5.5)$$

Here $\beta = \alpha\pi/\sqrt{8} \approx 2.78$ and $\sigma_n = 4.2 \times 10^{-19} \text{ m}^2$ denotes the cross-section for neutral-neutral collisions [107]. According to Eq. (5.5) the thermophoretic force is independent of the absolute gas temperature and pressure. However, at the

5.2. THE THERMOPHORETIC FORCE

used gas pressure of $p = 50$ Pa it is questionable whether Eq. (5.3) and Eq. (5.4) are highly reliable since the mean free path of neutrals $\ell_n = k_B T_n / (p \sigma_n)$ is much larger than the dimension of the dust particles, i.e. the concept of viscosity loses its meaning [105]. Hence, it should be kept in mind, that the accuracy of Eq. (5.5) is limited. In addition, there are other expressions describing the thermophoretic force, e.g. [27,108,109], that in part differ significantly from Eq. (5.1) [respectively Eq. (5.5)]. Transforming the given expressions for \vec{F}_{th} into the form of Eq. (5.5) yields a range for the value of β as $2.66 \lesssim \beta \lesssim 5.66$. Consequently, the here derived value of β must be considered a first approximation. For precise calculations of the thermophoretic force β has to be determined experimentally.

Rothermel *et al.* [27] presented an expression for the thermophoretic force that equals Eq. (5.5) when setting $\beta = 3.33$, i.e. their force is by ≈ 20 % larger with respect to the derived value here. The authors compared the theoretically derived force with experimental data and found a good agreement. As the setup and the discharge conditions of their experiment are very similar to the present case the value $\beta = 3.33$ was taken to determine the thermophoretic force within the context of this work.

In addition to the problem of choosing the correct β , Havnes *et al.* [108] found that the component of the thermophoretic force pointing towards a colder wall is significantly reduced, up to one half of its initial value, when approaching this wall. This effect becomes important when the distance x of the particle from the wall is below $\approx 5\ell_n$. In the present case ($p = 50$ Pa and $T_n \approx 300$ K) is $\ell_n \approx 0.2$ mm, i.e. the thermophoretic force is only influenced up to a distance of ≈ 1 mm from a wall. Thus, it is not expected that this effect influences the thermophoretic force in the focused central region of the glass box, which has a width of ≈ 30 mm.

As first application of Eq. (5.5) it is now possible to derive the temperature gradient at the positions where the thermophoretic force compensates for gravity in Fig. 5.2. With the Earth acceleration $g = 9.81$ m/s² the gravitational force acting on a dust particle of a Coulomb ball is given by

$$F_{g,c} = -\frac{4}{3}\pi g \varrho_d \left(\frac{d_c}{2}\right)^3 \approx 8.6 \times 10^{-13} \text{ N} . \quad (5.6)$$

Equating this value with the thermophoretic force in Eq. (5.5) yields the vertical component of the temperature gradient $\partial T / \partial z \approx 1356$ K/m, which is necessary to levitate a dust particle with a diameter $d_c = 4.8$ μm . Assuming, for comparison, a linearly decreasing temperature when approaching the lid of the chamber, i.e. a constant temperature gradient in the chamber, the temperature difference $\Delta T \approx 46$ K between the electrode and the lid of the chamber yield a value of $\Delta T / \Delta z \approx 460$ K/m. This significant discrepancy between this value and the temperature gradient that is necessary to levitate the particle is a further indication for the previously proposed vertical variation of the temperature gradient, which makes a measurement of the thermophoretic force essential.

To measure the thermophoretic force $\vec{F}_{th,c}$ acting on a dust particle of a Coulomb ball it is necessary to introduce an additional kind of diagnostic. The

basic idea behind the intended measurement is to inject heavier dust particles, so-called tracer particles, into the glass box when the electrode is heated but no plasma is present. Neglecting any flow of the neutral gas the injected tracer particles are considered to be only subject to gravity and thermophoretic force. Thus, by analyzing the trajectories of the tracer particles it is possible to derive the thermophoretic force $\vec{F}_{th,t}$. The reason for choosing heavier particles is to overcome the thermophoretic force even in the lower parts of the glass box, from which the smaller particles are expelled (see Fig. 5.2). By choosing tracer particles with a diameter $d_t = 9.55$, it is possible to reach most parts of the glass box. This is necessary to obtain the thermophoretic force field in the complete field of view. Inspecting Eq. (5.5), the thermophoretic force depends on the size of the particles. Thus, the force $\vec{F}_{th,t}$ acting on the tracer particles differs from $\vec{F}_{th,c}$, which acts on the smaller particles of a Coulomb ball. Using Eq. (5.5) and introducing d_t and d_c , for the diameters of the tracer particles and for those forming the Coulomb ball, yields the relation

$$\vec{F}_{th,c} = (d_c/d_t)^2 \vec{F}_{th,t} . \quad (5.7)$$

Accordingly, $\vec{F}_{th,t}$ and $\vec{F}_{th,c}$ are simply scaled by the ratio of the particle diameters squared.

5.2.1 Particle image velocimetry (PIV)

As stated above, the measurement of the thermophoretic force inside the glass box is based on the analysis of the trajectories of injected tracer particles. The diagnostic method applied here is called *Particle Image Velocimetry (PIV)*. It is an optical method to determine a two- or three-dimensional velocity field of tracer particles embedded in a fluid. These particles are assumed to follow a well-known (fluid dynamic) equation of motion, which is typically used to derive the dynamics of the surrounding fluid. The basic principle of measurement is as follows: The positions of the tracer particles within a selected volume of the fluid is instantaneously measured. Then this measurement is repeated after a well defined short period of time. By analyzing the displacements of the particles between both measurements, their velocities are derived. The most challenging part of the PIV method is to acquire instantaneously the positions of all tracer particles in the desired volume. Since it is very sophisticated to do this in three dimensions, most applications are restricted to a two-dimensional velocity field containing the two components of velocity lying within a thin slice of the measurement volume. In order to get these data, typically a thin laser sheet illuminates a section of the fluid. The light scattered by the tracer particles is recorded twice by a CCD camera with a short delay between the two images. Analysing the images yields the positions of the illuminated tracer particles. Since the motion of the particles can be very fast, two things have to be considered. First, it is necessary to use short exposure times to get sharp images of the moving particles and thus precise position data. Second, the delay between both measurements

5.2. THE THERMOPHORETIC FORCE

has to be chosen sufficiently short to ensure that the displacement of the particles is less than one-half of the minimal inter-particle spacing. Otherwise a meaningful analysis of the data is not possible. For applications where a two-dimensional velocity field is not sufficient there are numerous modifications of the described technique. The so-called *stereoscopic PIV* method uses two cameras to image the particles within a thin laser sheet under two different angles. By using this setup in combination with a more sophisticated image analysis it is possible to obtain the third velocity component of the particles perpendicular to the almost two-dimensional laser sheet. This method has recently been applied to observe transport phenomena in complex plasmas [110]. A complete three-dimensional velocity field containing three velocity and space components is gained by using holographic approaches (*holographic PIV*) [111]. A wide range of applications in science and industry [112] uses this technique in order to measure the motion of a fluid. There is in addition to the mentioned basic PIV principles a large number of implementations, also commercially available, that vary the basic principles in order to fit special needs. With respect to its application on complex plasmas [110,113] this method can be considered mostly non-invasive since the tracer particles are naturally present and typically the particles themselves are the object of observation rather than the surrounding plasma. Nevertheless, it has to be taken into consideration that the laser illumination might have an effect on the complex plasma by its radiation pressure [114] or by photophoretic forces [115].

Within the context of this work, an implementation of the two-dimensional PIV method (two space and two velocity components) has been applied to measure a thermophoretic force field acting on dust particles. In order to achieve this goal, a two-dimensional velocity field of tracer particles that fall through the thermophoretic force field inside the glass box is measured. To ensure that the motion of the tracer particles is (besides the thermophoretic force) only subject to known forces the plasma remains switched off during these measurements. Thus, the tracer particles are only affected by gravity, which is a known quantity, and by the thermophoretic force. To obtain the velocity data in the complete field of view, a spatially extended dust shower of these particles has to be produced. To prevent that a large number of injected particles induces a flow of the neutral gas, the flux of dust particles is kept a low value. By using an equation of motion, which includes neutral drag, thermophoresis, gravity and the inertia of the particles, it is possible to derive the thermophoretic force acting on the tracer particles. In contrast to previous applications in complex plasmas (e.g. [110,113]), here, the tracer particles are not part of the complex plasma but are additionally injected in the absence of a plasma. As the thermophoretic force depends on the size of the particles it is necessary to apply a correction according to Eq. (5.7) in order to obtain the correct value for the smaller particles that are used for the Coulomb balls.

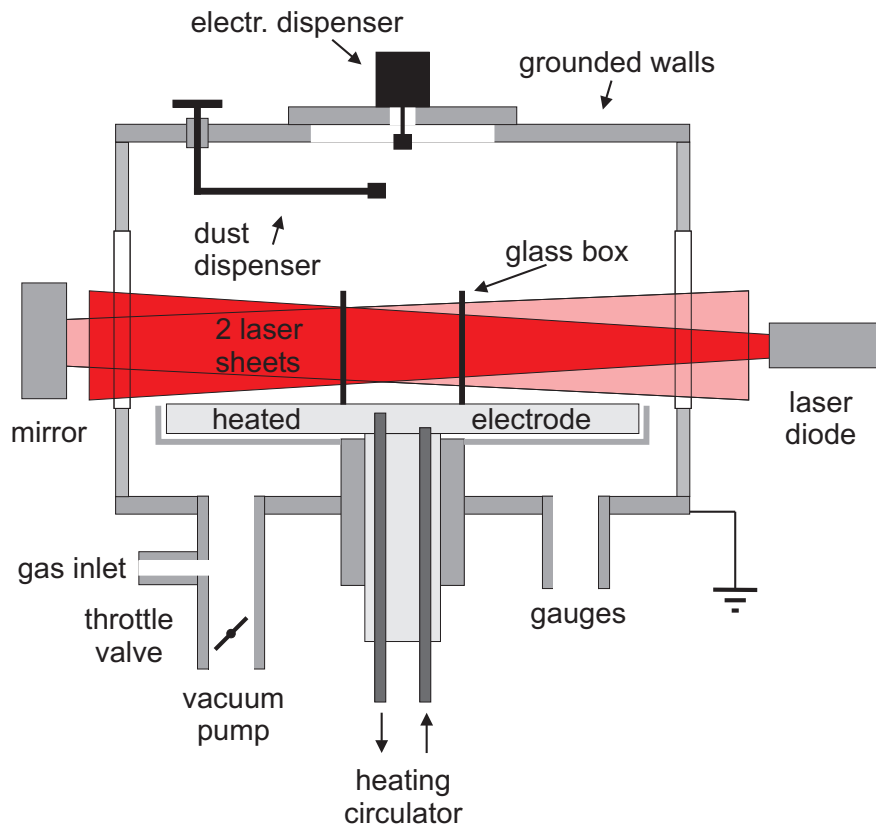


Figure 5.4: A vertical section through the modified discharge chamber. An electro-magnetic dispenser has been installed in the center of the lid.

5.2.2 Setup

Since the manual dispenser is not suited to produce the desired homogenous dust shower above the glass box a second electro-magnetic dispenser is installed. A sketch of the modified setup is shown in Fig. 5.4. The window in the lid of the chamber is replaced by a metallic disc with the new dispenser at its center. To prevent a possible influence of the newly installed metallic surface on the discharge the vacuum-facing surface of the disc is covered by a sheet of PTFE in order to simulate the dielectric window. The newly installed dispenser consists of an electro-magnetically shaken dust container with a sieve at its bottom (similar to a salt shaker). By applying periodic voltage pulses to the coil of the magnet the dust container moves up and down, which generates an almost homogenous dust shower. In a certain range of the pulse width and period the rate of injected particles can be adjusted. The sieve of the dispenser has a much larger influence on the properties of the produced dust shower and must be selected carefully. Electro-formed sieve material [116] has been used, which has square holes with a side length between $8 \mu\text{m}$ and $25 \mu\text{m}$. The actually chosen mesh size is a tradeoff between the number of injected dust particles and the clogging rate of the sieve. As a rule of thumb, the mesh size has to be about three times the

5.2. THE THERMOPHORETIC FORCE

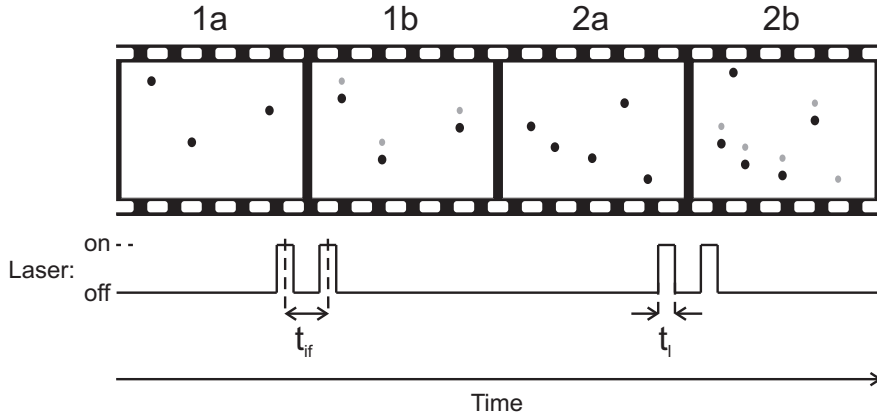


Figure 5.5: Timing scheme illustrates the coaction of camera exposures and pulsed laser illumination as used for the PIV measurements.

particle diameter to guarantee a satisfactory function of the device. As described for the manual dispenser, the new dispenser was filled with a mixture of dust and steel balls to reduce the clogging rate of the sieve by dust agglomerates. Although the sieve material has only an optical transparency of 10%, for most applications here, where only a very dilute dust shower is desired, the throughput of dust particles is still too large. Hence, an aperture is installed in front of the sieve to reduce the total sieve area and thus the flux of injected particles.

For the PIV measurements the existing SVM setup (see Sec. 4.1) has been used. Unfortunately, the maximum frame rate (40 fps) of the CCD camera does not allow for the necessary short delay between two successive exposures. As a workaround a pulsed laser illumination synchronized with the exposure of the camera yields the necessary improvement. This technique utilizes the property of the used camera, that in a certain mode of operation, two successive exposures are separated by only a very short delay of a few microseconds. The timing scheme in Fig. 5.5 illustrates the co-operation of the pulsed laser illumination and the camera. The camera is operated at 40 fps and at the maximum possible exposure time of almost 25 ms. The synchronization of the pulsed laser illumination and the camera exposure is done as follows: The first laser pulse occurs near the end of the exposure time of the first video frame (1a). After a time t_{if} a second laser pulse is triggered. The delay is chosen in a way that the second laser pulse appears at the beginning of the exposure of the following video frame (1b). Then for a relatively long period of time nothing happens until, at the end of the following video frame (2a), the next laser pulse occurs and the procedure repeats. This timing scheme ensures, on the one hand, that each video frame is illuminated only once and, on the other hand, it yields pairs of successive video frames (1a/b, 2a/b, ...) with a well-known and very short delay between both exposures. In the present case typical values for t_{if} are in the range of $t_{if} = (1-2.5)$ ms at a width $t_L = 1$ ms of the laser pulse. Thus, the illumination time is short enough to acquire sharp images of the moving particles, and the effective time resolution

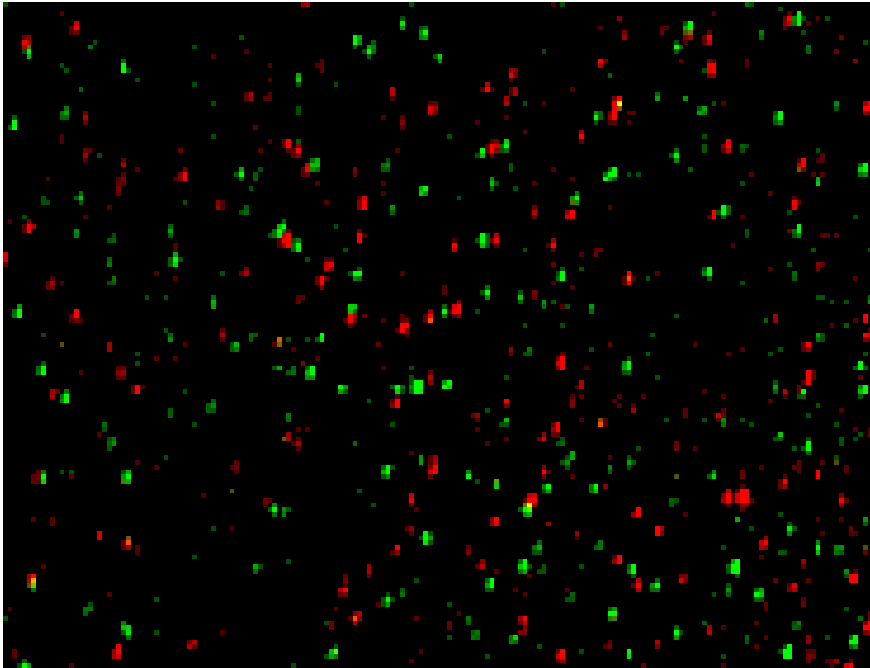


Figure 5.6: Partial view of a superposition of a pair of PIV images. The red channel of this color image corresponds to the first and the green channel to the second PIV image.

is improved by up to a factor of 25 with respect to the regular frame rate of the camera.

5.2.3 Analysis of PIV data

A superposition of a pair of PIV images is shown in Fig. 5.6. The first image corresponds to the red and the second image to the green channel of the displayed color image. Each colored spot is a dust particle in the first and respectively the second PIV image. By careful inspection of the image one observes a mainly vertical motion of the particles with a slight tendency to the left hand side. Due to the short exposure time the images of the single particles are sharp and not blurred by motion.

Two different approaches are common to analyze the PIV images in order to derive the velocity vectors of the particles. The *particle tracking* method uses, in a first step, a particle detection algorithm, which yields the positions of the dust particles in both frames. In a second step, it tries to identify each individual particle of the first frame in the second. By measuring the displacement of each particle the velocity vectors are estimated. The resulting data is then interpolated to a rectangular grid to get a useful velocity field. It is obvious that this approach becomes very complicated and susceptible for errors when the particle density inside the images is high. A more robust and, for most applications, better

5.2. THE THERMOPHORETIC FORCE

suitable technique is the use of a so-called *block-matching* algorithm. This approach does not estimate the velocity vector of each single particle, but uses statistical methods to yield an average displacement vector of selected regions of the first frame. For this purpose it is divided by a square grid into a number of so-called *interrogation areas* with a typical side lengths of 32 or 64 pixels. By cross-correlation each interrogation area is matched within a larger *search area* to the second frame in order to obtain a displacement vector. Since this displacement vector represents the average displacement of the interrogation area this method is much more robust with respect to high particle densities in comparison to the particle tracking method. In addition the resulting vector field fits naturally to a square grid. This motion estimation by using the block-matching technique is widely used in computer science, e.g. for the compression of digital video material.

A freely available toolbox for *MATLAB* [117] called *MatPIV* [118] implements the described method and has been used within the scope of this work. In addition, this package includes a set of filters to enhance the quality of the obtained velocity field. The requirement of the block-matching algorithm for a certain minimum value of particle density in the images contradicts the desire for a dilute dust shower. Therefore, the analysis is not applied to the original PIV images but to superpositions of a number of a-frames and b-frames, respectively. By this means it is possible to adjust the necessary particle density inside the images after the actual measurement. Since the resulting velocity fields are the basis for various calculations their quality, especially their smoothness, is very crucial. It turned out to be favorable to perform an additional average over multiple velocity fields gained by the described method.

5.2.4 Neutral friction

All objects that move inside a gas atmosphere are subject to a friction force as a consequence of collisions with neutral gas molecules. In the present case of spherical tracer particles this neutral friction force is, according to Epstein [119], given by

$$\vec{F}_{fr} = -\delta \frac{4}{3} \pi r_d^2 m_d n_n \bar{v}_{tn} \vec{v}_d, \quad (5.8)$$

where n_n is the number density of the neutral gas and \vec{v}_d the velocity of the dust particle relative to the neutral gas. The Millikan coefficient δ expresses the type of reflection of a gas molecule after it hits a dust particle. Its value lies in a range defined by the cases of pure specular reflection ($\delta = 1$) and pure diffusive reflection ($\delta = 1 + 4/9$) [119]. Assuming an ideal gas, i.e. $n_n = p/(k_B T_n)$, and with $m_d = 4/3 \pi \rho_d r_d^3$ Eq. (5.8) transforms to

$$\vec{F}_{fr} = -m_d \beta_{fr} \vec{v}_d \quad (5.9)$$

with the Epstein coefficient

$$\beta_{fr} = \delta \frac{8}{\pi} \frac{p}{\rho_d r_d \bar{v}_{tn}}. \quad (5.10)$$

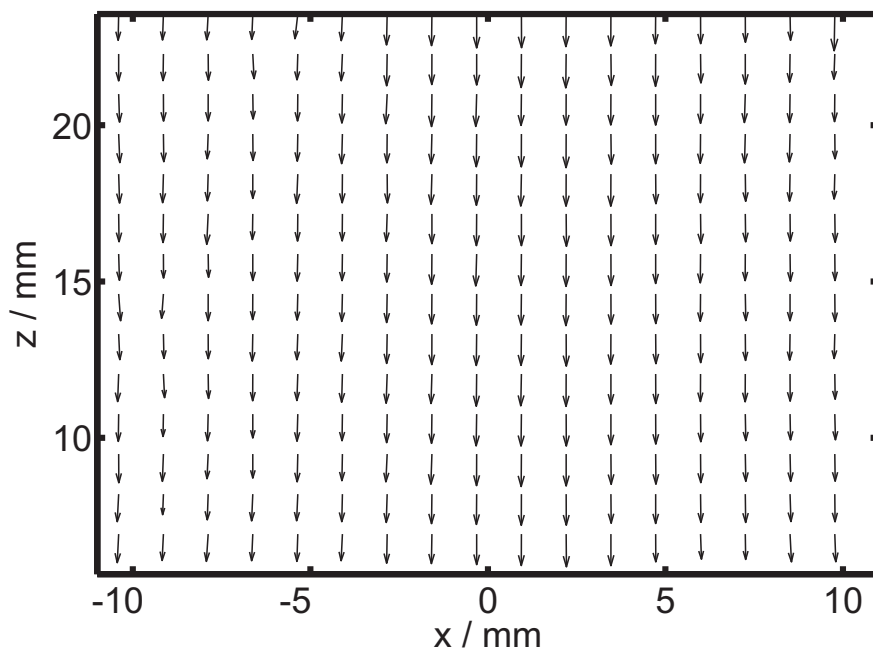


Figure 5.7: Velocity field of the tracer particles without a temperature gradient inside the neutral gas.

Since the actual value of δ crucially depends on various experimental parameters it is necessary to determine its value experimentally in order to calibrate the PIV method. Therefore, the following procedure is performed after powering up the experiment and setting the neutral gas pressure.

At the desired gas pressure (typically $p = 50$ Pa), but without a plasma and without heating the electrode, tracer particles are injected by the electromagnetically driven dispenser. To ensure that no temperature gradient inside the neutral gas and thus no thermophoretic force is present the vacuum chamber has been kept at room temperature for at least one day before the measurement. Hence, the injected tracer particles are only subject to gravity and neutral friction force. The gravitational force acting on a tracer particle is according to Eq. (5.6) $F_{g,t} \approx 6.8 \times 10^{-12}$ N.

The analysis of the recorded PIV image pairs of the falling tracer particles shows, that the particles fall as expected in a straight line down to the electrode. In the corresponding velocity field (see Fig. 5.7) the vertical velocity component is almost constant in the complete field of view. This is expected since simple calculations show at the used neutral gas pressure the falling tracer particles reach their terminal velocity due to an equilibrium of gravitational and friction force, i.e. $F_{g,t} + F_{fr,t} = 0$, already after approximately the first 10 mm of their path. The mean vertical displacement of the particles within one PIV image pair is $\bar{\Delta z} = -11.5$ pixels with a standard deviation of $\sigma = 1.0$ pixels. This corresponds to a mean vertical velocity of $\bar{v}_z = -(0.176 \pm 0.001)$ m/s. Inserting Eq. (5.10) in Eq. (5.9) and rearranging yields δ . With the measured velocity value \bar{v}_z and

5.2. THE THERMOPHORETIC FORCE

equating $F_{th} = -F_{g,t}$ the Millikan coefficient is determined to be $\delta = 1.28 \pm 0.01$. This value is in good agreement with other experiments [120] and corresponds to a mostly diffusive reflection of the gas molecules after hitting a dust particle.

5.2.5 Balance of forces

Since the correct operation of the PIV-setup was demonstrated in the previous section the next step is to heat the electrode and to derive the thermophoretic force $\vec{F}_{th,t}$ acting on the tracer particles. This is done by measuring the velocity field of the tracer particles in the presence of a temperature gradient in the neutral gas and considering the following balance of force:

$$m_{d,t}\vec{a}_d = \vec{F}_{g,t} + \vec{F}_{th,t} + \vec{F}_{fr,t}. \quad (5.11)$$

Here \vec{a}_d is the acceleration of the tracer particles, which can be derived from the measured velocity field. In Eq. (5.11) all quantities except $\vec{F}_{th,t}$ are known, thus the thermophoretic force acting on the tracer particles can be derived.

Since the intention is to measure the thermophoretic force acting on the dust particles of a trapped Coulomb ball, at first such a spherical dust cloud is generated. The PIV camera is then adjusted to show the desired field of view. A picture of the trapped Coulomb ball is taken for a later reconstruction of the position of the confined cloud in the present thermophoretic force field. Then the rf and thus the plasma is switched off, which causes the Coulomb ball to fall down as shown in Fig. 5.2. With all other experimental parameters (especially the electrode temperature) kept constant, tracer particles are injected. In contrast to the measurement in the previous section the tracer particles are now not only subject to gravity and neutral friction, but also to thermophoresis.

The measured velocity field of the tracer particles is shown in Fig. 5.8. The field of view is identical to the previous measurement, i.e. it covers almost the complete width of the glass box and again the origin of the z -axis corresponds to the surface of the electrode. The topology of the field is significantly different from the case without a heated electrode shown in Fig. 5.7. In the upper part of the field of view the velocity is mostly directed downwards. Only a slight divergence of the vectors towards the glass walls is observable. This divergence, i.e. the radial velocity component, increases significantly when approaching the bottom of the field of view. Simultaneously, the vertical velocity component decreases, especially in the vicinity of the center axis ($x = 0$ mm). This deceleration of the particles is expected since the thermophoretic force is proportional to $-\vec{\nabla}T$ and is therefore directed upwards. This observation suggests that the thermophoretic force varies significantly with the vertical position but also with the distance from the center axis of the glass box.

To obtain the actual thermophoretic force field from the measured velocity data using Eq. (5.11), it is necessary to derive the acceleration of the tracer particles at each grid point of the velocity field. This is done by calculating the convective deviation

$$\vec{a}_d = (\vec{v}_d \cdot \vec{\nabla})\vec{v}_d. \quad (5.12)$$

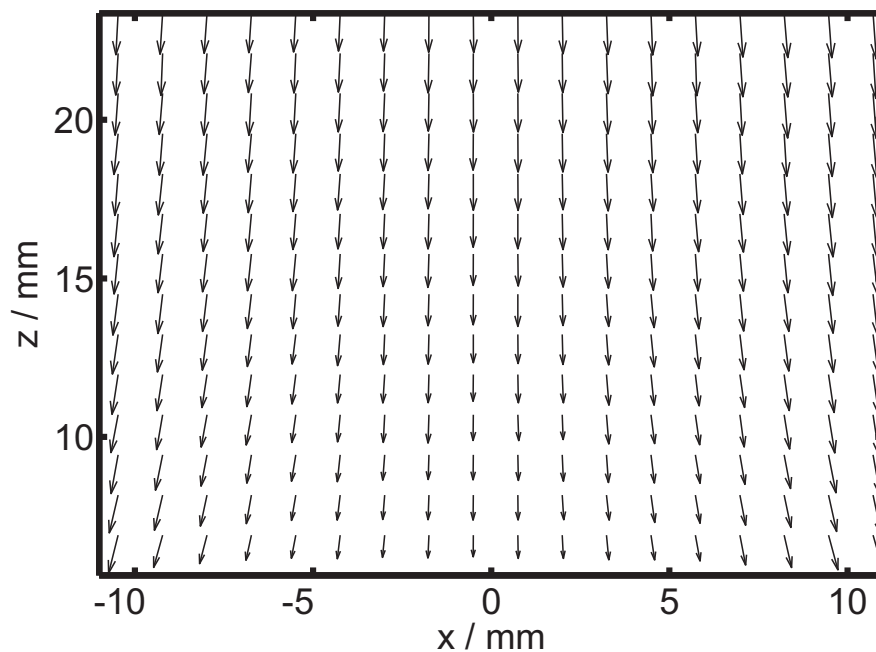


Figure 5.8: Velocity field of the tracer particles at the presence of a temperature gradient inside the neutral gas. The electrode is heated to a temperature of $T_E = 78$ °C. The temperature of the lid of the chamber is $T_v = 32$ °C.

It is well-known that numerical differentiation of data is very delicate because it dramatically amplifies the noise of the data. Hence, an approximation of the acceleration is used, which is derived by averaging the data resulting from Eq. (5.12). Despite a high noise level the analysis of the vertical component of the acceleration yields no significant systematic variation in the field of view. Thus, the vertical acceleration component is approximated by its mean value in the complete field of view $\bar{a}_z = 0.26$ m/s², i.e. the particles are assumed to be decelerated constantly in vertical direction. Since the divergence of the velocity field increases with the distance from the center axis the horizontal component has different directions in the left ($x < 0$ mm) and the right ($x > 0$ mm) half of the field. Hence, it is approximated by the average over all vertical positions (see Fig. 5.9). The radial component increases almost linearly from the center towards the glass walls. The slight deviations from a straight line in the vicinity of the walls may on the one hand attributed to interpolation errors of the PIV data in this region due to low dust densities. On the other hand, as discussed in Sec. 5.2, the outwards directed component of the thermophoretic force may be reduced in the immediate vicinity of the walls, which may explain the decreasing tendency at radial positions $x \lesssim -10$ mm and $x \gtrsim 10$. With this simple model the acceleration $\vec{a}(x, z)$ can be approximated at every position inside the glass box. In combination with the friction force $\vec{F}_{fr,t}$ and the gravitational force $\vec{F}_{g,t}$ the thermophoretic force $\vec{F}_{th,t}$ acting on the tracer particles is directly obtained by rearranging Eq. (5.11). Although the approximation of the acceleration data

5.2. THE THERMOPHORETIC FORCE

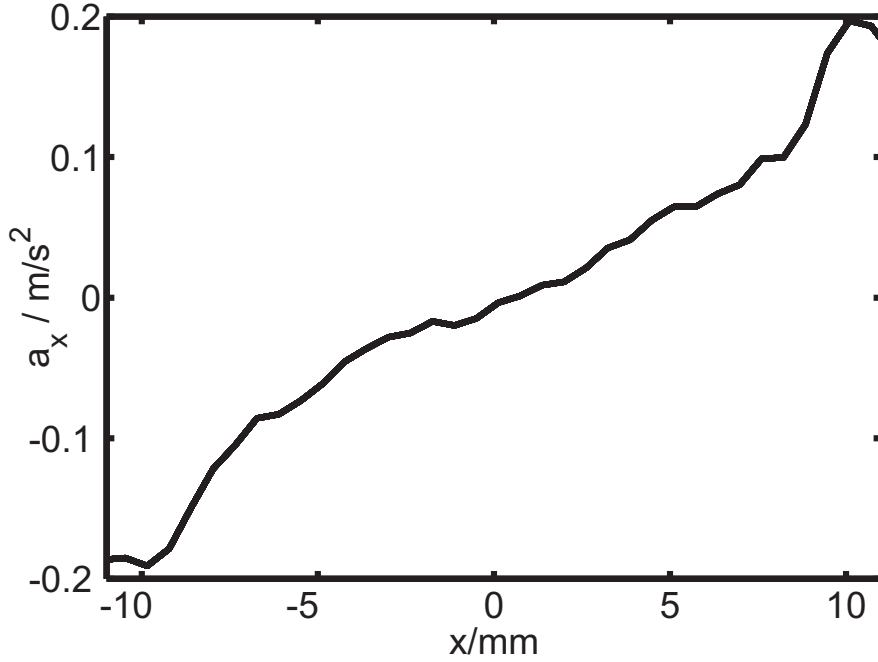


Figure 5.9: The mean horizontal acceleration component a_x is derived by numerical differentiation of the velocity field and averaging over all vertical positions z .

might appear crude, its actual influence on the derived thermophoretic force is small since inertial forces are small compared to the friction force.

5.2.6 The thermophoretic force field

The topology of the derived thermophoretic force field is plotted in Fig. 5.10. Since, according to Eq. (5.7) the thermophoretic forces $\vec{F}_{th,t}$ and $\vec{F}_{th,c}$ are simply scaled by the squared ratio of the corresponding particle diameters, the topology of the thermophoretic force field is identical for the tracer particles and the smaller particles of a Coulomb ball. In addition, as the thermophoretic force is proportional to $-\vec{\nabla}T$ rearranging Eq. (5.5) and inserting $\vec{F}_{th,t}$ yields the temperature gradient inside the glass box. Thus, by integrating the resulting temperature gradient field the temperature differences with respect to the position ($x = 0$ mm, $z = 5$ mm) are derived and plotted as contours in Fig. 5.10. It shows, that the temperature gradient systematically decreases from the bottom to the top of the field of view, which is consistent with the earlier suggested variation of the temperature gradient (see Sec. 5.1). In the lower part of the figure the vertical component of the temperature gradient is $\partial T/dz \approx 1700$ K/m, whereas the corresponding value at the top of the field of view is $\partial T/dz \approx 650$ K/m. Extrapolating the temperature gradient towards the lid of the chamber yields a good agreement with the actual temperature difference $\Delta T \approx 46$ K between the electrode and the lid of the chamber. The measured temperature gradient and respectively the

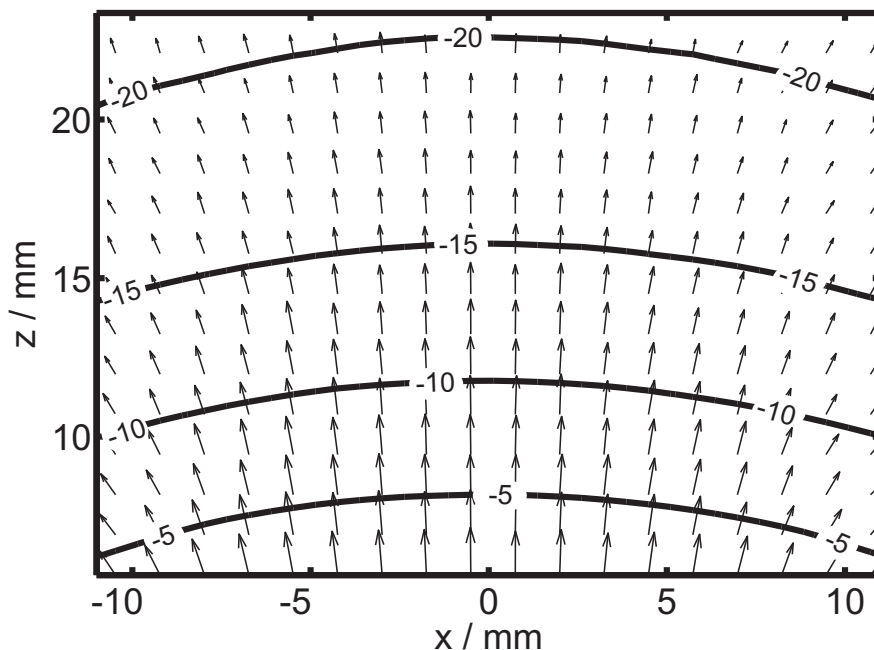


Figure 5.10: Thermophoretic force field. The contours show the temperature differences (in K) with respect to the position ($x = 0$ mm, $z = 5$ mm).

thermophoretic force is sufficiently strong to levitate a dust particle of a Coulomb ball, since the required gradient is $\partial T/dz \approx 1356$ K/m (see Sec. 5.2), which is in good agreement with Fig. 5.2.

Considering the topology of the measured thermophoretic force field, one observes a radially outward-directed component of the force, which increases when approaching the walls of the glass box. This observation implies that according to Eq. (5.5) the gas temperature decreases towards the walls of the glass box. Consequently, when examining the isotherms in Fig. 5.10, one observes at identical positions z a higher temperature in the center of the glass box than close to the walls. To get an explanation of this finding, which is on the first glance not intuitive, the one-dimensional heat transfer equation [121]

$$\frac{\partial T}{\partial t} = \Lambda_T \frac{\partial^2 T}{\partial z^2} \quad (5.13)$$

is considered. Here is $\Lambda_T = \Lambda/(\rho c)$ the thermal conductance and ρ the mass density of the observed material. The value $\tau = \Delta z^2/\Lambda_T$ defines the time scale for the relaxation of a temperature difference over a distance Δz . In the present case the values of τ for the glass of the walls and the argon inside the box have to be compared. With the data of Tab. 5.1 and a distance $\Delta z = 30$ mm one gets for the argon inside the glass box $\tau_{Ar} \approx 2 \times 10^{-2}$ s and for the walls of the box $\tau_{gl} \approx 1 \times 10^3$ s.

First, this result suggests that the gas inside the box reacts almost instantaneously on a change of the electrode temperature. This is in good agreement

5.2. THE THERMOPHORETIC FORCE

Table 5.1: Heat conductivity Λ , specific heat c and mass density ρ of glass and argon gas at $p = 50$ Pa and $T_n = 300$ K. For argon is $\rho = (pm_n)/(kT_n)$. The other values are taken from Ref. [122].

material	Λ $(\frac{W}{m K})$	c $(\frac{J}{kg K})$	ρ $(\frac{kg}{m^3})$
glass (silicon dioxide)	1.4×10^0	600	2.5×10^3
argon ($p = 50$ Pa, $T_n = 300$ K)	1.8×10^{-2}	521	8.0×10^{-4}

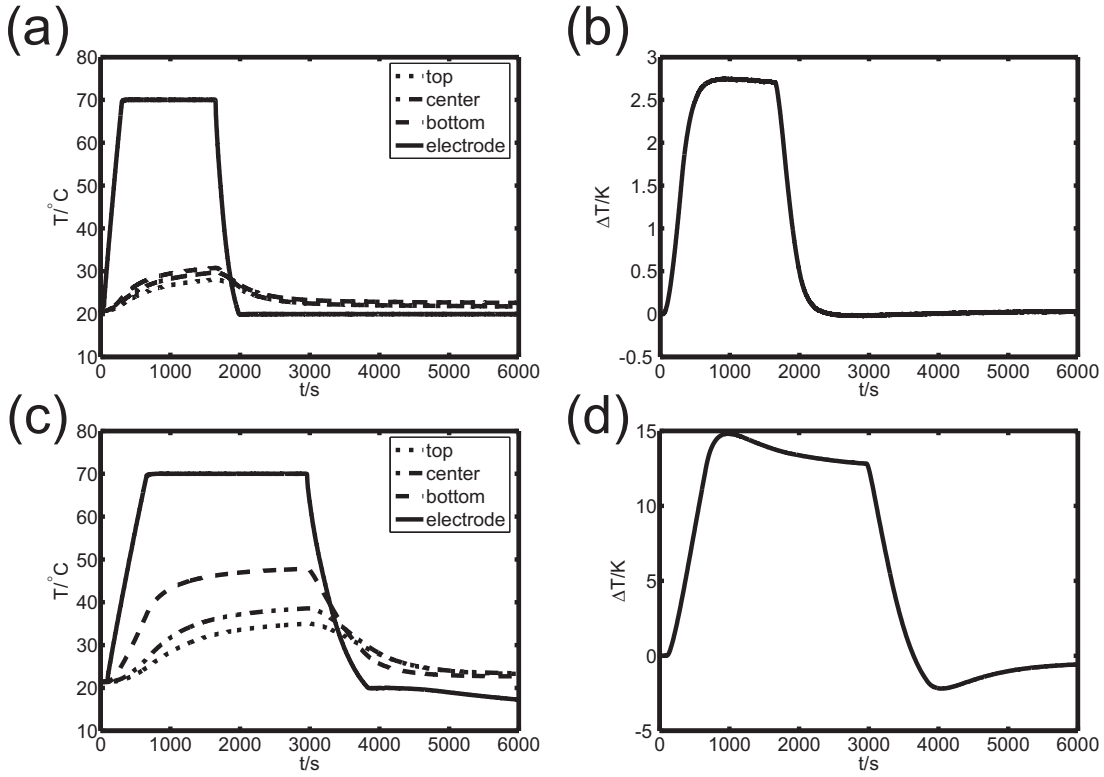


Figure 5.11: Temperature evolution at bottom, center and top of the glass box (left column) and temperature differences (right column) between top and bottom at $p \approx 10^{-2}$ Pa [(a), (b)] and $p = 100$ Pa [(c), (d)].

with the experiment, since as stated earlier (see Sec. 5.1), the shape of a confined Coulomb ball reacts very immediately on a variation of the electrode temperature. Second, it should takes many minutes to achieve a significant change of the temperature of the glass walls.

To verify this suggestions, temperature measurements were performed by gluing three small platinum resistors (PT100) with a small amount of epoxy glue

5. CONFINEMENT OF COULOMB BALLS

to the outside of a wall of a glass box ($30 \times 30 \times 30 \text{ mm}^3$). The resistors were positioned on the center line of the wall at different vertical positions ($z_1 \approx 2 \text{ mm}$, $z_2 \approx 15 \text{ mm}$, $z_3 \approx 28 \text{ mm}$). The temporal evolution of the measured temperatures during heating of the electrode from room temperature to $T_E = 70 \text{ }^\circ\text{C}$ and afterwards rapidly cooling down the electrode is measured at two different gas pressures.

Figure 5.11 (a) shows the evolution of the temperatures measured with the three thermal resistors and for comparison the temperature of the electrode. Here, the gas pressure is $p \approx 10^{-2} \text{ Pa}$, which is the base pressure of the chamber without any gas inlet. When the heating of the electrode starts ($t \approx 0 \text{ s}$) the temperature of the electrode increases rapidly until it reaches the nominal temperature of $T_E = 70 \text{ }^\circ\text{C}$ at $t \approx 300 \text{ s}$. At the same time the temperature measured at the bottom of the glass box increases by only $\approx 5 \text{ K}$. The other sensors at $z_2 \approx 15 \text{ mm}$ and $z_3 \approx 28 \text{ mm}$ show, as expected, an even smaller increase of the temperature. After approximately 2000 s the temperature at the bottom of the electrode has barely reached a value of $30 \text{ }^\circ\text{C}$ and is still rising slowly with a rate of approximately 3 K/h , which is qualitatively consistent with the calculated timescale $\tau_{gl} \approx 1.33 \times 10^3 \text{ s}$. In Fig. 5.11 (b) is the temperature difference between the sensor at the top and the bottom of the glass box plotted. The maximum value of $\Delta T \approx 2.8 \text{ K}$ is reached at $t \approx 900 \text{ s}$ then the difference decreases slightly as a consequence of the heating of the glass wall. The temperature difference between the bottom sensor and the electrode is during the whole measurement remarkable large and indicates a very low heat transfer between the electrode and the glass box. According to the measurement it should take hours until the temperature of the glass walls reaches the temperature of the electrode.

In the case of a gas pressure of $p = 100 \text{ Pa}$ (argon) the temporal evolution of the temperatures shows qualitatively the same effects as at the lower pressure, however the absolute values are significantly different [see Fig. 5.11 (c)]. Here, the temperature on the glass wall rises much faster compared to the previous case. As the electrode reaches its nominal temperature of $T_E = 70 \text{ }^\circ\text{C}$ the sensor at the bottom of the glass box measures $\approx 40 \text{ }^\circ\text{C}$. However, at the same time, the temperature at the top is $\approx 26 \text{ }^\circ\text{C}$, which is only slightly more than at the lower pressure at the corresponding time. This results in a temperature difference [see Fig. 5.11 (d)] between top and bottom of the glass box, which is significantly larger than at $p = 10^{-2} \text{ Pa}$. Again, the maximum value of the temperature difference (here $\Delta T \approx 15 \text{ K}$) is reached slightly after the nominal temperature of the electrode is reached.

The significantly larger temperature of the glass box at the high gas pressure shows that its temperature is mainly affected by heating from the gas and not by heat conduction along the walls. Considering the maximum value of the temperature difference between the sensor at the top and bottom of the glass box it corresponds to a mean temperature gradient inside the wall of $\partial T / \partial z \approx 580 \text{ K/m}$. This value is approximately half the mean vertical temperature gradient in the field of view of Fig. 5.10. Keeping in mind, that the presented Coulomb balls are typically confined at a gas pressure of $p = 50 \text{ Pa}$ the discrepancy is expected to be

5.2. THE THERMOPHORETIC FORCE

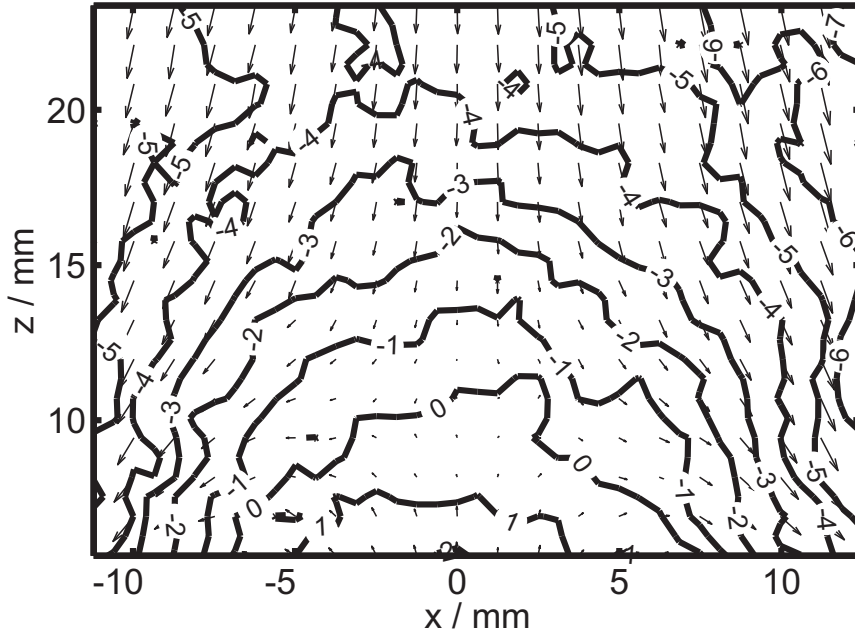


Figure 5.12: The sum of thermophoretic and gravitational force $F_{th} + F_g$. The contours indicate the magnitude of the vertical component in units of 10^{-13} N.

even larger. This may be attributed to a non-linear spatial temperature evolution in the direct vicinity of the glass wall and to a lower accuracy of the PIV data close to the walls of the glass box due to interpolation errors. Nevertheless, these findings show, that the heating of the glass box takes a very long time and the glass walls stay significantly colder than the gas inside the box for hours. Hence, the measured temperature profile as well as the topology of the thermophoretic force field are reliable.

To get an impression of how the thermophoretic force affects the particles of a Coulomb ball, the sum $\vec{F}_{th,c} + \vec{F}_{g,c}$ is plotted in Fig. 5.12. The contours mark the values of the vertical component of the resulting force in units of 10^{-13} N. The contour labeled "0" connects all points where the thermophoretic force cancels gravity. Negative values indicate a downwards oriented force while positive values correspond to an upward directed force. The vertical location ($z \approx 11$ mm) of the force balance in the center of the glass box ($x = 0$ mm) agrees very good with the observations shown in Fig. 5.2. In addition the topology of the measured thermophoretic force field is consistent with the trajectories of the falling particles in the lower part of the glass box. Furthermore, an increase of T_E steepens the temperature gradient and thus enhances the thermophoretic force on a particle. As a consequence its levitation height increases, which is in agreement with the observation (see Fig. 5.1).

The topology and the magnitude of the measured thermophoretic force field is in good agreement with the observations, but it is alone not capable to provide a

horizontal confinement of the Coulomb ball. Furthermore, it is not strong enough to explain the levitation height of a Coulomb ball. The residual gravitational force acting on a dust particle can be read from Fig. 5.12. At a vertical position of $z = 19$ mm, where the Coulomb ball was levitated (compare with Fig. 5.1), the residual downwards directed force is $(3-4) \times 10^{-13}$ N. This is $\approx 1/4$ of the gravitational force $\vec{F}_{g,c}$ and has to be compensated by additional plasma induced forces as suggested in Sec. 5.1.

5.2.7 Accuracy of the measurement

At the end of this section a few comments on the accuracy of the presented measurements have to be made. An important point in performing the PIV measurements is the number density of the injected particles. On the one hand a certain minimum number of particles is necessary in each PIV image to allow for an accurate analysis.

It was mentioned that a superposition of multiple PIV images is used to adjust the dust density after the actual measurement to yield the necessary data quality. This method combines the contradictory requirements of a high number density of the dust, which is required by the block-matching algorithm, and a diluted dust flux for minimizing gas drag. However, the cone-shaped dust shower as a consequence of the small dispenser leads to a spatial inhomogeneity of the dust density, which cannot be eliminated by the discussed method. This leads to a reduced accuracy of the derived velocity data in the upper outer regions of the glass box ($z \gtrsim 15$ mm, $|x| \gtrsim 5$ mm). Fortunately, this region is of little interest for the present analysis.

The absolute values, although not the topology, of the measured force fields depend crucially on the accuracy of the neutral friction force, i.e. especially the value of the Millikan coefficient δ in Eq. (5.9). Therefore, its measurement has to be carried out carefully. In addition, Eq. (5.9) depends on the gas density n_n . Due to the temperature gradient in the neutral gas and at pressure equilibrium its density is reduced in the lower part of the glass box with respect to the upper region. However, according to the ideal gas law $p = n_n k_B T_n$ and a temperature difference of ≈ 20 K in the field of view, this variation is below 10 % and can be neglected.

The accuracy of the analytic expression for the thermophoretic force [see Eq. (5.5)], due to the uncertainty of the value β , does not affect the resulting thermophoretic force field, since Eq. (5.5) is only used to derive the temperature difference field (contours in Fig. 5.10). In addition, the consistency of the absolute value of the derived force field can easily be verified by measuring the vertical location of the force balance $\vec{F}_{th,t} + \vec{F}_{g,t} = 0$ after switching the rf off, as described above. To summarize, the good agreement between the observation and the derived thermophoretic field shows that the mentioned sources of errors have a small influence on the accuracy of the derived thermophoretic force field and the uncertainty of the vertical equilibrium position in Fig. 5.10 is estimated as $\Delta z < 2$ mm.

5.3 Plasma-induced forces

As found in the last sections the thermophoretic force provides an essential contribution to the vertical confinement of Coulomb balls. Nevertheless, this force alone is not capable to establish a stable confinement. The behavior of the dust particles after switching the plasma off requires a significant contribution of plasma-induced forces, like the electric field force and the ion-drag force. The knowledge of the corresponding force fields completes the understanding of the trap. To determine these forces the plasma properties need to be known. In principle this information can be derived from measurements. Unfortunately, such measurements require some kind of diagnostic like a Langmuir probe, which is invasive and which severely disturbs the plasma. Other non-invasive methods, like LIF-spectroscopy, drop out because of the expected low ion densities in the present experiment, which results in too weak signals. To get a quantitative impression of the contribution of the mentioned forces, a hydrodynamic simulation of the complete discharge including the glass box was performed.

5.3.1 Simulation of the discharge

For the simulation of the plasma properties inside the discharge the commercially available fluid code SIGLO-2D [123] by Boeuf *et al.* [124, 125] was used. The code performs a two-dimensional simulation of low power rf and dc discharges in axial symmetry and considers electrons and up to two ion species. The transport of the electrons is described by the first three moments of the Boltzmann equation whereas, for the ions, only the first two moments are taken. The code contains two different sets of gas parameter for argon, which describe the required gas properties like electron and ion mobility, ionization frequencies, recombination rate etc.. For the simulations performed here, the more recent parameter set based on [126] was used. The simulation was carried out on a rectangular grid with a maximum possible number of 50×50 cells. To fit to the real-world dimensions of the experiment both dimensions of the grid can be scaled independently. Each cell of the grid can be assigned either to be an electrode, a metallic or dielectric wall, gas volume or a surface that emits secondary electrons. Neighboring electrode cells or respectively metallic cells are considered to be electrically connected, thus they form macroscopic electrodes and metallic walls. Each macroscopic electrode can either be directly or capacitively coupled to an individual voltage source. In the latter case a dc bias can be applied in addition to an rf voltage. When no bias is applied, the electrode attains a self-bias as a consequence of unequal rates of electrons and ions hitting the surface.

A screenshot of SIGLO-2D shows the grid of cells and illustrates the simulated discharge geometry (see Fig. 5.13). Since the code assumes a cylindrical symmetry the figure shows an ρ - z section of the discharge. The horizontal axis is the axis of symmetry the vertical axis points in radial direction. With respect to the real experiment the geometry is rotated by 90° , as the symmetry axis in real world points upwards. The dark grey cells at the left boundary of the grid

5. CONFINEMENT OF COULOMB BALLS

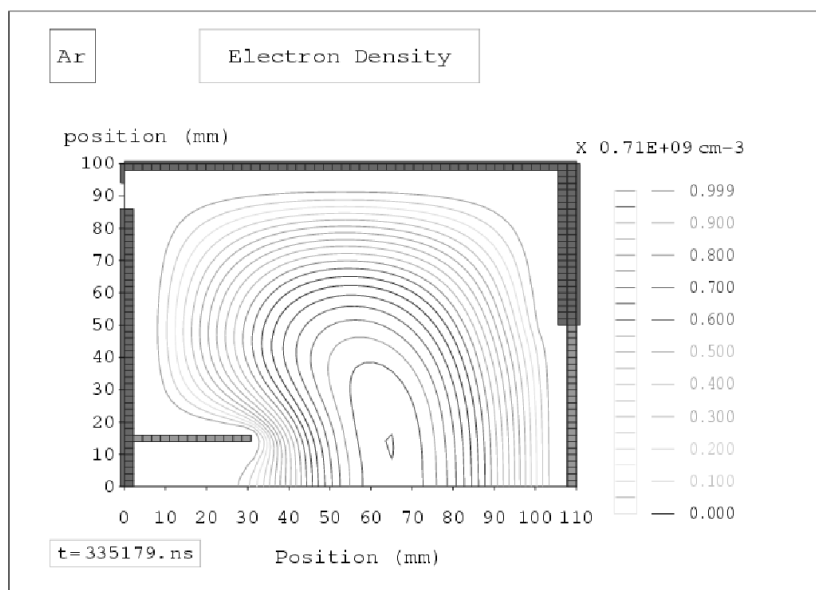


Figure 5.13: Screenshot of the SIGLO-2D simulation software.

correspond to the powered electrode. These cells are capacitively coupled to the simulated rf generator in analogy to the experiment. No external bias was applied. The 8.5 cm radius of the electrode is identical to the experiment. The upper boundary of the grid are grounded metallic cells corresponding to the side walls of the discharge chambers. The four dielectric windows in these walls are neglected in the simulation. On the one hand, it is not straightforward to translate them into the cylindrical symmetry and, on the other hand, they are not expected to show a significant influence on the plasma inside the glass box. The right boundary of the grid corresponds to the lid of the chamber with the large window or respectively the dielectric plate when using the electromagnetically driven dispenser. In agreement with the experiment the distance between the electrode end the lid of the chamber is approximately 10 cm. Since it is intended to get an impression of the plasma inside the glass box the box is represented in the simulation by a thin dielectric wall with a length of approx. 30 mm at a radial position of 15 mm directly on top of the powered electrode.

The selected geometry and parameters of the simulation ensures a good approximation of the real world experiment. Nevertheless there are a few points to mention. First, as a consequence of the cylindrical symmetry of the simulation, the dielectric wall corresponds to a glass tube with a circular cross-section. On the one hand, with respect to the experiment, this results in a smaller simulated plasma volume inside the glass box and thus probably a lower plasma density. On the other hand, the ratio of surface and volume, i.e. the influence of losses to the dielectric walls, is in the square box larger than in the simulated cylindrical case.

5.3. PLASMA-INDUCED FORCES

This should result in a reduced plasma density inside the square box with respect to a cylindrical tube containing the same volume. Both effects are considered to cancel each other, hence the simulated glass tube is a good approximation of the experiment.

Second, the simulation does not consider an effect of the dust on the plasma parameters. Since the particles are a sink for electrons and ions their presence affects the plasma in their vicinity. However, for the moment the influence of the dust is considered to be negligible because the number of particles inside the glass box is small. Nevertheless, this point will be discussed in more detail later. Finally, even though the plasma inside the glass box is the actual matter of interest, it is necessary to simulate the complete discharge. As the maximum number of 50×50 grid cells is limited by the software, the resolution of the simulation inside the glass box is limited to approx. 13 by 7 cells. This is not much and should be kept in mind when evaluating the results of the simulation. To agree with the experimental conditions of the above observations the simulation has been carried out at a gas pressure of 50 Pa (argon) and a rf amplitude of $U_{rf} \approx 21$ V. The countours in Fig. 5.13 correspond to the averaged electron density inside the discharge chamber after a simulated time of approx. 335 μ s, which corresponds to approx. 4500 rf cycles. This ensures that the simulation reaches steady state.

To get a better impression of the complete discharge the simulated data is mirrored and rotated as shown in Fig. 5.14. The electron density and thus due to the quasineutrality of the plasma also the ion density, has its maximum value of $n_{e,max} \approx 7 \times 10^{14} \text{ m}^{-3}$ near the geometric center of the discharge chamber. This value is typical for such a kind of discharge and can be verified by e.g. Langmuir probe measurements in the bulk plasma [52, 78]. Additionally, the simulations show that there is no plasma production inside the glass box, but only a diffusive plasma. A more detailed view of the region inside the glass box in Fig. 5.15 reveals a very low electron density. At the position where Coulomb balls are observed ($x = 0$ mm, $z = 19$ mm) the simulated density is $n_e \approx 10^{12} \text{ m}^{-3}$. The electron temperature (see Fig. 5.16) varies inside the glass box from $T_e \approx 1$ eV in the vicinity of the electrode up to $T_e \approx 3$ eV at the top of the glass box, which is also the temperature in most parts of the bulk plasma. In contrast to the electrons the ions are at room temperature ($T_i \approx 0.026$ eV), as expected for this kind of discharge [52]. From the simulated data the linearized Debye length

$$\lambda_D = \left[\frac{1}{\lambda_{De}^2} + \frac{1}{\lambda_{Di}^2} \frac{1}{1 + v_i^2/\bar{v}_{ti}^2} \right]^{-1/2} \quad (5.14)$$

as a function of the ion velocity v_i is calculated [127]. Here, the term $1/(1 + v_i^2/\bar{v}_{ti}^2)$ accounts for the effect of accelerated ions streaming to the electrode and the walls of the glass box. The result is plotted in Fig. 5.17.

At the levitation point ($x = 0$ mm, $z = 19$ mm) the Debye length becomes $\lambda_D \approx 0.7$ mm yielding with $a_{ws} = 0.3$ mm (see Sec. 5.1) a screening strength $\kappa \approx 0.43$. This value is in excellent agreement with the simulations in Sec. 4.5.

5. CONFINEMENT OF COULOMB BALLS

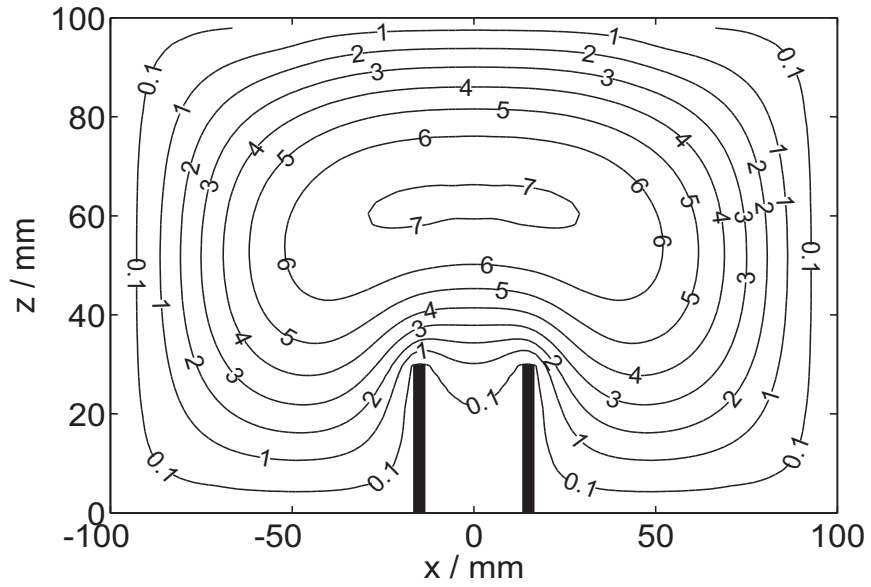


Figure 5.14: Simulated electron density n_e in the complete discharge in units of 10^{14} m^{-3} .

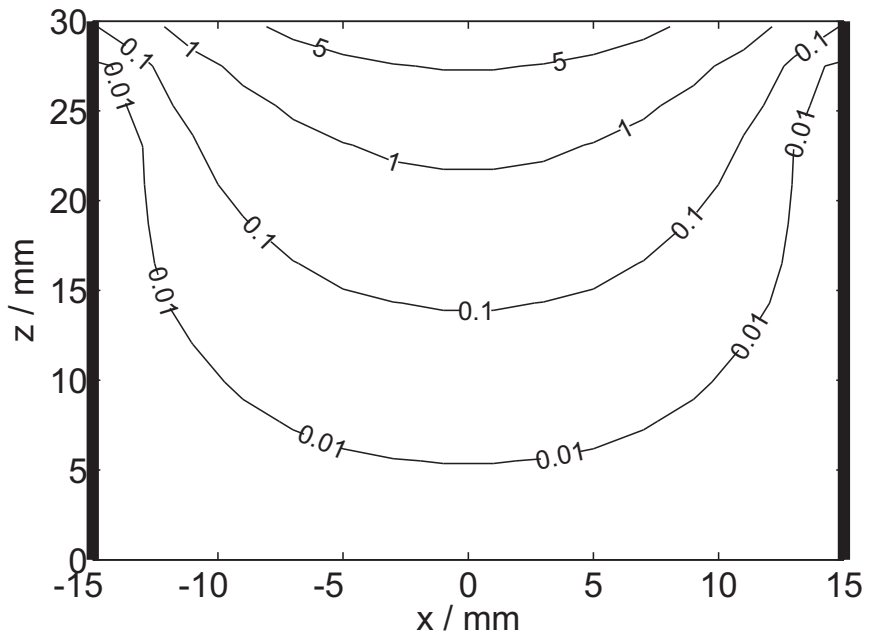


Figure 5.15: Detailed view of the electron density $n_e/10^{13} \text{ m}^{-3}$ inside the glass box.

5.3. PLASMA-INDUCED FORCES

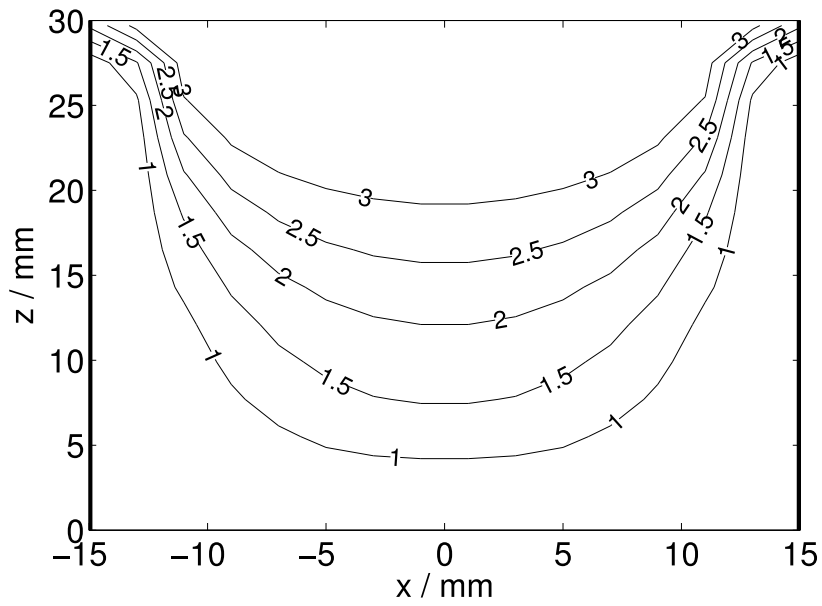


Figure 5.16: Electron temperature T_e / eV inside the glass box.

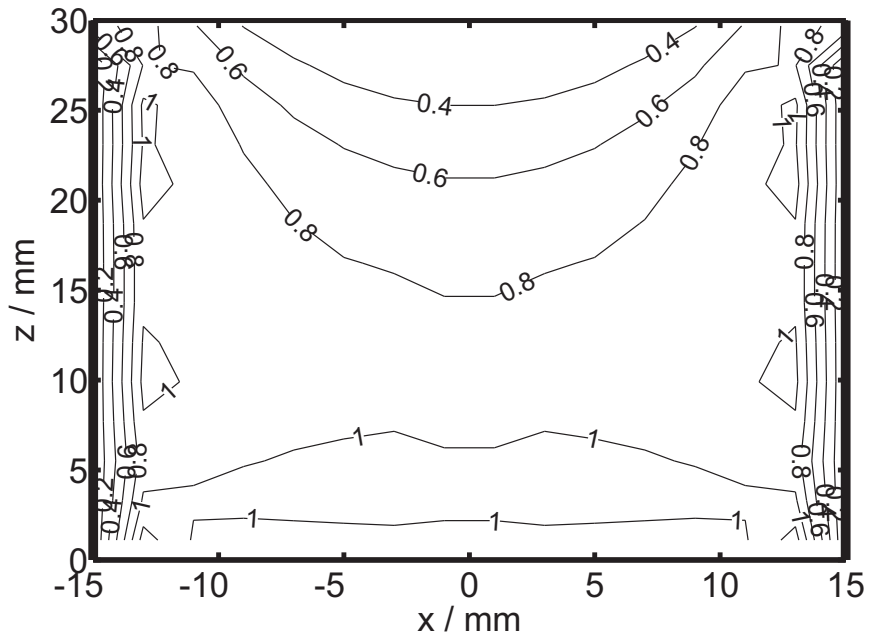


Figure 5.17: Linearized Debye length λ_D / mm inside the glass box.

In order to determine the influence of the plasma on the trapped dust particles it is necessary to derive the plasma induced forces from the simulated data.

5.3.2 Electric field force

The electric field force acting on a dust particle inside a plasma is given by $\vec{F}_E = q_d \vec{E}$, i.e. it depends on the electric field \vec{E} and the dust charge q_d . The electric field \vec{E} is derived from the gradient of the electric potential, which results from the simulation.

To calculate the electric field force it is necessary to know the charge of the dust particles. Measurements of the dust charge are in some cases possible by e.g. resonance methods [30, 128], the analysis of wave phenomena [129–131] or the observation of particle collisions [132]. Unfortunately, none of these methods is applicable in the present case. First, the resonance method is limited to complex plasmas in the sheath where the confining potential well is known. Second, the observation of waves suffers in the present experiment from strong damping due to the high gas pressure. Finally, the estimation of the dust charge by observing particle collisions is limited to systems with very few particles, ideally two.

However, there are theoretical models that allow for estimating the charge of a dust particle from the plasma properties, like the densities and temperatures of the electrons and ions, respectively. A common approach is to consider the particle as a floating probe and use the *Orbital Motion Limit* (OML) model by Mott-Smith and Langmuir [133]. This simple model is limited to a single dust particle surrounded by an infinitely extended collision-less plasma, which is not fulfilled in the present case. Recent experiments [131] and calculations [84] reported a significant influence of the dust charge on the *collisionality parameter* λ_D/ℓ_i , where ℓ_i is the mean free path of ion-neutral collisions. In the collision-less limit $\lambda_D/\ell_i \rightarrow 0$ the charge equals the value obtained by the OML model but is significantly reduced when $\lambda_D/\ell_i > 0$. Assuming an ideal gas at $p = 50$ Pa and room temperature $T_n = 300$ K then the density of the neutral gas is given by $n_n = p/(k_B T_n)$. Thus, by using $\ell_i = 1/(n_n \sigma_{ni})$, with the cross-section of ion-neutral collisions $\sigma_{ni} \approx 125 \text{ \AA}^2$ [107, 134], yields $\lambda_D/\ell_i \approx 11$. Hence, the collisions have a significant influence on the charge, i.e. the OML model is not valid in the present case. According to Ref. [84] the charge is given by

$$q_d = -\frac{4\pi\epsilon_0 a k_B T_e}{e} z \quad (5.15)$$

with the radius of the dust particle $a = d/2$ and the dimension less particle charge

$$z \approx \frac{3T_i}{T_e} \sqrt{\frac{v_{Te}}{v_{Ti}}} \sqrt{\frac{\ell_i}{\lambda_D}} \quad (5.16)$$

Here is $T_{e,i}$ the temperature, $v_{Te,i} = (k_B T_{e,i}/m_{e,i})$ the thermal velocity and $m_{e,i}$ the mass of the electrons and respectively the ions. For the used dust this model yields a charge of $q_d \approx -1000e$, compared to the charge estimated by the (not applicable) OML model $q_{d,OML} \approx -8600e$. Using the above derived value of the shielding strength, the observed crystalline order of the Coulomb balls suggests values for the coupling parameter $\Gamma > 270$. This requires in the present case a minimum dust charge of $q_{d,min} \approx -1200e$. Since the two models discussed above

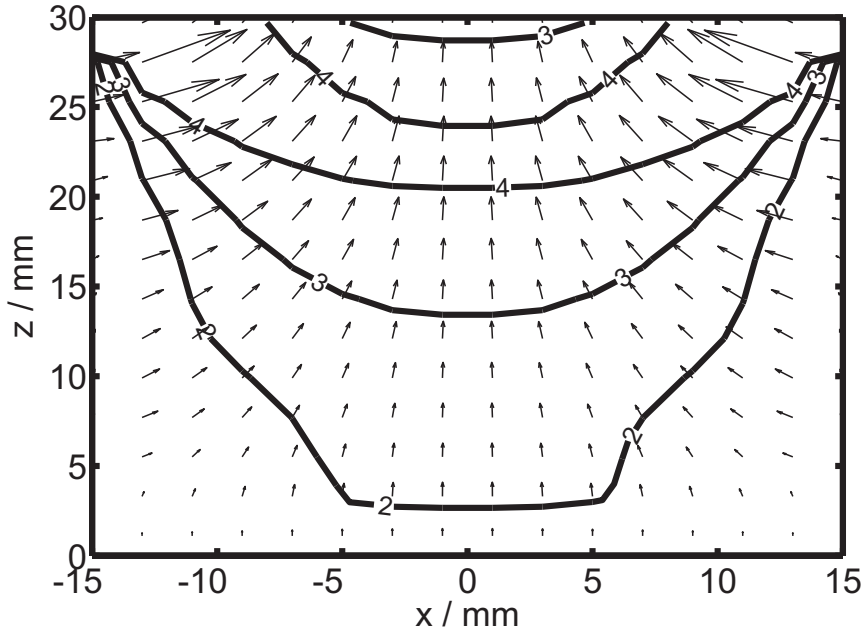


Figure 5.18: Electric field force \vec{F}_E acting on a dust particle with a charge $q_d = 2000e$. The contours indicate the vertical component $F_{E,z} = 10^{-13}$ N

can be considered a maximum and a minimum for the real dust charge a value of $q_d = -2000e$ is considered realistic in the present experiment and is assumed for the following calculations.

The resulting electric force field is plotted in Fig. 5.18. In the center of the glass box \vec{F}_E points upwards and increases from the electrode to the top of the box. The contours show the vertical component $F_{E,z}$. At $z = 19$ mm, where the Coulomb ball is observed, its value is $F_{E,z} \approx 3 \times 10^{-13}$ N. This is in good agreement with the estimated residual gravitational force (see Sec. 5.2.6). Near the glass walls \vec{F}_E points almost horizontally into the center of the box. Thus, the topology of the force field is suitable to provide a horizontal confinement of a Coulomb ball.

5.3.3 Ion-drag force

Similar to the neutral drag force, which is caused by collisions between neutral gas molecules and a dust particle, the ion-drag force is a consequence of collisions between ions and a dust particle. In contrast to the neutral drag force, where the collision cross-section is only given by the gas-kinetic cross-section of the colliding particles the interaction between the charged ions and dust particles, is much more complicated. First, the collision cross-section is larger than the gas-kinetic cross-section, since a negatively charged dust particle attracts the positively charged ions. Second, even though an ion does not hit the dust particle directly but passes in its vicinity it transfers momentum to the particle due to Coulomb interaction.

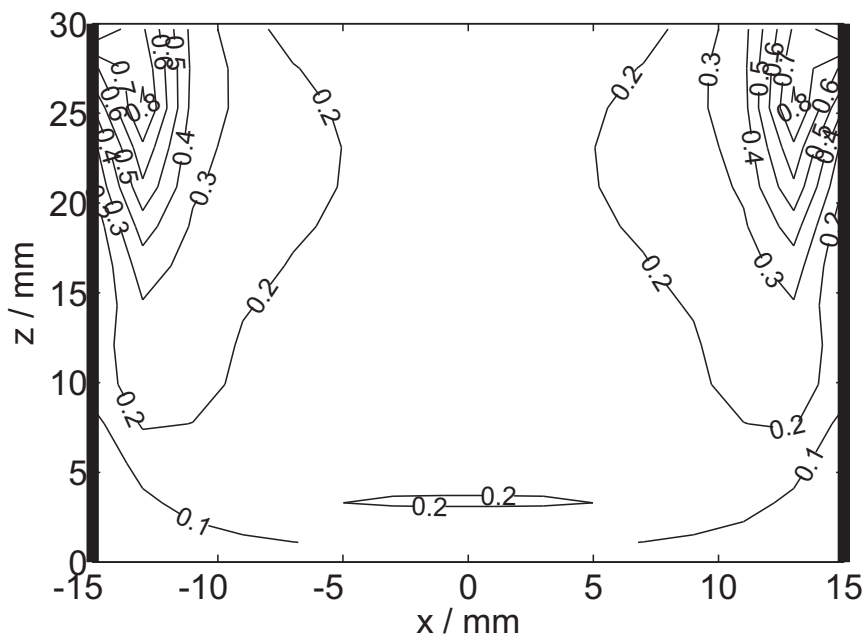


Figure 5.19: Ion velocity inside the glass box in units of the Bohm velocity (Mach number).

According to the two mechanisms of momentum transfer to a dust particle the ion-drag force consists of two components. These components are the *collection force* $F_{i,coll}$, which is a consequence of direct collisions between ions and the particle and the *orbit force* $F_{i,orb}$, which corresponds to the momentum transfer due to Coulomb scattering.

The ion drift velocity in units of the Mach number $M = v_i/v_B$ (with the Bohm velocity $v_B = (k_B T_e/m_i)^{1/2}$) is derived from the simulation and plotted in Fig. 5.19. In most parts of the glass box the ions have very low velocities with a Mach number $M \approx 0.2$. The present case of subsonic ions allows for neglecting the collection force since the cross-section for direct collisions between ions and a dust particle is very small [135]. Thus the ion-drag force is dominated by the orbit force. The question of how to treat the orbit force in an analytic way was an intensely debated topic in the past [135–141]. Recently Khrapak *et al.* [84] presented a sophisticated general analytic expression for the ion-drag force, which includes all relevant effects except for collisions with neutrals and is considered to be valid for most plasma conditions. However, a simpler expression given by Khrapak *et al.* [142] is still valid in the present case of very slow subsonic ions. A modification of this model was presented by Gozadinos *et al.* [143], which considers a more realistic shifted Maxwellian velocity distribution

$$f(\vec{v})d\vec{v} = \left(\frac{m_i}{2\pi k_B T_i}\right)^{3/2} \exp\left(-\frac{m_i(\vec{v} - \vec{v}_i)^2}{2k_B T_i}\right) d\vec{v}, \quad (5.17)$$

of the ions and allows for a convenient computational handling of the ion-drag

5.3. PLASMA-INDUCED FORCES

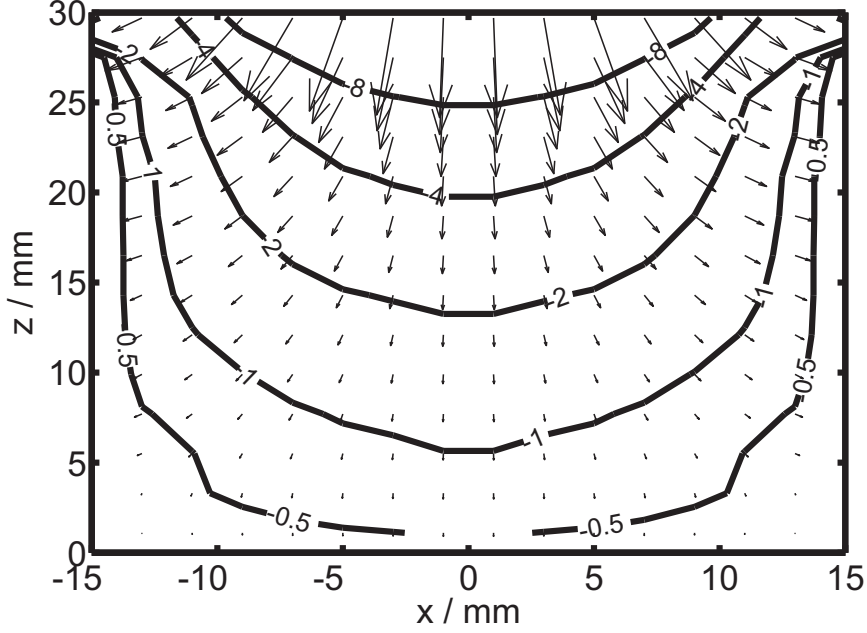


Figure 5.20: Ion-drag force \vec{F}_i inside the glass box. The contours indicate the vertical component $F_{i,z}/10^{-15}$ N.

force. With a given ion velocity distribution $f_i(v)$ according to [142, 143] the ion-drag force is given by

$$F_i = \sqrt{\frac{2}{\pi}} \frac{n_i m_i}{v_{T,i} v_i} \int_0^\infty \sigma_o(v) v^3 \exp\left(-\frac{v^2 + v_i^2}{2v_{T,i}^2}\right) \left[\cosh\left(\frac{vv_i}{v_{T,i}^2}\right) - \frac{v_{T,i}^2}{vv_i} \sinh\left(\frac{vv_i}{v_{T,i}^2}\right) \right] dv. \quad (5.18)$$

Here is $v_{T,i} = (k_B T_i / m_i)^{1/2}$ the ion thermal velocity and $\sigma_o = 4\pi b_{\pi/2}^2 \Gamma_K$ the orbit cross-section with the Coulomb logarithm

$$\Gamma_K = \ln\left(\frac{\lambda_D + b_{\pi/2}}{r_d + b_{\pi/2}}\right) \quad (5.19)$$

and the collision parameter

$$b_{\pi/2} = -\frac{q_d e}{4\pi\epsilon_0 m_i v_i^2}, \quad (5.20)$$

which results in a deflection by 90° of a passing ion. Since, according to this model collisions with impact parameters larger than the Debye length yield a significant contribution to the ion-drag force the resulting values can be considered an upper boundary in the present case of a dust cloud. Here, a cut-off at half the inter-particle distance b is suggested, which yields a reduction of the force.

The ion-drag force \vec{F}_i , which is derived from the simulation using Eq. (5.18) is plotted in Fig. 5.20. In comparison with \vec{F}_E the topology of the field is inverted.

The contours show the vertical component $F_{ion,z}$. In the whole region of the trap, the ion-drag force is by two orders of magnitude smaller than the electric field force. Thus, the ion-drag force does not contribute to the topology of the trap.

These two findings, the low ion velocity and the weak ion-drag force are an important requirement for the observed structural properties of the Coulomb balls. First, the low Mach numbers ensure that the Coulomb balls are not subject to non-isotropic order phenomena like the formation of particle chains that result from a directed ion flow [28]. Second, the lack of plasma production inside the glass box and thus a weak ion-drag force explains why Coulomb balls are not affected by the "Void"-phenomenon [66–70].

In summary, the results of the simulation are in good agreement with the experimental observations and emphasize their reliability.

5.4 Properties of the trap

The superposition of the gravitational force \vec{F}_g , the measured thermophoretic force $\vec{F}_{th,c}$, the simulated electric field force \vec{F}_E , and ion-drag force \vec{F}_i is plotted in Fig. 5.21. The contours indicate the potential energy E_{pot} of a sample particle ($q_d = 2000e$) inside the force field. A distinct minimum in E_{pot} is located at ($x = 0$ mm, $z \approx 19$ mm), which agrees with the position of a trapped Coulomb ball (see Fig. 5.2).

A horizontal section through the minimum of the potential energy at a vertical position $z = 19$ mm is plotted in Fig. 5.21. The data values (crosses) agree very good with the parabolic fit (solid curve). The solid vertical lines indicate the radius $r_{CB} \approx 1.6$ mm of the observed Coulomb ball taken from Fig. 5.2. To verify whether the derived potential well is capable to trap the Coulomb ball and yield a similar radius of the cluster, molecular dynamics simulations using the previously described code by Piel [96] (see Sec. 4.5) are performed. These calculations use a dust charge $q_d = -2000e$, a particle number $N = 200$ and consistent with Fig. 5.22, an isotropic parabolic potential well

$$\Phi(r) = \frac{E_{pot}(r)}{q_d} \approx 40600V \left(\frac{r}{\text{m}} \right)^2. \quad (5.21)$$

Pure Coulomb interaction between the dust particles results in a radius $r_{Coul} = 2.1$ mm, which is indicated by the dotted vertical lines in Fig. 5.22. In addition, considering Yukawa interaction at a Debye length of $\lambda_D = 0.8$ mm, as obtained from the SIGLO-2D simulations (see Fig. 5.17) at the location of the trapped Coulomb ball, the radius of the simulated cluster is $r_{Yuk} = 1.7$ mm (dashed vertical lines). As expected, the simulation with Coulomb interaction yields a slightly larger dust cloud than observed in the experiment, where Yukawa interaction is present. The excellent agreement between the radius of the simulated Yukawa cluster with the experiment emphasizes the reliability of the measured potential well of the trap[see Eq. (5.21)].

These simulations assume an isotropic spherical potential well, which is justified for small Coulomb balls. However, Fig. 5.21 shows, that in case of a large

5.4. PROPERTIES OF THE TRAP

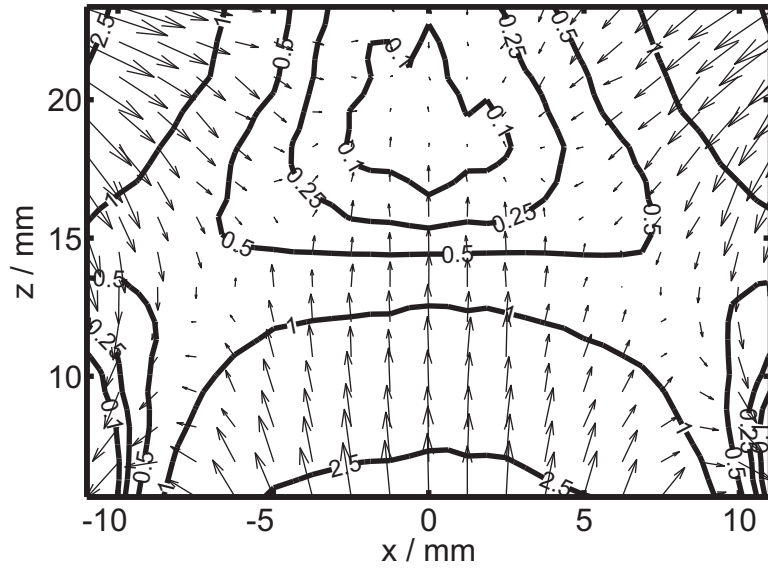


Figure 5.21: Superposition of all forces: $\vec{F}_g + \vec{F}_E + \vec{F}_i + \vec{F}_{th}$. The contours indicate the potential energy of a sample particle ($q_d = 2000e$) in units of 10^{-15} J.

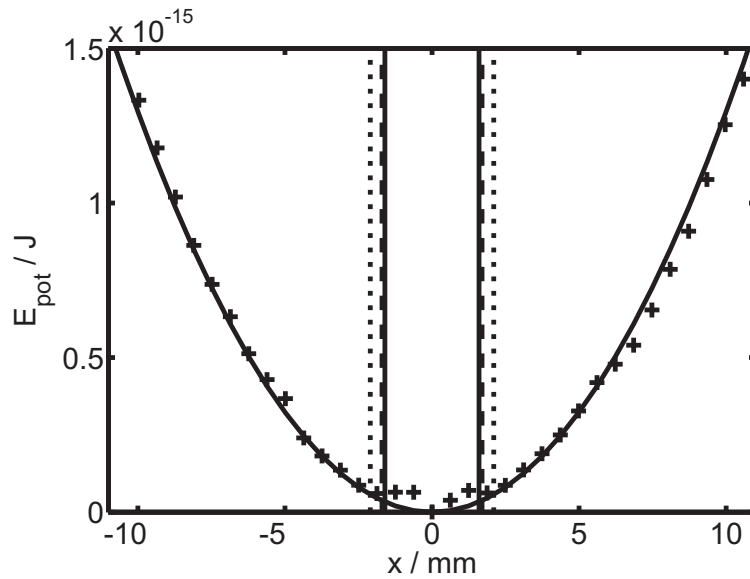


Figure 5.22: The horizontal section through the minimum of the trap potential well ($z \approx 19$) mm yields a parabolic potential well (crosses: data values, solid curve: parabolic fit). The solid vertical lines indicate the observed cluster radius. MD simulations of a cluster ($N = 200$, $q_d = -2000e$) yield the dotted (Coulomb interaction) and the dashed (Yukawa interaction, $\lambda_D = 0.8$ mm) lines.

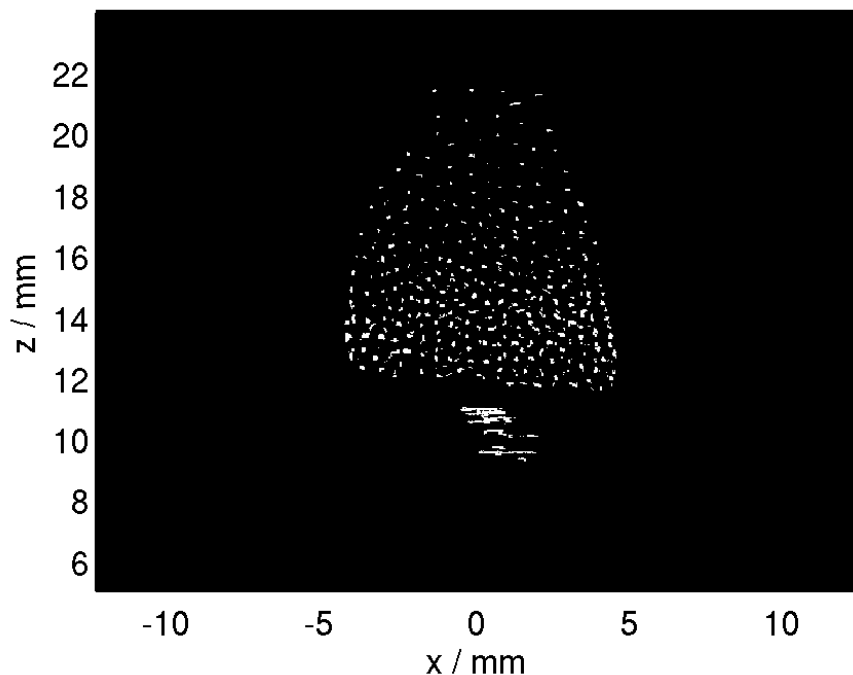


Figure 5.23: Vertical section through a large dust cloud. The triangular shape of the cloud is consistent with the derived trap potential. The horizontal traces below the cloud are caused by the motion of a single particle trapped below the cloud.

Coulomb ball the topology of the trap suggests a deformed triangular shaped vertical section of such a dust cloud . This suggested property of the trap is experimentally verified. A vertical section through a large dust cloud trapped inside the glass box is shown in Fig. 5.23. Its triangular shape is in good agreement with the topology of the trap potential (see Fig. 5.21). The horizontal traces below the cloud are caused by the motion of a single particle trapped below. In addition, the reduced steepness of the potential well above the minimum is consistent with observations, as Coulomb balls tend to show a reduced particle density and defects at the top (see Sec. 4.2).

5.5 Higher-order effects

The presented model of the trap includes the gravitational force, the thermophoretic force, the electric field force and the ion-drag force. Their combination yields a confinement of a Coulomb ball inside the glass box, which is in very good agreement with the observations. With respect to their contribution the confinement, these forces can be hierarchically ordered. The strongest zero-order forces are gravity and thermophoresis. The interaction of both forces yield

5.5. HIGHER-ORDER EFFECTS

a situation in which the dust is mainly affected by the electric field force and a small residual fraction of gravity, which can be considered first-order forces. As presented, the zero- and first-order forces suffice to quantitatively explain the size and location of Coulomb balls. In addition to these forces there are other higher-order forces, which act on the particles of a Coulomb ball. One of these forces is the ion-darg force, which was already discussed in Sec. 5.3.3 and is included in the model of the trap. Although they are not required for the confinement, these forces cause under certain conditions effects that are not explainable with the presented model.

An example is the occurrence of self-confinement effects as a consequence of the influence of the dust on the surrounding plasma. According to the quasi-neutrality of the complex plasma, i.e.

$$n_i e - n_e e - n_d Z_d \approx 0, \quad (5.22)$$

where $Z_d = q_d/e$, the presence of charged dust particles requires a reduction of the electron density and respectively an increase of the ion density in the vicinity of the dust cloud to keep the complex plasma neutral. This results in a more negative plasma potential in this region and a smaller charge of the particles due to electron depletion. The magnitude of this effect is typically characterized by the so-called *Havnes parameter* $P = Z_d n_d / n_e$ [144]. Considering, consistent with the experiment, a Coulomb ball with $N = 200$ particles, a dust charge $Z_d = 2000$ and a radius $r = 1.6$ mm, the average charge density in the volume of the Coulomb ball is

$$n_d Z_d \approx \frac{3Nq_d}{4\pi r^3} \approx 2 \times 10^{13} \text{ m}^{-3}, \quad (5.23)$$

yielding a Havnes parameter $P \approx 20$. Since, the dust charge $Z_d = 2000$ is required by the observed crystalline order (see Chapt. 4) and is consistent as well with the observed levitation height as with the cluster radius (see Sec. 5.4) the high value of P does not shed doubt on the value of the dust charge. Rather, it suggests a significant modification of the plasma potential in the vicinity of the cloud [145]. According to Annaratone *et al.* [146] this potential difference between a complex plasma and a dust-free plasma involves the formation of an electrostatic double layer at the boundary between both plasmas. An indication for the presence of such a double layer around a confined Coulomb ball yields the observation shown in Fig. 5.24. Under certain conditions it is possible to confine two Coulomb balls inside the glass box at the same time. The dust clouds are aligned vertically and are touching each other in the center region of the glass box, only separated by a narrow dust-free gap. Here, the upper dust cloud was injected after the lower cloud had been confined. In the proposed model of the trap, one expects that both dust clouds merge to one large, depending on the electrode temperature, possibly vertically elongated cloud. Surprisingly, even after a rough treatment by varying the rf power and the electrode temperature both clouds did not merge. This finding is in good agreement with observations under microgravity conditions [146, 147], where two complex plasmas are separated by a similar dust-free gap,

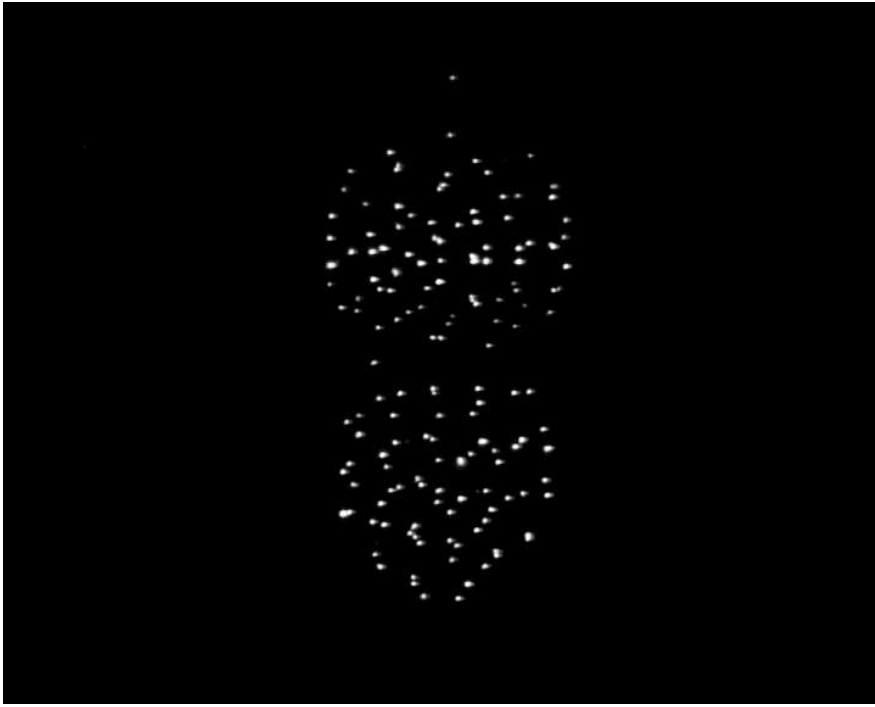


Figure 5.24: Two almost spherical clusters are confined inside the trap. Both clouds are separated by a small dust-free gap.

which is attributed to the presence of electrostatic double layers surrounding the dust clouds. Although, the presence of a double layer seems to have an effect on the microscopic structure of the surface of a complex plasma [146] it is not relevant for the confinement of Coulomb balls, where much stronger forces are present. However, recent simulations [148] suggest that in the absence of strong electric and gravitational forces, a dust cloud might even be able to confine itself by its influence on the surrounding plasma.

6 Summary and outlook

In this thesis the basic properties of crystalline spherical complex plasmas and their confinement were explored. For this purpose, numerous experimental observations and simulations of the structural properties of the dust clouds as well as the plasma conditions inside the trap were performed.

A method was discussed to confine spherical complex plasmas under gravity conditions, which we named Coulomb balls. The used trap combines two principles that have been separately used before within the context of complex plasmas. First, dielectric walls in form of a small cubical glass box, are used to shape the plasma profile and to generate a lateral confinement of the Coulomb ball. Second, a thermophoretic force is applied to reduce the effect of gravity, which usually leads the dust to form flat dust clouds in the lower sheath of the discharge. With this new technique it is possible to confine a range from a single to many thousand particles, for a long period of time.

A scanning video microscopy diagnostic was implemented to derive the three-dimensional coordinates of each dust particle inside a Coulomb ball. The diagnostic acquires subsequent parallel sections of the observed dust cloud. In each section the two-dimensional particle coordinates are determined. By analyzing the intensity evolution of each particle in multiple sections their three-dimensional position was derived. The resulting real world particle coordinates have an accuracy of $\approx \pm 30 \mu\text{m}$. The uncertainty is more than one order of magnitude smaller than the typical inter-particle distance inside a Coulomb ball. By this method, precise three-dimensional reconstructions of observed dust clouds were obtained, which represented the basis for analyzing the structural properties of Coulomb balls.

Coulomb balls show a new kind of structural order in complex plasmas. The particles are arranged in nested shells. A Voronoi analysis performed on each shell shows that the particles form a hexagonal lattice within each shell. According to Euler's theorem, the hexagonal lattice is affected by defects with mainly pentagonal arrangements, which is a consequence of the curvature of the shell surface. The observed crystalline order is consistent with a statistical analysis of the dust cloud. First, the modulation of the pair distribution functions indicates global order and a finite inter-particle distance, as a consequence of

Coulomb repulsion. Second, the analysis of the thermal motion of the particles indicates a solid state, according to the Lindemann criterion.

The observed structural order of Coulomb balls is similar to the ordering found in laser-cooled ion clusters in Paul and Penning traps. However, a quantitative comparison with molecular dynamics simulations of Coulomb and Yukawa clusters reveals significant differences between Coulomb and Yukawa interaction. The weaker repulsion of the particles inside a (shielded) Coulomb ball results in a smaller inter-particle distance and consequently to smaller cluster radii, in comparison to a pure Coulomb system containing the same number of particles. Moreover, the shell occupation numbers, i.e. the number of particles located within a shell, show significant differences. In Coulomb balls, more particles are located at inner shells, whereas the outermost shell is depleted. In addition, boundaries for the shielding strength of the plasma were derived from the simulations, which are not directly measurable in the experiment.

The thermophoretic force field inside the trap was measured by analyzing the trajectories of tracer particles. For this purpose, a two-dimensional velocity field of heavier particles falling through the trap was derived by means of particle image velocimetry (PIV). When the plasma is switched off, these particles are only subject to gravity, gas friction and thermophoretic force. Since the first two forces are known, the thermophoretic force can be determined. The resulting force field shows that the thermophoretic force is a crucial component of the trap, as it compensates a significant fraction of the gravitational force on the dust particles. However, thermophoresis alone is not capable to generate a stable confinement. The convex topology of the plane of constant force gives no radial confinement and the absolute value of the force is only 70 % of the weight force of the particles. This result requires the presence of additional plasma-induced forces.

The plasma conditions inside the trap were derived from simulations with SIGLO-2D, a commercial code for rf plasma discharges. The small size of the plasma inside the trap does not allow for meaningful measurements of the plasma conditions with probes, as the presence of a probe unavoidably disturbs the plasma dramatically. Therefore, simulations of the complete discharge, including the trap, were performed. The simulation shows, that inside the trap no significant plasma production is present. Accordingly, a Coulomb ball resides in a very dilute diffusive plasma, which is dominated by losses to the walls of the glass box. In the vicinity of a Coulomb ball only very slow ions are present, which explains, why Coulomb balls are not affected by non-isotropic order, like the formation of particle chains.

The plasma-induced forces, i.e. the electric field force and the ion-drag force were derived from the simulated plasma conditions. The electric field force has an upwards directed component, whose magnitude is in excellent agreement

with the remaining 30 % of gravity which need to be compensated. In addition, the electric field force has a radially inwards directed component, that establishes the radial confinement of the dust particles. The topology of the ion-drag force is opposite to the electric field force. Since the ion-drag force is approximately two orders of magnitude weaker than the electric field force, it does not contribute to the confinement of Coulomb balls.

The sum of all forces yields a parabolic shape of the total potential well of the trap. The comparison of the position of the potential minimum and the observed position of the Coulomb ball shows an excellent agreement. Molecular dynamics simulations were performed, which include the real world properties of the observed dust cloud, like the dust charge and the particle number, as well as the derived potential well of the trap. A pure Coulomb cluster and a Yukawa cluster at a shielding length of the plasma as obtained from the SIGLO-2D code was simulated. The radii of both simulated clusters show, within the uncertainties, a close agreement with the experiment. These results reveal, that the model of the trap, which includes gravity, the thermophoretic force and ion-drag force is capable to explain the confinement of Coulomb balls quantitatively.

The confinement of Coulomb balls does not require self-confinement mechanisms. In the proposed model of the trap an influence of dust on the plasma conditions is not included. The good agreement between the derived trap potential and the experimental observation shows that the effect of the dust is a correction of higher order, comparable to the strength of the ion-drag force. Estimations suggest an effect of the plasma potential inside the confined dust cloud, which induces the formation of an electrostatic double layer surrounding a Coulomb ball [146]. Indications of the presence of such a double layer are found in the experiment. This effect is assumed to become important when no strong confining forces are present, but is negligible in the present situation.

Trapped Coulomb balls have numerous advantages compared to other finite three-dimensional strongly-coupled systems. In contrast to similar experiments in complex plasmas [31, 75], where almost spherical clouds are dominated by particle chains, here the thermophoretic force reduces the required electric field to confine the particles. This, together with the small ion density in the vicinity of a Coulomb ball, leads to an effective reduction of the ion-drag force and associated alignment effects. Unlike ion-clusters in Paul and Penning traps, where the trap requires oscillating motions of the ions, the particles in the presented trap are only subject to their thermal random motion. Further, the macroscopic size and the large mass of the individual dust particles of a Coulomb ball slows down their motion. In complex plasmas the time scales of dynamical processes are of the order of many milliseconds, whereas nanoseconds in ion clusters. This simplifies the observation of Coulomb balls and suggests analyzing dynamical phenomena. In addition, a variation of the neutral gas pressure inside

the discharge allows to adjust the damping of the particle motion, which is not possible in other systems. The large charge of the particles results in large inter-particle distances, thus a high transparency of the system, which allows to observe each single particle, even in the bulk of very large dust clouds. Finally, the presented trap is sufficiently robust with respect to an external manipulation of the Coulomb ball by means of e.g. laser manipulation or a modulation of the electrode bias.

The discovery of Coulomb balls opens a wide range of interesting future experiments. The observation and analysis of dynamical phenomena, like waves and normal modes, is an obvious topic. Besides the general interest, especially an independent method to determine the particle charge inside a Coulomb ball might be obtained. These experiments are strongly related to the manipulation of a Coulomb ball by means of laser beams or by a modulation of the electrode bias, which can be used to excite waves, heat the Coulomb ball to enforce melting, or to explore the force balance of single particles on the surface of a Coulomb ball. A quantitative measure for the influence of self-confinement effects on Coulomb balls might be derived. With respect to large Coulomb balls, the transition from shell structure to bulk order is an important question. Simulations of spherical ion clusters show the formation of a bcc lattice in the center of systems containing more than 10^4 particles [48]. A fundamental question is, how this transition point depends on shielding. Experimental studies of Coulomb balls may give new answers. To answer these fundamental questions concerning the thermodynamic properties and dynamical phenomena of these finite strongly-coupled systems, numerous future experimental and theoretical investigations are required. Since many of these questions cannot be answered by experiments in ion clusters, because of the fast time scales involved, Coulomb balls are expected to have a growing share in these studies.

Bibliography

- [1] *Two-Dimensional Coulomb Liquids and Solids*, edited by Y. Monarkha and K. Kono (Springer, Berlin, 2004).
- [2] *Quantum Dots: a Doorway to Nanoscale Physics*, edited by D. Heiss (Springer, Berlin, 2005).
- [3] F. Diedrich *et al.*, Phys. Rev. Lett. **59**, 2931 (1987).
- [4] D. J. Wineland *et al.*, Phys. Rev. Lett. **59**, 2935 (1987).
- [5] S. L. Gilbert, J. J. Bollinger, and D. J. Wineland, Phys. Rev. Lett. **60**, 2022 (1988).
- [6] P. Bliokh, V. Sinitsin, and V. Yaroshenko, *Dusty and self-gravitational plasma in space* (Kluwer Academic Publ., Dordrecht, 1995).
- [7] L. Boufendi and A. Bouchoule, Plasma Sources Sci. Technol. **11**, A211 (2002).
- [8] P. Roca i Cabarrocas, N. Chaâbane, A. V. Kharchenko, and S. Tchakarov, Plasma Phys. Control. Fusion **46**, B235 (2004).
- [9] A. Bouchoule, *Dusty plasmas: physics, chemistry, and technological impacts in plasma processing* (John Wiley & Sons Ltd, New York, 1999).
- [10] J. H. Chu and L. I, Physica A **205**, 183 (1994).
- [11] H. Thomas *et al.*, Phys. Rev. Lett. **73**, 652 (1994).
- [12] Y. Hayashi and K. Tachibana, Jpn. J. Appl. Phys. **33**, L804 (1994).
- [13] J. E. Hug, F. van Swol, and C. F. Zukoski, Langmuir **11**, 111 (1995).
- [14] S. Naser, T. Palberg, C. Blechinger, and P. Leiderer, Prog. Colloid Polym. Sci. **104**, 194 (1997).
- [15] A. Melzer, A. Homann, and A. Piel, Phys. Rev. E **53**, 2757 (1996).
- [16] H. Thomas and G. E. Morfill, Nature **379**, 806 (1996).
- [17] L. I, W.-T. Juan, C.-H. Chiang, and J. H. Chu, Science **272**, 1626 (1996).

- [18] A. Piel and A. Melzer, *Plasma Phys. Control. Fusion* **44**, R1 (2002).
- [19] W.-T. Juan *et al.*, *Phys. Rev. E* **58**, R6947 (1998).
- [20] M. Klindworth, A. Melzer, A. Piel, and V. A. Schweigert, *Phys. Rev. B* **61**, 8404 (2000).
- [21] V. E. Fortov *et al.*, *JETP* **87**, 1087 (1998).
- [22] G. E. Morfill *et al.*, *Phys. Rev. Lett.* **83**, 1598 (1999).
- [23] H. Thomas *et al.*, *Physica Scripta* **89**, 16 (2001).
- [24] A. P. Nefedov *et al.*, *New J. Phys.* **5**, 33.1 (2003).
- [25] M. Klindworth, A. Piel, and A. Melzer, *Phys. Rev. Lett.* **93**, 195002 (2004).
- [26] M. Klindworth, O. Arp, and A. Piel, *J. Phys. D: Appl. Phys.* **39**, 1095 (2006).
- [27] H. Rothermel *et al.*, *Phys. Rev. Lett.* **89**, 175001 (2002).
- [28] V. A. Schweigert *et al.*, *Phys. Rev. E* **54**, 4155 (1996).
- [29] J. H. Chu and L. I, *Phys. Rev. Lett.* **72**, 4009 (1994).
- [30] T. Trottenberg, A. Melzer, and A. Piel, *Plasma Sources Sci. Technol.* **4**, 450 (1995).
- [31] V. E. Fortov, V. I. Molotkov, A. P. Nefedov, and O. F. Petrov, *Phys. Plasmas* **6**, 1759 (1999).
- [32] M. H. Thoma *et al.*, *Am. J. Phys.* **73**, 420 (2005).
- [33] J. J. Thomson, *Philos. Mag.* **39**, 236 (1904).
- [34] D. H. E. Dubin and T. M. O'Neill, *Rev. Mod. Phys.* **71**, 87 (1999).
- [35] E. Wigner, *Phys. Rev.* **46**, 1002 (1934).
- [36] S. Ichimaru, *Rev. Mod. Phys.* **54**, 1017 (1982).
- [37] N. McLachlan, *Theory and application of Mathieu functions* (Clarendon Pr., Oxford, 1947).
- [38] M. Drewsen *et al.*, *Phys. Rev. Lett.* **81**, 2878 (1998).
- [39] X.-P. Huang, J. J. Bollinger, T. B. Mitchell, and W. M. Itano, *Phys. Rev. Lett.* **80**, 73 (1998).
- [40] X.-P. Huang, J. J. Bollinger, T. B. Mitchell, and W. M. Itano, *Phys. Plasmas* **5**, 1656 (1998).

BIBLIOGRAPHY

- [41] T. B. Mitchell *et al.*, *Science* **282**, 1290 (1998).
- [42] A. Rahman and J. P. Schiffer, *Phys. Rev. Lett.* **57**, 1133 (1986).
- [43] R. W. Hasse and V. V. Avilov, *Phys. Rev. A* **44**, 4506 (1991).
- [44] K. Tsuruta and S. Ichimaru, *Phys. Rev. A* **48**, 1339 (1993).
- [45] T. Pohl, T. Pattard, and J. Rost, *Phys. Rev. Lett.* **92**, 155003 (2004).
- [46] W. M. Itano *et al.*, *Science* **279**, 686 (1998).
- [47] N. W. Ashcroft and N. D. Mermin, *Festkörperphysik* (Oldenbourg Verlag, München, 2005).
- [48] H. Totsuji, T. Kishimoto, C. Totsuji, and K. Tsuruta, *Phys. Rev. Lett.* **88**, 125002 (2002).
- [49] H. Ikezi, *Phys. Fluids* **29**, 1764 (1986).
- [50] M. O. Robbins, K. Kremer, and G. S. Grest, *J. Chem. Phys.* **88**, 3286 (1988).
- [51] S. Hamaguchi, R. Farouki, and D. H. E. Dubin, *Phys. Rev. E* **56**, 4671 (1997).
- [52] M. A. Liebermann and A. J. Lichtenberg, *Principles of plasma discharges and material processing* (John Wiley and Sons Inc., New York, 1994).
- [53] A. Melzer, Dissertation, Christian–Albrechts–Universität Kiel, 1997.
- [54] V. M. Bedanov and F. Peeters, *Phys. Rev. B* **49**, 2667 (1994).
- [55] Y.-J. Lai and L. I., *Phys. Rev. E* **60**, 4743 (1999).
- [56] V. A. Schweigert and F. Peeters, *Phys. Rev. B* **51**, 7700 (1995).
- [57] A. Melzer, M. Klindworth, and A. Piel, *Phys. Rev. Lett.* **87**, 115002 (2001).
- [58] A. Melzer, *Phys. Rev. E* **67**, 016411 (2003).
- [59] R. Ichiki *et al.*, *Phys. Rev. E* **70**, 066404 (2004).
- [60] Y. Ivanov and A. Melzer, *Phys. Plasmas* **12**, 072110 (2005).
- [61] Y. Hayashi, *Phys. Rev. Lett.* **83**, 4764 (1999).
- [62] M. Zuzic *et al.*, *Phys. Rev. Lett.* **85**, 4064 (2000).
- [63] J. L. Dorier, C. Hollenstein, and A. A. Howling, *J. Vac. Sci. Technol. A* **13**, 918 (1995).

- [64] G. Praburam and J. A. Goree, *Astrophys. J.* **441**, 830 (1995).
- [65] C. N. Davies, *Aerosol science* (Acad. Press, London, 1966).
- [66] J. Goree, G. E. Morfill, V. N. Tsytovich, and S. V. Vladimirov, *Phys. Rev. E* **59**, 7055 (1999).
- [67] V. N. Tsytovich, S. V. Vladimirov, G. E. Morfill, and J. Goree, *Phys. Rev. E* **63**, 056609 (2001).
- [68] M. R. Akdim and W. J. Goedheer, *Phys. Rev. E* **65**, 015401 (2002).
- [69] E. Thomas, B. M. Annaratone, G. E. Morfill, and H. Rothermel, *Phys. Rev. E* **66**, 016405 (2002).
- [70] V. N. Tsytovich, G. E. Morfill, U. Konopka, and H. Thomas, *New J. Phys.* **5**, 66 (2003).
- [71] M. Klindworth, private communication.
- [72] A. Barkan and R. L. Merlino, *Phys. Plasmas* **2**, 3261 (1995).
- [73] R. L. Merlino, in *New Vistas in Dusty Plasmas*, edited by L. Boufendi, A. Mikikian, and P. K. Shukla (AIP Conference Proceedings, Mellville, New York, 2005), pp. 3–11.
- [74] T. Trottenberg, D. Block, and A. Piel, *Phys. Plasmas* .
- [75] A. V. Zobnin *et al.*, *Plasma Physics Reports* **26**, 415 (2000).
- [76] O. Arp, D. Block, and A. Piel, *Phys. Rev. Lett.* **93**, 165004 (2004).
- [77] B. M. Annaratone *et al.*, *Plasma Phys. Control. Fusion* **46**, B495 (2004).
- [78] A. Homann, Dissertation, Christian–Albrechts–Universität Kiel, 1998.
- [79] MICROPARTICLES GMBH, Rudower Chaussee 5, 12484 Berlin.
- [80] Y. P. Raizer, *Gas Discharge Physics* (Springer, Berlin, 1997).
- [81] E. Guyon, J.-P. Hulin, and L. Petit, *Hydrodynamik* (Vieweg, Braunschweig, 1997).
- [82] V. E. Fortov *et al.*, *JETP* **96**, 704 (2003).
- [83] D. Block, private communication.
- [84] S. A. Khrapak, A. Ivlev, S. K. Zhdanov, and G. E. Morfill, *Phys. Plasmas* **12**, 042308 (2005).
- [85] M. P. Allen and D. J. Tildesley, *Computer simulation of liquids* (Oxford University Press, Oxford, 1987).

BIBLIOGRAPHY

- [86] F. Lindemann, Z. Phys. **11**, 609 (1910).
- [87] J. P. Schiffer, Phys. Rev. Lett. **88**, 205003 (2002).
- [88] W. C. Swope and H. C. Andersen, Phys. Rev. B **41**, 007042 (1990).
- [89] B. O'Malley and I. Snook, Phys. Rev. Lett. **90**, 085702 (2003).
- [90] D.-Q. Yu, M. Chen, , and X.-J. Han, Phys. Rev. E **72**, 051202 (2005).
- [91] K. Brown, Information Processing Letters **9**, 223 (1979).
- [92] J. Augenbaum and C. Peskin, J. Computational Physics **59**, 177 (1985).
- [93] F. Preparata and M. Shamos, *Computational Geometry: An Introduction* (Springer, Berlin, 1985).
- [94] M. Bonitz *et al.*, Phys. Rev. Lett. **96**, 075001 (2006).
- [95] H. Baumgartner, Monte-Carlo Simulation von Coulomb balls, 2006.
- [96] A. Piel, private communication.
- [97] L. Verlet, Phys. Rev. **159**, 98 (1967).
- [98] S. Nosé, J. Chem. Phys. **81**, 511 (1984).
- [99] W. G. Hoover, Phys. Rev. A **31**, 1695 (1985).
- [100] V. Golubnychiy, Dissertation, Christian–Albrechts–Universität Kiel, 1998.
- [101] L. Waldmann, Z. Naturforsch. **14A**, 589 (1959).
- [102] A. Santos, J. J. Brey, C. S. Kim, and J. W. Dufty, Phys. Rev. A **39**, 320 (1989).
- [103] G. M. Jellum, J. E. Daugherty, and D. B. Graves, J. Appl. Phys. **69**, 6923 (1991).
- [104] L. Talbot, R. K. C. anf R. W. Schefer, and D. R. Willis, J. Fluid Mech. **101**, 737 (1980).
- [105] F. Reif, *Fundamentals of Statistical and Thermal Physics* (McGraw-Hill, New York, 1965).
- [106] H. J. M. Hanley, J. Phys. Chem. Ref. Data **2**, 619 (1973).
- [107] R. N. Varney, PR **88**, 362 (1952).
- [108] O. Havnes *et al.*, Plasma Sources Sci. Technol. **3**, 448 (1994).
- [109] V. V. Balabanov *et al.*, JETP **92**, 86 (2001).

- [110] E. Thomas, J. D. Williams, and J. Silver, *Phys. Plasmas* **11**, L37 (2004).
- [111] U. Schnars and W. Jueptner, *Digital Holography* (Springer, Berlin, 2005).
- [112] M. Raffel, C. Willert, and J. Kompenhans, *Particle Image Velocimetry* (Springer, Berlin, 1998).
- [113] E. Thomas, *Phys. Plasmas* **6**, 2672 (1999).
- [114] A. Ashkin, *Phys. Rev. Lett.* **24**, 156 (1970).
- [115] A. M. Ignatov and S. G. Amiranashvili, *Phys. Rev. E* **63**, 017402/1 (2001).
- [116] PRECISION EFORMING LLC, 839 Route 13, Cortland, NY 13045.
- [117] MATLAB, The MathWorks, Inc., <http://www.mathworks.com/>.
- [118] J. K. Sveen, 27 pp (2004), <http://www.math.uio.no/~jks/matpiv>.
- [119] P. S. Epstein, *Phys. Rev.* **23**, 710 (1924).
- [120] B. Liu, J. Goree, V. Nosenko, and L. Boufendi, *Phys. Plasmas* **10**, 9 (2003).
- [121] W. Demtröder, *Experimentalphysik I, Mechanik und Wärme* (Springer, Berlin, 1994).
- [122] D. R. Lide, *CRC handbook of chemistry and physics* (CRC Press, Boca Raton, 1995).
- [123] SIGLO-2D, Version 1.1, Kinema Software.
- [124] J. P. Boeuf, P. Belenguer, and T. Hbid, *Plasma Sources Sci. Technol.* **3**, 407 (1994).
- [125] J. P. Boeuf and L. C. Pitchford, *Phys. Rev. E* **51**, 1376 (1995).
- [126] A. V. Phelps, C. H. Greene, and J. P. Burke, *J. Phys. B* **33**, 2965 (2000).
- [127] M. Klindworth, Dissertation, Christian-Albrechts-Universität Kiel, 2004.
- [128] A. Melzer, T. Trottenberg, and A. Piel, *Phys. Lett. A* **191**, 301 (1994).
- [129] A. Homann *et al.*, *Phys. Rev. E* **56**, 7138 (1997).
- [130] A. Homann *et al.*, *Phys. Lett. A* **242**, 173 (1998).
- [131] S. Ratynskaia *et al.*, *Phys. Rev. Lett.* **93**, 085001 (2004).
- [132] U. Konopka, L. Ratke, and H. M. Thomas, *Phys. Rev. Lett.* **79**, 1269 (1997).
- [133] H. M. Mott-Smith and I. Langmuir, *Phys. Rev.* **28**, 727 (1926).

BIBLIOGRAPHY

- [134] M. Hirt, Dissertation, Christian–Albrechts–Universität Kiel, 2003.
- [135] M. S. Barnes *et al.*, Phys. Rev. Lett. **68**, 313 (1992).
- [136] J. E. Daugherty, R. K. Porteous, M. D. Kilgore, and D. B. Graves, J. Appl. Phys. **72**, 3934 (1992).
- [137] M. D. Kilgore, J. E. Daugherty, R. K. Porteous, and D. B. Graves, J. Appl. Phys. **73**, 7195 (1993).
- [138] J. Perrin, P. Molinàs-Mata, and P. Belenguer, J. Phys. D: Appl. Phys. **27**, 2499 (1994).
- [139] T. Nitter, Plasma Sources Sci. Technol. **5**, 93 (1996).
- [140] S. A. Khrapak, A. V. Ivlev, G. E. Morfill, and H. M. Thomas, Phys. Rev. E **66**, 046414 (2002).
- [141] S. A. Khrapak and V. V. Yaroshenko, Phys. Plasmas **10**, 4616 (2003).
- [142] S. A. Khrapak and G. E. Morfill, Phys. Plasmas **9**, 619 (2002).
- [143] G. Gozadinos, A. V. Ivlev, and J. Boeuf, New J. Phys. **5**, 32 (2003).
- [144] O. Havnes, G. E. Morfill, and C. K. Goertz, J. Geophys. Res. **89**, 10,999 (1984).
- [145] J. Goree, Plasma Sources Sci. Technol. **3**, 400 (1994).
- [146] B. M. Annaratone *et al.*, Phys. Rev. E **66**, 056411 (2002).
- [147] G. Morfill *et al.*, Plasma Phys. Control. Fusion **44**, 263 (2002).
- [148] H. Totsuji, T. Ogawa, C. Totsuji, and K. Tsuruta, Phys. Rev. E **72**, 036406 (2005).

Publications

Parts of this thesis are already published or were presented at conferences:

Peer-reviewed journals:

1. O. Arp, D. Block, A. Piel, A. Melzer,
“Dust Coulomb Balls: Three-Dimensional Plasma Crystals”,
Phys. Rev. Lett. **93**, 165004 (2004)
2. O. Arp, D. Block, M. Klindworth, A. Piel,
“Confinement of Coulomb balls”,
Phys. Plasmas **12**, 122102 (2005)
3. ”Crystalline Order At 40,000 K”, AIP Physics News Update, **705**, October
20, 2004
4. M. Bonitz, D. Block, O. Arp, V. Golubnychiy, H. Baumgartner, P. Ludwig,
A. Piel, and A. Filinov,
“Structural Properties of Screened Coulomb Balls”,
Phys. Rev. Lett. **96**, 075001 (2006)

Invited talks:

1. D. Block, O. Arp, A. Piel and A. Melzer,
“Struktur sphärischer Staubwolken”,
DPG-Frühjahrstagung, Berlin, Fachvortrag, 2005
2. O. Arp, D. Block and A. Piel,
“Structure and trapping of three-dimensional dust clouds in a capacitively
coupled rf discharge”,
Fourth International Conference on the Physics of Dusty Plasmas, Orleans,
topical lecture, 2005

Contributions to international conferences:

1. O. Arp, D. Block, A. Piel and A. Melzer,
 “Three-dimensional dust clouds in a capacitively coupled rf discharge”,
31th EPS Conference on Controlled Fusion and Plasma Physics,
 London, 28 June to 2 July, 2004, ECA **28G**, O4-12
2. O. Arp, D. Block, M. Bonitz, H. Fehske, V. Golubnychiy, S. Kosse, P. Ludwig, A. Melzer and A. Piel,
 “3D Coulomb balls: Experiment and Simulation”,
J. Phys., Conf. Ser. 11, 234-247, 2005
3. O. Arp, D. Block and A. Piel,
 “Structure and trapping of three-dimensional dust clouds in a capacitively coupled rf-discharge”,
New Vistas in Dusty Plasmas: Fourth International Conference on the Physics of Dusty Plasmas,
 edited by L. Boufendi, M. Mikikian, P. K. Shukla, (American Institute of Physics, Mellville, NY, 2005), pp. 20-28
4. S. Käding, A. Melzer, O. Arp, D. Block, and A. Piel,
 “Stereoscopic Investigations of 3D Coulomb Balls”,
 in *New Vistas in Dusty Plasmas: Fourth International Conference on the Physics of Dusty Plasmas*,
 edited by L. Boufendi, M. Mikikian, P. K. Shukla, (American Institute of Physics, Mellville, NY, 2005), pp. 335-338
5. D. Block, O. Arp, A. Piel, and A. Melzer,
 “Coulomb balls in Experiment and Simulation”
 in *New Vistas in Dusty Plasmas: Fourth International Conference on the Physics of Dusty Plasmas*,
 edited by L. Boufendi, M. Mikikian, P. K. Shukla, (American Institute of Physics, Mellville, NY, 2005), pp. 454-457

Danksagung

An erster Stelle möchte ich mich bei Herrn Prof. Dr. Alexander Piel dafür bedanken, dass er mir die Anfertigung dieser Dissertation in seiner Arbeitsgruppe ermöglichte und jederzeit mit Rat und Tat zur Verfügung stand.

Des Weiteren danke ich insbesondere Dr. Dietmar Block für die intensive Zusammenarbeit im Rahmen dieser Arbeit und für seine Beiträge im Bereich Softwareentwicklung und Strukturanalyse.

Mein besonderer Dank gilt Dr. Markus Klindworth für die langjährige intensive Zusammenarbeit, den tiefgründigen Diskussionen in unzähligen Kaffeerunden und so manchem taktlosen Abend.

Ich danke Volker Rohwer und Michael Poser für die erstklassige Unterstützung bei allen technischen Problemen sowie Mattes Kroll, David Caliebe, Bartosz Slomski, Birger Buttenschön und Kristoffer Menzel für die tatkräftige Unterstützung im Rahmen ihrer Hiwi- und Praktikantentätigkeit.

Allen weiteren Mitgliedern der Arbeitsgruppe danke ich für das freundliche Arbeitsklima und die stete Hilfsbereitschaft.

Ich danke Herrn Krüger für den Bau zahlreicher Küvetten sowie Frau Thiedemann und Frau Seeger für die Unterstützung in bürokratischen Belangen.

Eidesstattliche Erklärung

Hiermit versichere ich an Eides Statt, dass die vorliegende Dissertation - abgesehen von der Beratung durch meinen wissenschaftlichen Lehrer und der Verwendung der angegebenen Hilfsmittel - nach Inhalt und Form meine eigene ist. Sie hat weder ganz noch teilweise an einer anderen Stelle im Rahmen eines Prüfungsverfahrens vorgelegen.

Kiel, den

Lebenslauf

Name: Oliver Arp
geboren: 07.04.1976 in Kiel
Familienstand: ledig
Staatsangehörigkeit: deutsch

Schulbildung: 1982 - 1986 Theodor-Möller-Grundschule in Kiel-Elmschenhagen
1986 - 1996 Gymnasium Elmschenhagen in Kiel
1996 Abitur mit den Prüfungsfächern:
Physik, Mathematik, Englisch und Geschichte

Wehrdienst: 1996/97 Versorger "Meersburg", 1. UG, Eckernförde

Studium: WS97/98 Immatrikulation im Fach Physik
an der Christian-Albrechts-Universität zu Kiel

WS99/00 Vordiplom mit Nebenfach Informatik
WS01/02 Diplom-Hauptprüfung mit Nebenfach Informatik

WS01/02-
WS02/03 Anfertigung der Diplomarbeit "Impedanzsonden-
messungen in komplexen Plasmen" in der Arbeits-
gruppe "Plasmadynamik" am Institut für Exper-
imentelle und Angewandte Physik der Christian-
Albrechts-Universität zu Kiel

WS02/03-
WS05/06 Promotion in der Arbeitsgruppe "Plasmadynamik"
am Institut für Experimentelle und Angewandte
Physik der Christian-Albrechts-Universität zu Kiel

